STRUCTURAL ANALYSIS OF VALLES MARINERIS, MARS

Luis Eduardo Vargas Medina, BSc.

MSc, Earth Sciences

Submitted in partial fulfillment
of the requirements for the degree of

Master of Science

Faculty of Earth Sciences, Brock University
St. Catharines, Ontario

Abstract

Valles Marineris is the largest canyonland formation known in the solar system being ~4000 km long and up to 11 km deep, it is subparallel to the Martian equator and exposes the interior of the Tharsis province. The spurs on the walls were analyzed using digital elevation models to geometrically quantify their morphology and orientation, relying on methodologies such as dip analysis, relief and curvature analysis, and attitude analysis among others. These analyses permitted the documentation of indicators of structural influence on the walls which were then classified by the morphology and the type of faults from which they originate.

Anomalous Planes (APs) are planar features that dip into the walls of a chasma and appear to be pre-existing fault planes within the Tharsis province. These faults are associated with the underlying structures of the Large Wrinkle Ridges (LWRs) located on Ophir Planum. An elastic dislocation model was used to corroborate that the APs can define the geometry of the underlying structure of the LWRs.

Planetary grabens can be distinguished from sapping channels using their geometries. It is proposed that the formation of Coprates Chasma was the result of four individual smaller chasmata that later joined. This work shows the tools and criteria used to demonstrate that the formation of Valles Marineris was complex as reflected in the formation of the wall morphology. It is shown that the formation of the walls was influenced by pre-existent structures and chasma producing faults.

Acknowledgements

I would first like to thank Frank Fueten for always steering me in the right direction whenever I had a question about my research. Thanks to Bob Stesky, his participation as a second reader was very valuable. Thank you to my other committee members and external examiner. I would also like to acknowledge Jon Walmsley for his participation making digital elevation models available for me.

Finally, I must express my very profound gratitude to my family and friends for their support and encouragement throughout the program.

Thank you.

Table of Contents

List of Figures

Chapter 1

Chapter 2

Chapter 3

Chapter 4

Appendices

List of Tables

Chapter 2

Chapter 3

List of Abbreviations

AP	Anomalous Plane
AVA	Augmented Visualization of Attitude
CTX	Context Imager
DEM	Digital Elevation Model
ETM	East Thaumasia Minor
HRSC	High Resolution Stereo Camera
LP	Lunae Planum
LTS	Length Throw and Slope
LWR	Large Wrinkle Ridge
MOLA	Mars Orbiter Laser Altimeter
MSSD	Mean Signed Squared Difference
OP	Ophir Planum
SG	Spur and Gully
SP	Solis Planum
TM	Thaumasia Minor

Chapter 1 : Introduction

1.1. Mars

Mars is one of the terrestrial planets in the solar system which has been a subject of study due the presence of many large-scale geological features such as Valles Marineris (Figure 1-1) [Lucchitta, 1978]. Mars is comparable to the Earth based on multiple similarities in its composition and geological development. Yet, differences are noticed when the size of the planets, and magnitude of geological features and events are compared. The radius of Mars is slightly more than half of the radius of the Earth, which is considerable since geological processes and features observed on Mars appear in a greater scale than those observed at Earth [Lucchitta, 1978; Schultz, 2002; Mege and Bourgeois, 2011]. Many differences are also associated with the difference in gravitational potential of each planet [Schultz, 2002] where the surface gravity of Mars gravity is 38% of Earth´s.

It is considered that Mars has no plate tectonics [Okubo and Schultz, 2003; Williams and Nimmo, 2004]; nevertheless, volcano-tectonic stress indicators (e.g. wrinkle ridges) appear on the Tharsis province [Mege and Masson, 1996]. Understanding the different geological processes involved is important to develop accurate theories about the geological history of Mars [Lucchitta, 1978; Peulvast and Masson, 1993; Andrews-Hanna, 2012]. The order of occurrence of the processes is necessary to date the visible features, but diverse erosional and fluvial processes have altered and covered the surface structures [Watters and Maxwell, 1986; Lucchitta, 1990]. Dating the Martian surface is accomplished using methods such as crater counting that estimate the relative surface ages from cratering density, with reference to sample-calibrated cratering ages taken from the moon [Hartmann and Neukum, 2001] and the use of the principle of superposition. Other data sources include meteorites, landers, and orbital spectrometers.

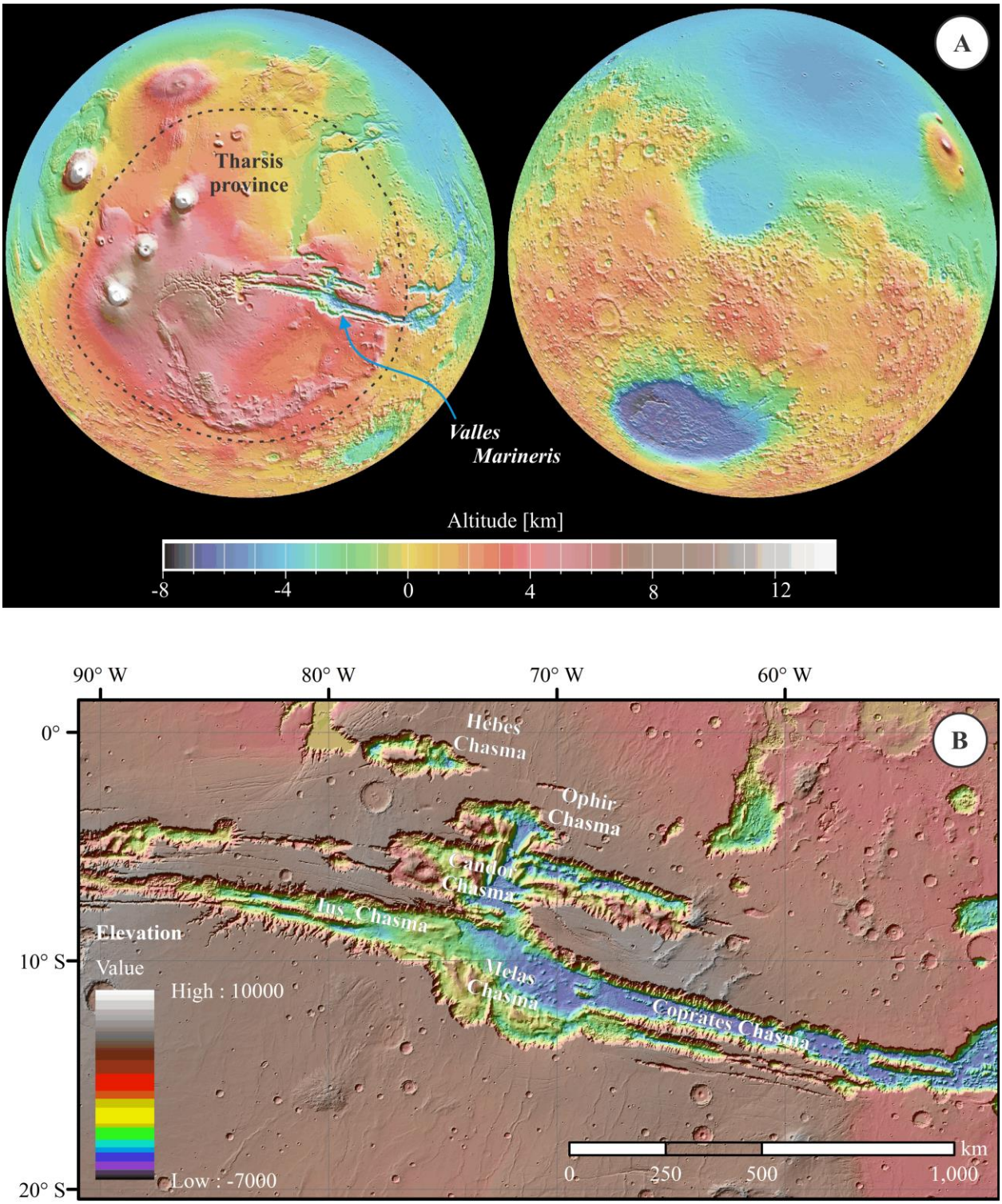

Figure 1-1 (A) Orthographic projection of Mars; dashed line represents the possible outline of the Tharsis province. Modified from: NASA/JPL (B) equirectangular projection of central Valles Marineris shown using Mars Orbiter Laser Altimeter (MOLA) colorized elevation over MOLA Hillshade imagery, resolutions of ~450 m/px and 128 pixels per degree respectively.

The Martian geologic timescale consists of three periods [Hartmann and Neukum, 2001]. The *Noachian* period spans from the accretion of Mars at ~4.5 Ga to 3.7 Ga, ending just after the Late Heavy Bombardment. It is characterized by high rates of cratering and valley formation. The next period is the *Hesperian*, characterized by high rates of volcanism from 3.7 to 3.0 Ga. The *Amazonian* period extends from 3.0 Ga to the present day covering about two thirds of the martian history. This period has less volcanism and cratering than the earlier periods, but shows evidence of widespread glaciations [Carr and Head, 2009].

1.2. The Tharsis province

The Tharsis province is a large Noachian volcanic bulge that rises ~10 km above the martian datum and holds several giant shield volcanoes [Golombek and Phillips, 2010] (Figure 1-1 A). It shows several structural features such as concentric compressional wrinkle ridges on its surface [Okubo and Schultz, 2004; Tanaka et al., 2014] that are evidence of significant deformation due isostatic subsidence from the Tharsis load [Mege and Masson, 1996; Andrews-Hanna, 2012(3)] resulting in a multi-directed stress distribution.

The formation of the Tharsis province involved several processes, such as tensional fracture [Tanaka and Golombek, 1989; Knapmeyer et al., 2006], magmatic activity [McKenzie and Nimmo, 1999; Brustel et al., 2017], chasmata collapses and erosion [Lucchitta, 1978, 1979], and volcanic deposits [Lucchitta, 1990], that altered the surface. These events obscure internal structures such as pre-existing faults that extended to the surface and now can only be inferred from remnants of topographic expressions.

The Tharsis province contains Valles Marineris, one of the greatest structural features of the solar system, which exposed a cross section of the eastern Tharsis province (Figure 1-1).

1.3. Valles Marineris

Valles Marineris is a ~4000 km long and up to 11 km deep system of chasmata, south of the martian equator (Figure 1-1 B) [Sharp, 1973; Blasius et al., 1977]. Its formation spans a large period between the late Noachian and early Hesperian involving multiple stages and faulting that facilitated the collapse of the chasmata and consequently the formation of the walls [Lucchitta et al., 1994; Schultz, 1998; Peulvast et al., 2001; Williams et al., 2003].

Several mechanisms have been proposed to explain the collapse, such as loss of volume by melting of ground ice [Sharp, 1973], dissolution of carbonates in the subsurface [Spencer and Fanale, 1990; Jackson et al., 2011], tension fractures [Tanaka and Golombek, 1989], magmatic activity [Mckenzie and Nimmo, 1999], isostatic subsidence from the Tharsis load [Andrews-Hanna, 2012c], and sediment infill [Fueten et al., 2008]. Possible tectonic activity is inferred from wall retreat observed in the upper parts of the walls however; many features were eroded and erased by the later geomorphological events, such as landslides.

Valles Marineris exposes the interior of the Tharsis province where its walls work as windows allowing observation of the interior structure of the province (Figure 1-1 B). The relief of the walls is divided into several wall morphologies, such as spur and gully, tributary canyons, and landslide scarps [Lucchitta, 1978]. Variations in the height of the walls is partially related to the altitude of the Tharsis and shows a decrease of ~3 km from central Valles Marineris to eastern Coprates [Williams et al., 2003] (Figure 1-1 B). The largest exposed area of Valles Marineris is Coprates Chasma.

The walls of Coprates Chasma expose the stratigraphy of the Tharsis bulge showing the thinning of the volcanic deposits towards the east into older highlands [Williams et al., 2003; Vivianno-Beck et al., 2017]. The variation of the volcanic deposits can be noticed on Ophir Planum adjacent to the north wall of Coprates Chasma. This planum, and many others, has topographic expressions, such as grabens and wrinkle ridges [Watters, 1991, 2004; Zuber, 1995; Okubo and Schultz, 2003, 2004; Hauber et al., 2010; Tanaka et al., 2014; Cole and Andrews-Hanna, 2017], thought to have formed prior to or during the formation of Valles Marineris [Schultz, 1991; Tanaka et al., 2014]. Most of these features cannot be traced directly to the chasmata floor, as they appear disrupted and/or covered by deposits of volcanic and eroded material [Blasius et al., 1977; Lucchitta, 1990; Mege and Bourgeois, 2011].

Studies of some isolated cases show that some of these features appear to be traceable within the walls [Schultz et al., 2007; Cole and Andrews-Hanna, 2017]. Schultz et al. [2007] discussed the geometry of planetary grabens from examples that cross the walls. Recently, Cole and Andrews-Hanna [2017] suggested that wrinkle ridges on the plateau could be linked to ridge formations within the walls.

1.4. Chasma formation and wall morphology

The origin of the Valles Marineris is still conjectural and based on the involvement of diverse processes and events. The current wall morphology is divided into three major wall morphologies: spur and gully, tributary canyons, and landslide scarps [Lucchitta, 1978]. Other morphologies such as pit chains are included in the study as they interact with the wall morphology (Figure 1-2). These morphologies represent the current wall configuration and it was suggested that they are the result of the periodic evolution of the walls where wall retreat and erosional processes play important roles [Peulvast et al., 2001].

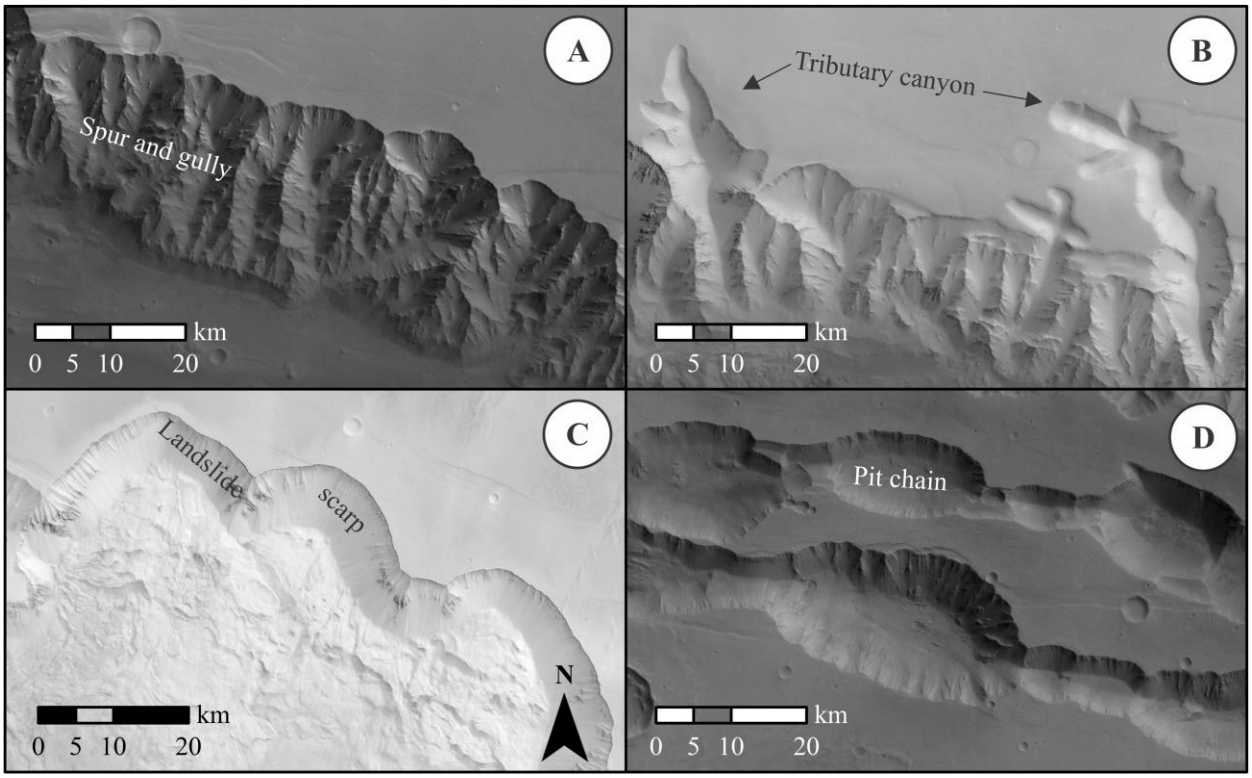

Figure 1-2: Major martian wall morphologies: (A) spur and gully, north wall of Coprates Chasma, (B) tributary canyons, north wall of Ius Chasma, (C) landslide scarps, north wall of Ophir Chasma, and (D) pit chains, south of Coprates Chasma. High Resolution Stereo Camera (HRSC) imagery, resolution ~12.5-50 m/px.

1.4.1. Spur and gully

The spur and gully wall morphology is considered to be the result of gravitational erosion that formed vertically and subparallel, downslope ridges and troughs on the walls (Figure 1-2A). This type of wall morphology appears associated with the absence of catastrophic events [Blackwelder, 1928; Lucchitta, 1978]. Previous researches have considered that the formation of spurs and gullies involves the activity of faults, suggesting that these features, and tributary canyons, are at least partly structurally controlled [Blasius et al., 1977; Peulvast et al., 2001]. However, there have been no detailed studies on the morphology of these features in Valles Marineris.

This wall morphology shows that gullies near the top of the walls have steeper attitudes, subjacent to them debris flows appear at the floor as evidence of the erosion. Comparison of terrestrial debris flows at the Antarctic [Calkin, 1971] with martian debris flows showed a resemblance interpreted as mudflows, which implies the melting of ground ice, as suggested by Sharp [1973].

The formation of spurs and gullies is considered to occur at a slow rate making this wall morphology vulnerable to other events such as landslide collapses that can destroy them [Lucchitta, 1979]. The spurs and gullies might reappear through the breakaway scarp possibly involving pre-existing structures. These renewed spur and gully structures and the ribs formed at the upper walls of the landslides have characteristics related to the erosional process such as smooth talus slopes [Lucchitta, 1978].

1.4.2. Tributary canyons

Tributary canyons are usually solitary valley channels with blunt heads and smooth walls. Most of the tributary canyons appear to have low gradients along the extent of their floors that merge with the main trough at the level of its floor [Lucchitta, 1978] (Figure 1-2B). Strong structural control is evident in their development based on aligned straight segments.

The walls of Ius Chasma at western Valles Marineris have complex networks of tributaries. Most are rectilinear, suggesting that some of them follow faulting and joint systems [Lucchitta, 1978; Davis and Golombek, 1990] as seen from the graben on the adjacent plateaus. The northern walls of Ius are a good example of tributary canyons associated with visible grabens (Figure 1-1 and Figure 1-2B). The southern walls show no evidence of faulting being associated with joint systems [Davis and Golombek, 1990].

1.4.3. Landslide scarps

Landslides are interpreted to occur mainly in fault scarps bounding the Martian chasmata, leaving a characteristic amphitheater-shaped depletion zone on otherwise straight sections of the walls (Figure 1-2C). The occurrence of the landslide leaves evenly spaced small ribs that form at the uppermost layer immediately below the plateau. The eroded material is deposited at the base of these recessed sections burying the walls locally [Lucchitta, 1978, 1979; Schultz, 2002] (Figure 1-2C). Landslides within Valles Marineris do not provide evidence of either active tectonics or wet conditions in the martian past. These landslides, especially large landslides, expose porous materials in the valley walls where this condition would trigger the collapse [Lucchitta, 1979; Williams et al., 2003]. The local presence or absence of this weak material may locally influence the stability of the chasmata walls relative to their elevation on the walls.

1.4.4. Pit chains

The development of the pits has been attributed to collapse, possibly including the presence of groundwater [Tanaka and Golombek, 1989]. They are not clearly associated with local tectonism nor with erosion [Davis and Golombek, 1990]; yet the texture of their walls is similar to that observed on scarps (Figure 1-2D). Pits at western Valles Marineris appear to follow the E-W trend of existing shallow grabens, which suggest structural control [Davis and Golombek, 1990].

1.5. Superficial structures

Various structural features, such as grabens and wrinkle ridges, are observed on the plateau and have been studied [Okubo and Schultz, 2004; Tanaka et al., 2014]. Their spatial distribution has been analyzed and modelled, the wrinkle ridges being concentric to the Tharsis province and grabens distributed radially surrounding the center of Tharsis [Okubo and Schultz, 2004; Dimitrova et al., 2006; Knapmeyer et al., 2006].

1.5.1. Planetary grabens

Grabens are thought to be symmetrical structures with a defined floor that contrasts with the surface due its meters-scale depth. Martian grabens are not always fresh and well defined due the occurrence of erosional processes and late deposits of volcanic flows that make them difficult to recognize (Figure 1-3A) [Schultz et al., 2007].

Symmetric graben models suggest keystone collapse wedges that intersect at the subsurface. Hypotheses of the formation of planetary grabens are based on terrestrial canyonlands using them as templates for simple planetary grabens and their near surface, extensional geometry [Golombek, 1979; Golombek and McGill, 1983; Tanaka and Golombek, 1989; Banerdt et al., 1992].

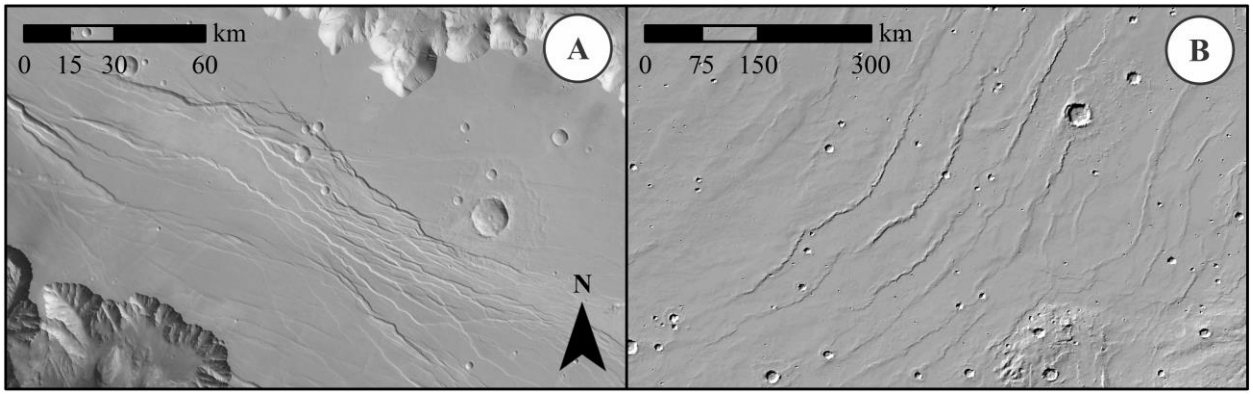

Figure 1-3: (A) Grabens, western Ophir Planum shown using HRSC imagery (B) wrinkle ridges, Solis Planum shown using MOLA Hillshade imagery.

Models of martian symmetrical grabens involve the concept of thin-skinned models comparable to models from Earth. However, models of thin-skinned tectonics are problematic with loading configurations for Tharsis as the strain would be accommodated at greater depths below the graben wedges [Banerdt et al., 1992; Schultz et al, 2007]. Findings of planetary grabens with tilted floors led to the reconsideration of previous graben models suggesting an asymmetric geometry of the structure [Schultz et al., 2007]. A fault network that penetrates deeper through the layers is proposed for these graben models. Such grabens are compared to similar lunar grabens that seem to cut through diverse geologic units [Schultz et al., 2007].

1.5.2. Wrinkle ridges

Wrinkle ridges may originate from fault-related folds in the underlying Noachian crust appearing as surface expressions concentric to the Tharsis province (Figure 1-3B) [Watters and Maxwell, 1986; Anderson et al., 2001]. Difference in the geometry between Hesperian and Noachian wrinkle ridges is evidence of possibly different mechanical origins [Mangold et al., 1998]. Wrinkle ridges are recognized for their low asymmetric rise in cross section that might result from faulting in ice-poor horizons. It has been suggested that symmetrical ridges possibly originated on ice-rich horizons [Okubo and Schultz, 2003]. These features are thought to originate from compressive stresses based on a thick-skin and thin-skin tectonics comparison. The thick-skin tectonic model assumes that the entire crust is deformed by major thrusts [Zuber and Aist, 1990] whereas the thin-skin mechanism is based on initially folded volcanic layers in the mega regolith [Watters, 1991] that later faulted.

Overall, the development of grabens and wrinkle ridges is the result of regional conditions reflecting lithosphere-scale deformational processes, rather than slipping mid-crustal detachment [Okubo and Schultz, 2003].

1.6. Datasets: Imagery and Digital Elevation Models (DEMs)

The study relied on the use of images in order to identify the morphological and structural features on the surface of the walls and the plateau (Figure 1-4A). These datasets helped in the qualitative analysis of the areas studied. The use of DEMs was necessary in order to quantify the observed morphology of the features (Figure 1-4 B&C). The available DEMs have horizontal resolutions from ~450 m/px (Figure 1-4B) to ~18 m/px (Figure 1-4C). The use of these DEMs depended in the quality of their coverage. The MOLA DEM covers the whole surface of Mars without presenting problems although its resolution limits the interpretation of small-scale features (Figure 1-4D). Nonetheless, in-home computed DEMs from the Context Imager (CTX) are available. These DEMs have higher resolution and provide more information about small-scale features. However, they required a selection and adjusting process due their lack of alignment with the Martian datum and suffer from the presence of artifacts such as holes and spikes in them (Figure 1-4E). These artifacts limit the use of the CTX DEMs to visual purposes since their existence can alter any geometrical measurement and statistical analysis. The CTX DEMs were filtered in order to remove the spikes and only those of good quality (e.g. Figure 1-4C) were selected to be adjusted to their proper location with respect to the MOLA DEM. The CTX DEMs used are listed in appendix A.

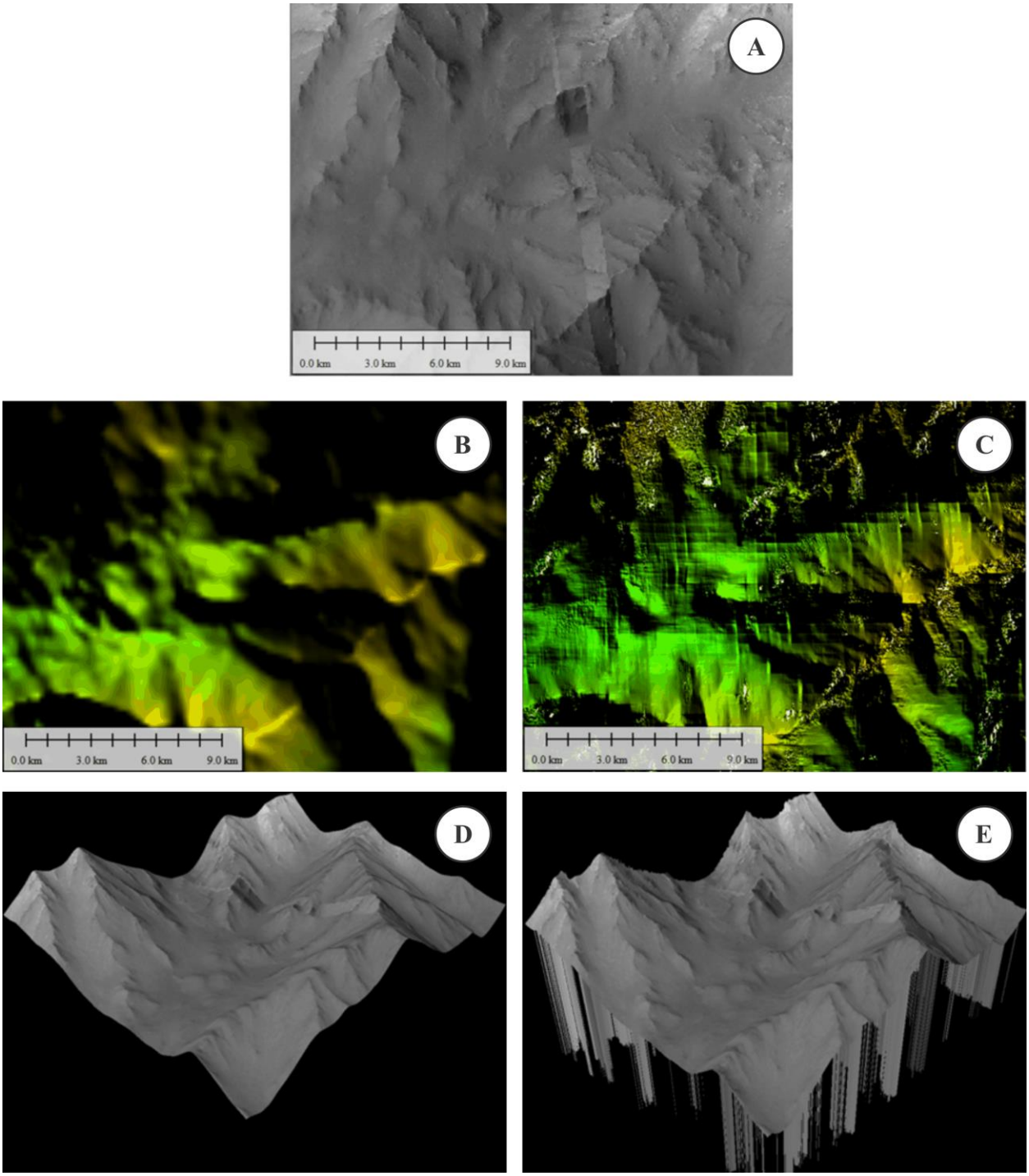

Figure 1-4: Section of spur and gully wall morphology covered using (A) HRSC Imagery, resolution of ~12.5 m/px (B) MOLA DEM, resolution of ~450 m/px (C) CTX DEM, resolution, ~18 m/px. 3D projection of the same section of the spur and gully wall morphology using (D) MOLA DEM and (E) CTX DEM. Notice the presence of holes and spikes on the CTX DEM.

1.7. Purpose of this study

This study focuses in the formation and origin of topographic expressions such as grabens and wrinkle ridges visible on the Martian surface as well as on the morphology of the walls of central Valles Marineris. The origin of these features is conjectural however, I will pursue a different approach to understand them by characterizing them and by modelling specific cases observed within central Valles Marineris. These cases represent a connection between pre-existing structures within the Tharsis and chasma-forming faults with visible structures seen on the surface of the surrounding plana.

Chapter 2 : Large Wrinkle Ridges

Wrinkle ridges are topographic expressions formed along the diverse plana of the Tharsis province [Schultz and Tanaka, 1994; Zuber, 1995; Schultz, 2000; Okubo and Schultz, 2003, 2004; Watters, 2004]. Their relative high topographic relief makes of them visible structures on the surface. In this chapter, three special ridge formations located on Ophir Planum are examined. Due to their large relief and similar morphology they are classified as Large Wrinkle Ridges. I present an elastic dislocation model that will explore their formation,

2.1. Introduction

Wrinkle ridges have been studied using photoclinometrically-derived topography from Viking Orbiter images [Golombeck et al., 1991; Watters and Robinson, 1997, 2000] but the acquisition of new data from Mars Orbiter Laser Altimetry (MOLA) allowed for better topographic profiles to test the Viking-based elevation models and increased the discussion about the origin and nature of the Tharsis wrinkle ridges [Smith et al., 1999]. Datasets from HRSC and the Context Imager (CTX) have higher resolutions [Broxton and Edwards, 2008; Gwinner et al., 2016] that improved spatial analysis and modelling of these structures to understand their origin [Schultz and Watters, 2001; Okubo and Schultz, 2003, 2004; Watters, 2001, 2004].

These and other landforms formed by martian tectonic activity are visible on the surface of the Tharsis province but many of them are now hidden by later deposits (Figure 2-1) [Watters and Maxwell, 1986; Lucchitta, 1990]. The observed lithology on the plana that surround central Valles Marineris varies from volcanic deposits to older (Figure 2-1A) [Watters and Maxwell, 1986; Tanaka et al., 2014].

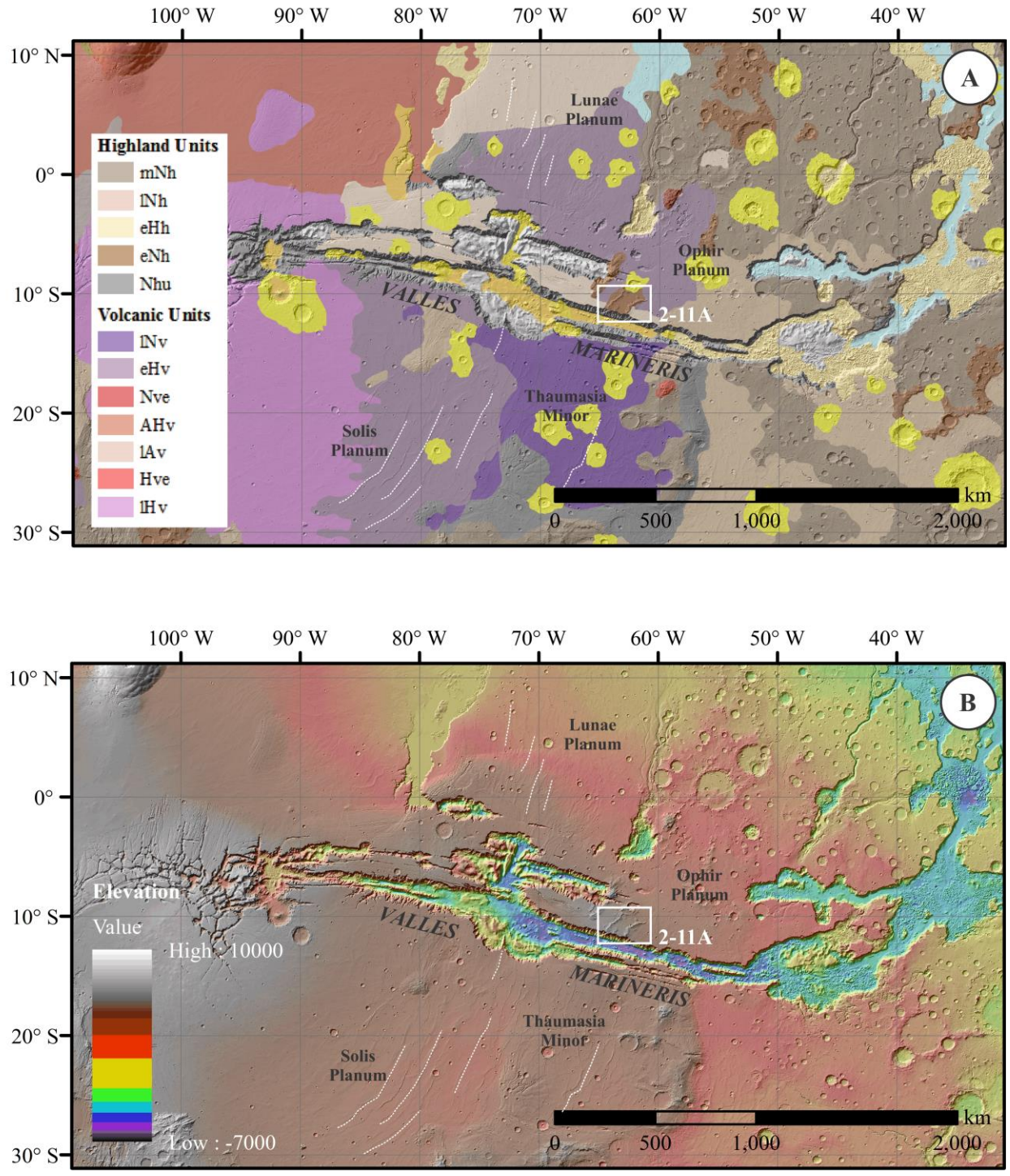

Figure 2-1: Eastern plana of the Tharsis province surrounding Valles Marineris (A) geological map modified from Tanaka et al. [2014]. Labels refer to the stage of the period (e: early, m: mid, l: late), the period in the Martian geological timescale (N: Noachian, H: Hesperian, A: Amazonian), and lithological unit (h: highland, u: undivided, v: volcanic, ve: volcanic edifice) (B) MOLA-HRSC blend colorized elevation, resolution ~200 m/px. Dashed grey lines marked the trend of some wrinkle ridges. Location of Figure 2-11A as indicated.

2.1.1. Distribution and formation of wrinkle ridges

Most of the wrinkle ridges that surround Valles Marineris appear sub-perpendicular to the main trend of the chasmata [Okubo and Schultz, 2003; Tanaka et al., 2014] (Figure 2-2). They curve over their length mimicking the concentric outline of the Tharsis province [Okubo and Shultz, 2003] with extents of up to hundreds of kilometers. Several wrinkle ridges appear distributed evenly spaced as quasilinear topographic expressions within clustered regions [Watters, 1988; Schultz and Tanaka, 1994; Okubo and Shultz, 2003, 2004].

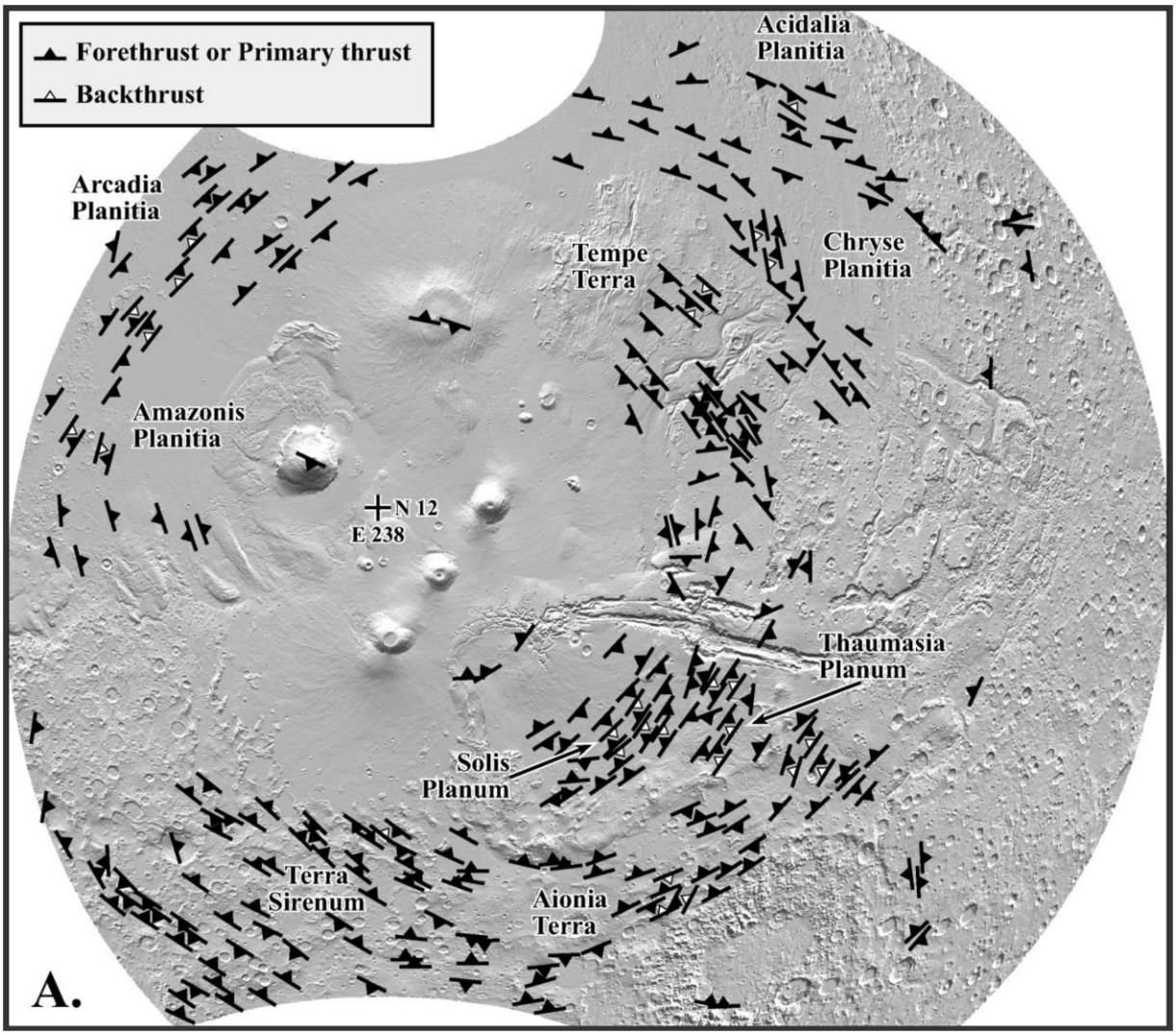

Figure 2-2: Representative thrust-fault strike and dip directions for wrinkle ridges within the western equatorial region of Mars, modified from Okubo and Schultz [2004].

Wrinkle ridge distribution is similar to the strain distribution generated from the load compression of the Tharsis bulge [Mege and Masson, 1996] (Figure 2-2). Compressional stresses are higher near the outer edge of the province [Montgomery et al., 2009]. Their origin is presumed from compressional tectonism which suggests them as expressions of underlying thrust faults [Schultz and Tanaka, 1994; Zuber, 1995; Mege and Masson, 1996; Okubo and Shultz, 2003, 2004; Watters, 2004; Cole and Andrews-Hanna, 2017] that involves later folding of the upper layers. The folding is expressed at the surface as a high relief topography with a characteristic asymmetric morphology [Lucchitta, 1978; Sharpton and Head, 1988; Watters, 1988; Golombeck et al., 1991]. The presence of backthrust suggests that the fault formation process is complex [Okubo and Schultz, 2004] and possibly consisting of more than one stage.

2.1.2. Morphometry

The morphology of wrinkle ridges is typically a lobate topography composed of two landforms, a narrow ridge of 2-5 km width superimposed onto a broad low relief arch that is 10-20 km wide (Figure 2-3) [Strom, 1972; Bryan, 1973; Maxwell et al., 1975; Watters, 1988, 2004] making the wrinkle ridges asymmetric in profile. The asymmetry is considered a key morphologic element as it can be a possible indicator of the vergence of the underlying fault (Figure 2-3) [Watters, 1988, 2004].

The relief of wrinkle ridges elevates from 50-300 m over their respective surface location, where the highest elevated part of it is associated with the superimposed narrow ridge (Figure 2-3) [Watters, 1991, 2004; Schultz, 2000; Okubo and Schultz, 2004]. However, their relief can appear degraded due to erosional processes similar to cases observed in grabens [Watters, 2004; Hauber et al., 2010].

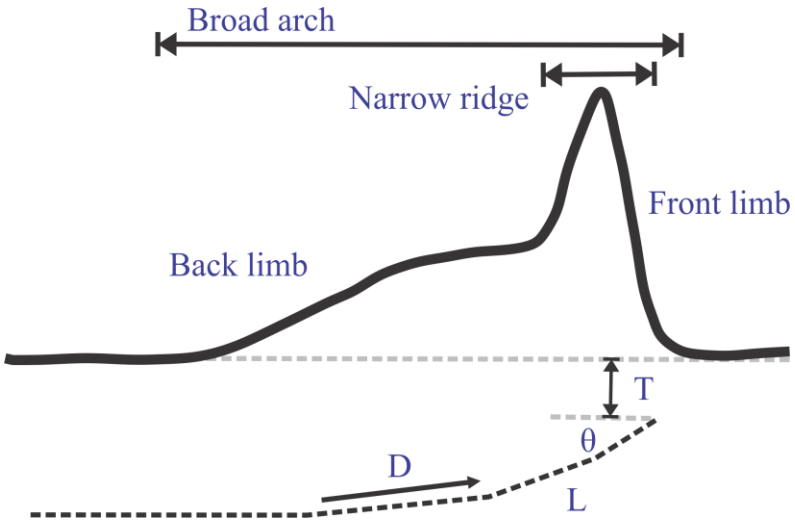

Figure 2-3: Schematic topographic profile of a wrinkle ridge possibly formed by an underlying listric fault that flattened into a décollement. The fault is segmented having dip angle θ, a depth T from the surface, and a total displacement or slip D for each segment of the fault. Significant vertical exaggeration to enhance clarity.

2.2. Previous studies

2.2.1. Hypotheses for wrinkle ridge formation

Previous studies of wrinkle ridges used several morphological elements to estimate models to infer a possible origin of formation [Watters, 1991, 2004; Zuber, 1995; Schultz, 2000; Okubo and Schultz, 2004]. These models consider certain morphological characteristics such as width, relief, and asymmetry to be associated with the location of the blind fault [Zuber, 1995], the lithology [Okubo and Schulz, 2003, 2004], and the geometry of the underlying fault [Okubo and Schultz, 2004; Watters, 2004].

Zuber [1995] and Schultz [2000] suggest that the formation of wrinkle ridges is affected by the lithology and the location of the fault, considered a singular blind fault. Okubo and Schultz [2004], and Watters [2004] suggest a more complex shape for the blind fault, giving it listric geometry. Both agree that the geometry of the underlying fault involves the merging into a horizontal decollement, as suggested by Mangold et al. [1998].

Okubo and Schultz [2004] discussed the nature of wrinkle ridges on Mars in general, suggesting a formation influenced by the competence of the underlying strata (Figure 2-2). They propose a correlation between the presence of a backthrust and shallow volatile-rich layers, and further clarify that the presence of these superficial volatiles is not a requirement for the formation of primary wrinkle ridges. Watters [2004] shows several cases of wrinkle ridges within Solis Planum and Lunae Planum, with similar morphologies among the wrinkle ridges, although differences in scale are noticed showing that wrinkle ridges on Solis Planum are approximately twice as high as those on Lunae Planum.

2.2.2. Quantitative models of wrinkle ridge formation

The description of the nature of wrinkle ridges relies mostly on qualitative interpretations from surface distributions and simulated kinematics [Watters, 1991; Knapmeyer et al., 2006]. Recent studies [Okubo and Schultz, 2004; Watters, 2004] are based on elastic dislocation models that simulated the deformation of the surface by possible underlying faults. The models iteratively adjust the fault parameters associated with the structure in order to replicate the current topography. Schultz [2000] introduced a model that pre-defined underlying blind thrust faults with dips of ~30°, to explore a general formation. Later models displayed a more complex underlying fault geometry [Okubo and Schultz, 2004; Watters, 2004]. Watters [2004] considered a segmented thrust fault that varies the dip for each segment of the fault (e.g. 30°, 10°, 5°, 0.01°) as it extents and merges into a ~4.5 km deep horizontal decollement (Figure 2-3). The depth of the decollement is comparable to stratigraphic results by Ori and Karna, [2003], who explored the exposed materials within the walls of Coprates, Candor, and Ophir chasmata. Okubo and Schultz [2004] assumed a similar listric geometry that dips at ~30° near the surface and the addition of back thrust to represent secondary faulting.

Recent studies [Cole and Andrews-Hanna, 2017] pursue a different approach trying to connect the fault planes involved in the formation of wrinkle ridges with ridge formations that extend from the walls of Valles Marineris.

This study focuses on the origin and formation of wrinkle ridges using spatial analysis of digital elevation models (DEMs) and imagery datasets. Some previously examined wrinkle ridges are sampled as reference sets for comparison with some anomalous larger topographic features.

2.3. Methodology

2.3.1. Datasets and locations

General inspection relied on the Mars Orbiter Laser Altimetry (MOLA) DEM, with a resolution of ~450 m/px [Smith et al., 1999], to determine areas with representative and well-defined wrinkle ridges (e.g. Lunae Planum, Solis Planum, Thaumasia Minor, and Ophir Planum). Closer inspection required DEMs with higher resolution leading to the use of HRSC DEMs, resolution 50-150 m/px [Gwinner et al., 2016], which provided better morphometric results. The HRSC DEMs cover areas like Solis Planum, Thaumasia Minor, and Ophir Planum, although the datasets do not cover areas such as Lunae Planum that were covered using the MOLA DEM.

Inspection of the walls of Valles Marineris required DEMs with higher resolution than HRSC. The DEMs were made from CTX imagery using routines of stereo projection [Broxton and Edwards, 2008], resulting in DEMs of the overlapped area of the available imagery with planar resolution of ~18 m/px and vertical resolution of ~0.1 m/px. The vertical resolution of MOLA and HRSC DEMs is ~1 m/px [Smith et al., 1999].

Examination of the surface used diverse mosaic datasets created to determine differences in texture among the wrinkle ridges facilitating their interpretation. These mosaics were made using HRSC and CTX Imagery [Broxton and Edwards, 2008; Gwinner et al., 2016], with resolutions of ~12.5-50 m/px and ~6 m/px, respectively. The inspection of certain locations depends on the mosaics using CTX within the walls of Valles Marineris, and HRSC for a general analysis of the overall surface of Valles Marineris.

2.3.2. Topographic analyses and selection of wrinkle ridges

Topographic analyses include the examination of the morphology of the wrinkle ridges by adjusting the coloring of the elevation of the DEMs to a short range in order to enhance their relief (Figure 2-4A). This color adjustment revealed which wrinkle ridges within the selected areas have well-defined morphology (i.e. relief, width, and extension). Another component is the aspect of the surface calculated using the Augmented Visualization of Attitude (AVA) tool [Minin et al., 2015] which facilitates the interpretation of changes in the attitude of the morphology of wrinkle ridges such as the limbs using a schematic color-wheel (Figure 2-4B). The AVA tool calculates the attitude of a plane centered on a specific pixel; this is calculated for each pixel of the used DEM. The results are associated with the corresponding pixel where the plane was centered assigning the color based on the pole of the plane on a color-coded Schmidt net. The intensity of the color uses the dip value, where shallower dips appear dull nearly grayish (Figure 2-4B). This technique improved the process of selection of wrinkle ridges considering only those that show a well-defined topography and consistent limbs (i.e. invariable attitude).

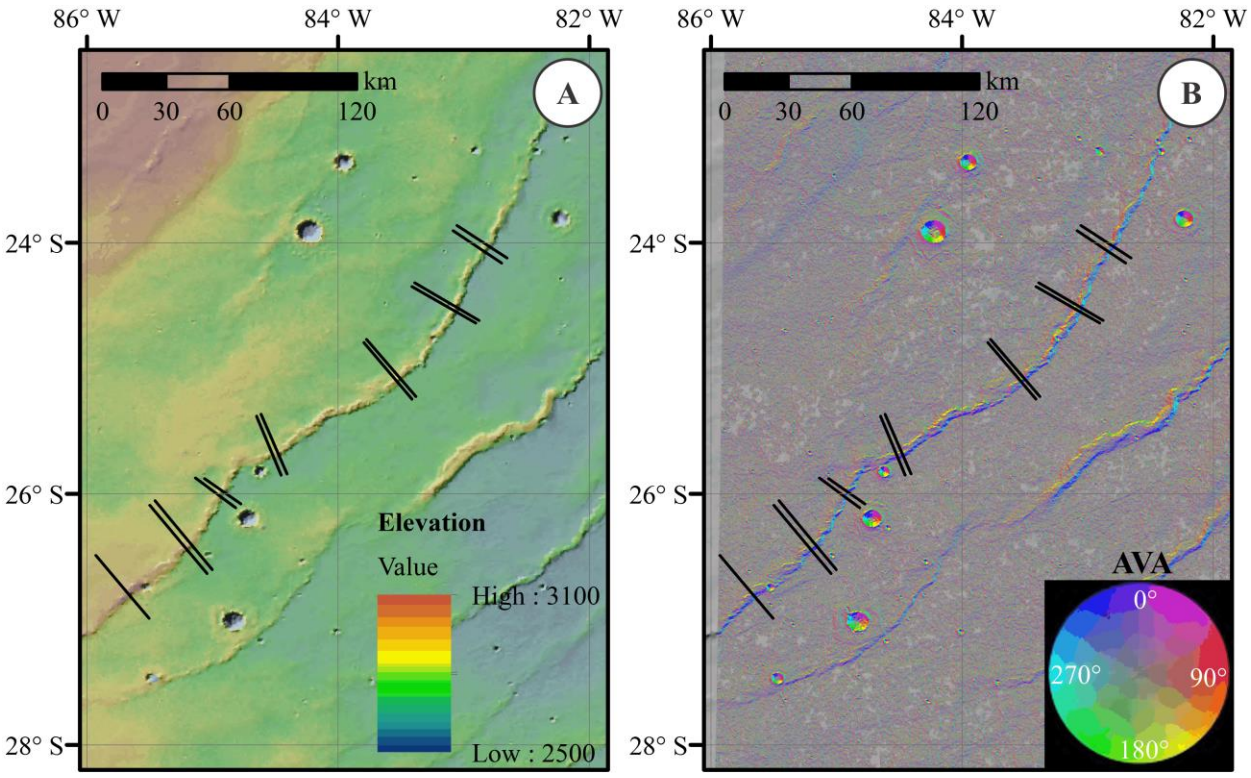

Figure 2-4: Example of a wrinkle ridge within Solis Planum shown using HRSC data with resolution ~75m/px. (A) DEM (B) AVA color-scheme with respective orientation; black solid lines mark the location of the topographic profiles.

The results from the AVA tool depend on the size of the kernel that represents a plane use to calculate the attitudes. It was decided to use a kernel size of 3x3 pixels to obtain a more detailed illustration of the attitude. A 3x3 kernel defines the smallest possible plane that can sample the surfaces under study using the resolution of the DEM.

The selection of wrinkle ridges considers the amount of erosion using the imagery mosaics, since erosion can obscure or distort the attitude of the limbs, limiting the accuracy of the morphometry (i.e. relief, width, and extension). Wrinkle ridges with lengths of 50-150 km are preferred considering that their greater length could indicate a more consistent topography that would improve the results.

One special case is a wrinkle ridge that extends along the transition of the geological units on Lunae Planum. This transition occurs along a length of ~50 km where the early Hesperian volcanic deposit thins until it merges with the early Hesperian highland volcanic sequence (i.e. decreases from ~3 km to <1 km) [DeHon, 1985, 1988; Frey and Grant, 1990; Robinson and Tanaka, 1990; Watters, 1991].

Any possible change in the morphology of the wrinkle ridges was analyzed along their extent using topographic profiles (Figure 2-4). The profiles were measured covering the majority of the extension of the wrinkle ridges orientating them from west to east. In order to analyze the profiles properly a reference point is necessary to align them to the front limb, as it appears more consistent than the back limb. The profiles show that the back limb has a variable width (Figure 2-4A). Some profiles are adjusted as well to a similar elevation to compare the morphology of the wrinkle ridges along their extent.

2.4. Wrinkle ridges surrounding Valles Marineris

2.4.1. North of Valles Marineris

Three different wrinkle ridges were selected within Lunae Planum (LP), two formed on different geological units (i.e. early Hesperian volcanic deposit and early Hesperian highland [Witbeck et al., 1991; Tanaka et al., 2014]) and the third one extending between both units (Figure 2-5). The early Hesperian volcanic unit of this planum has been interpreted as a flood basalt [Greeley and Spudis, 1981; Mouginis-Mark et al., 1992] with a thickness that varies from <1 km to ~3 km [DeHon, 1985, 1988; Frey and Grant, 1990; Robinson and Tanaka, 1990; Watters, 1991].

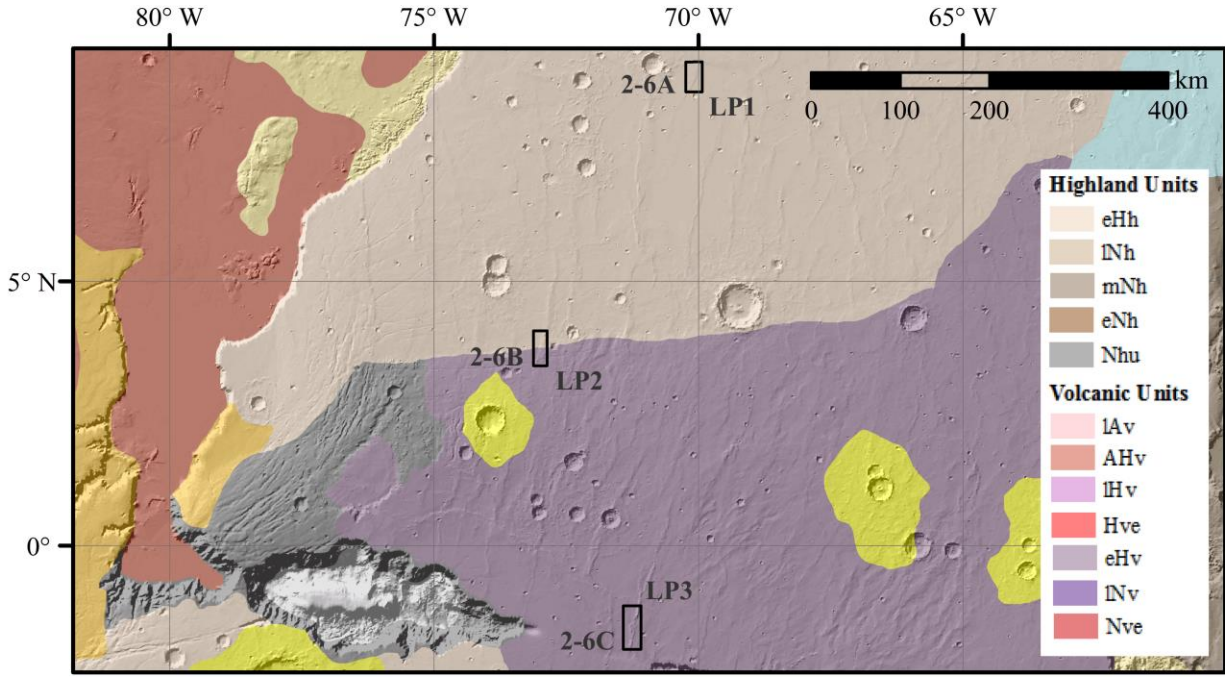

Figure 2-5: Measurements on selected areas of LP. Geological map modified from Tanaka et al. [2014]. Labels mean stage (e: early, m: mid, l: late), period (N: Noachian, H: Hesperian, A: Amazonian), and lithological unit (h: highland, u: undivided, v: volcanic, ve: volcanic edifice).

The results from the topographic profiles of the wrinkle ridge LP1 on the highland show a morphology of ~75 m in relief and ~12 km in width along an extent of ~100 km (Figure 2-6 A&D). Measurements for the wrinkle ridge LP3 on the volcanic deposit show similar morphology to LP1, differing with LP3 being ~250 m in relief and having opposite asymmetric orientation (Figure 2-6 C&D).The profile on LP3 was extended beyond the CTX image to observe the full width of the wrinkle ridge. The new profile shows that the wrinkle ridge has a broad arch of ~25 km, which was almost unrecognizable on the surface due the shallow slope of the back limb (Figure 2-6D).

LP2 shows a similar morphology over its extension along the transition but a difference in scale is noticed. The changes include an uplift of ~1 km towards the volcanic deposit while narrowing the broad arch of the wrinkle ridge. The relief of the wrinkle ridge appears to decrease ~20 m over a length of ~40 km as it passes across the transition onto the volcanic deposit (Figure 2-6 B&D).It is suggested that the changes in morphology of LP2 along the transition are associated with the lithology. Lithological influence is inferred from the difference in scale of the morphology of the wrinkle ridges within this region.

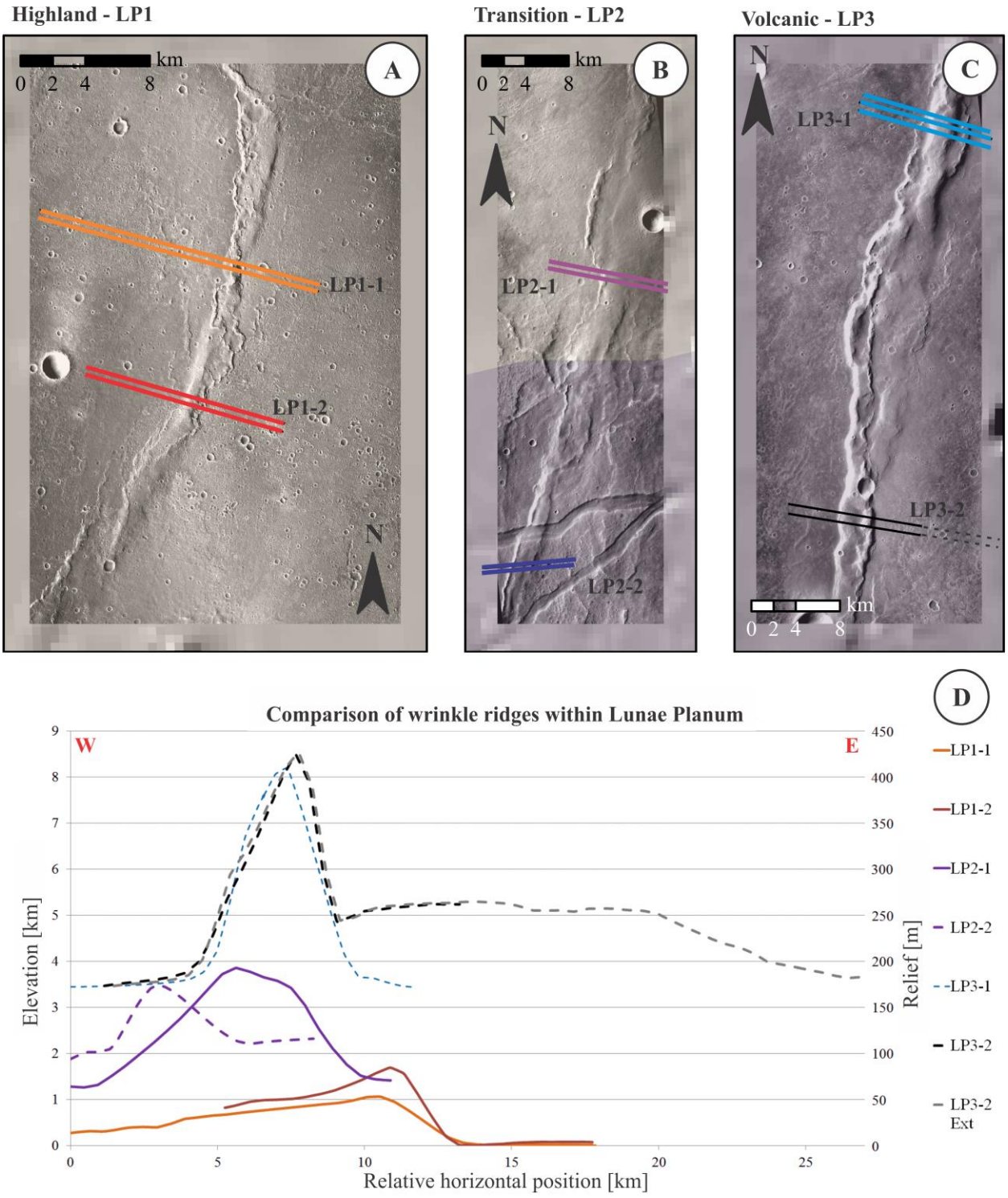

Figure 2-6: Comparison of wrinkle ridges within Lunae Planum using CTX Imagery, resolution ~6 m/px, from orbits (A) P06_003210_1887_XN_ 08N070W (B) F02_036439_1843_XN_04N073W (C) B16_016053_1795_ XN_00S071W. The color-shade represents their geological unit from Tanaka et al. [2014]. (D) Comparison of topographic profiles. 60x vertical exaggeration (V.E.), elevation scale in km on the left is valid for the leftmost end of the profiles, relief scale in meters is valid for the overall profile. Solid lines for profiles over highlands (eHh) and dashed lines for profiles over volcanic deposits (eHv).

2.4.2. South of Valles Marineris

The plateaus that surround southern Valles Marineris (i.e. Solis Planum (SP), Thaumasia Minor (TM), and a section to the East of Thaumasia Minor (ETM)) were analyzed based on their extent, surface lithology, and morphology of their wrinkle ridges (Figure 2-7). Topographic profiles cover the most well developed sections of the wrinkle ridges where the morphology is clearly visible using the AVA tool results. This is made to obtain several profiles that sample the wrinkle ridges in order to obtain their average morphology.

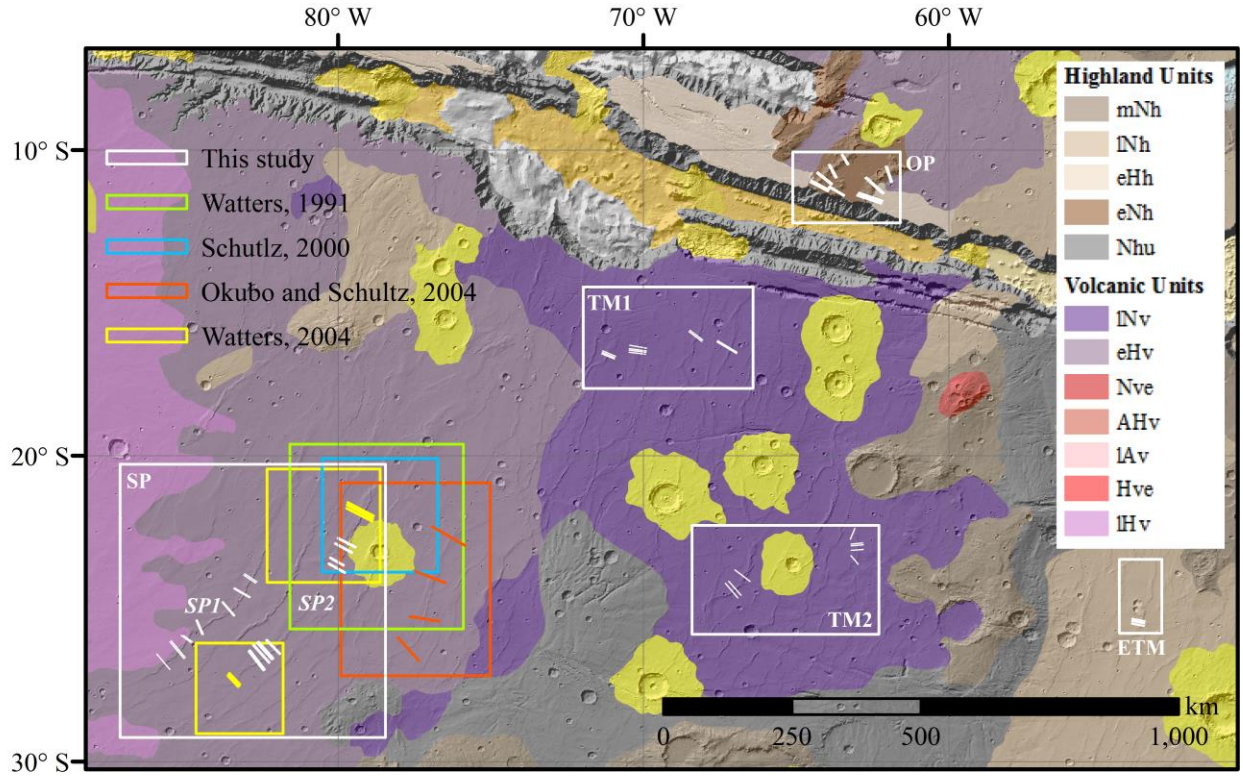

Figure 2-7: Wrinkle ridge topographic profile measurements on selected areas of SP, TM, ETM and Ophir planum (OP), including previous studies. Geological map modified from Tanaka et al. [2014]. Labels mean stage (e: early, m: mid, l: late), period (N: Noachian, H: Hesperian, A: Amazonian), and lithological unit (h: highland, u: undivided, v: volcanic, ve: volcanic edifice).

The surface of Solis Planum exposes a lithology classified as early Hesperian volcanic deposit, where two large wrinkle ridges were selected based on their length extent of ~300 km each, labelling them as *SP1* and *SP2* (Figure 2-7). Both appear as slightly curved lineations that

change trend from ~045° to 020° as they approach Valles Marineris (Figure 2-4) with an apparent consistent morphology along their extent based on results from the AVA analysis. Comparison of topographic profiles of SP1 shows a consistent morphology with small variations reaching a maximum relief close to the midsection of its extent (Figure 2-8A). An average of the measurements was calculated, resulting in a relief of ~200 m and ~3 km width, superimposed on a width of ~12 km.

SP2 shows morphology comparable to previous studies [Watters, 2004] without the presence of an apparent double arch mentioned in that study. The topographic profiles show increasing width and relief of the wrinkle ridge towards north. The relief varies from ~100 m to 300 m (Figure 2-8B). The average morphology of SP2 is ~175 m in relief and ~15 km in width similar to SP1. Both results of SP1 and SP2 show them to be continuous, long wrinkle ridges inferred from their consistent topographic expression along length, implying that each one represents a fault of large extent.

Shorter wrinkle ridges appear towards northeast on Thaumasia Minor, a Late Noachian volcanic deposit [Tanaka et al., 2014]; they appear visibly disrupted, which made the selection of consistent sections difficult to measure. Yet measurements of the topography determined smaller sections of various wrinkle ridges along the extent of the plana (Figure 2-9A).

Topographic profiles show that the relief of the TM wrinkle ridges is within a range of 100-200 m over widths of 5-10 km. Their resemblance in morphology indicates possible similar underlying structures even though they do not share the same asymmetric orientation on their relief (Figure 2-9B). It is suggested that this could be the result of diverse multiple faults that cross among each other based on previous suggestions of back thrusting [Okubo and Schultz, 2003].

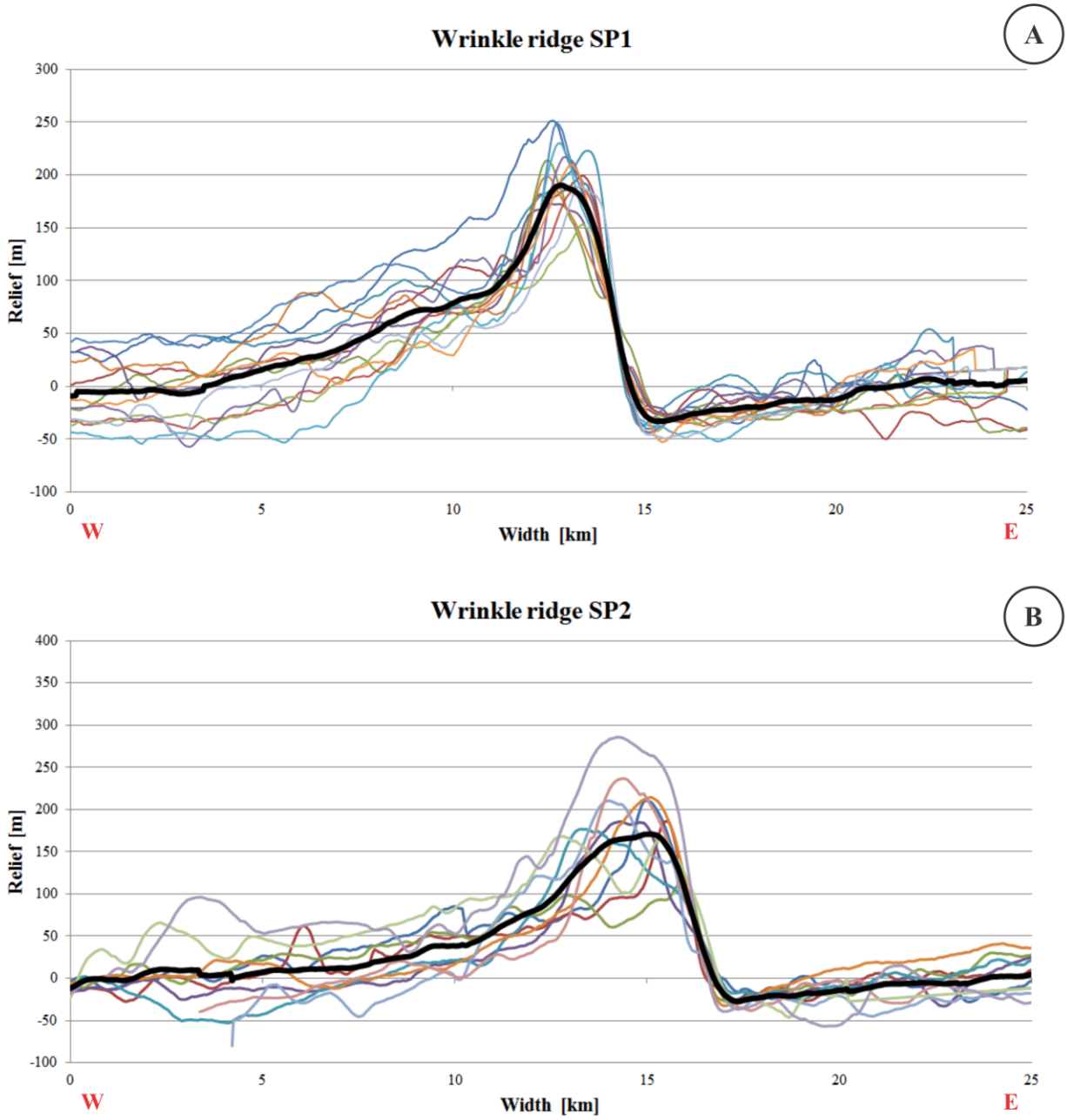

Figure 2-8: Comparison of topographic profiles of wrinkle ridges (A) SP1 and (B) SP2. 50x V.E. Locations of profiles appear on Figure 2-7. Thick black line is the average of all the measured profiles.

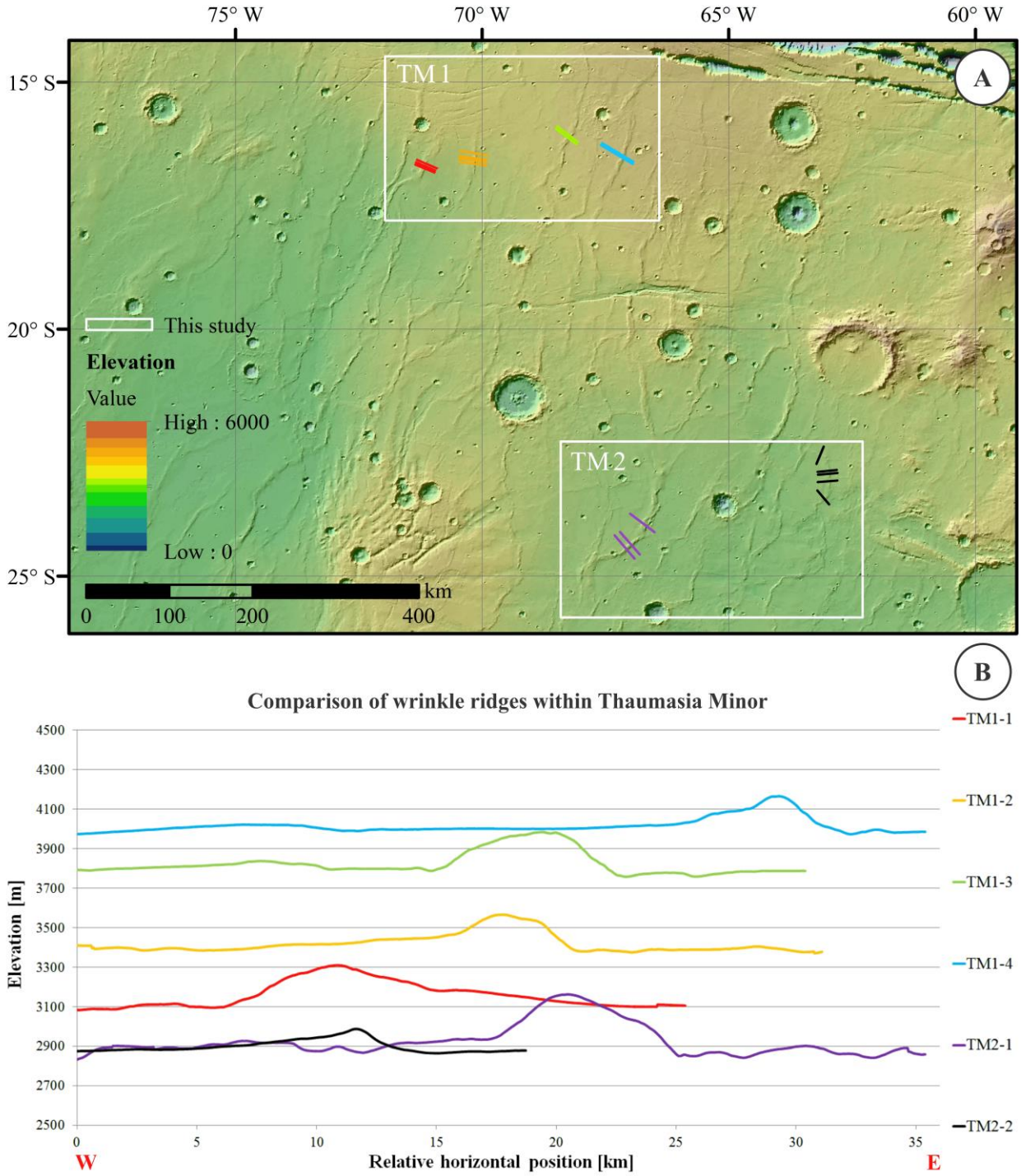

Figure 2-9: (A) Thaumasia Minor showing the measured topographic profiles over wrinkle ridges and a (B) comparison of the profiles at their actual elevation on the plateau. 60x V.E. Profiles are colour coded to correspond with their locations on the map.

A wrinkle ridge in ETM at the edge of the Tharsis province was measured in order to compare wrinkle ridges from different lithologies and locations (Figure 2-7). ETM is located ~3 km below the elevation of TM extending over a Late Noachian highland (Figure 2-10) [Ori and Karna, 2003; Williams et al, 2003; Tanaka et al., 2014]. The profiles show a superimposed narrow ridge of ~200 m in relief extending ~4 km wide, over a broad arch of ~16 km.

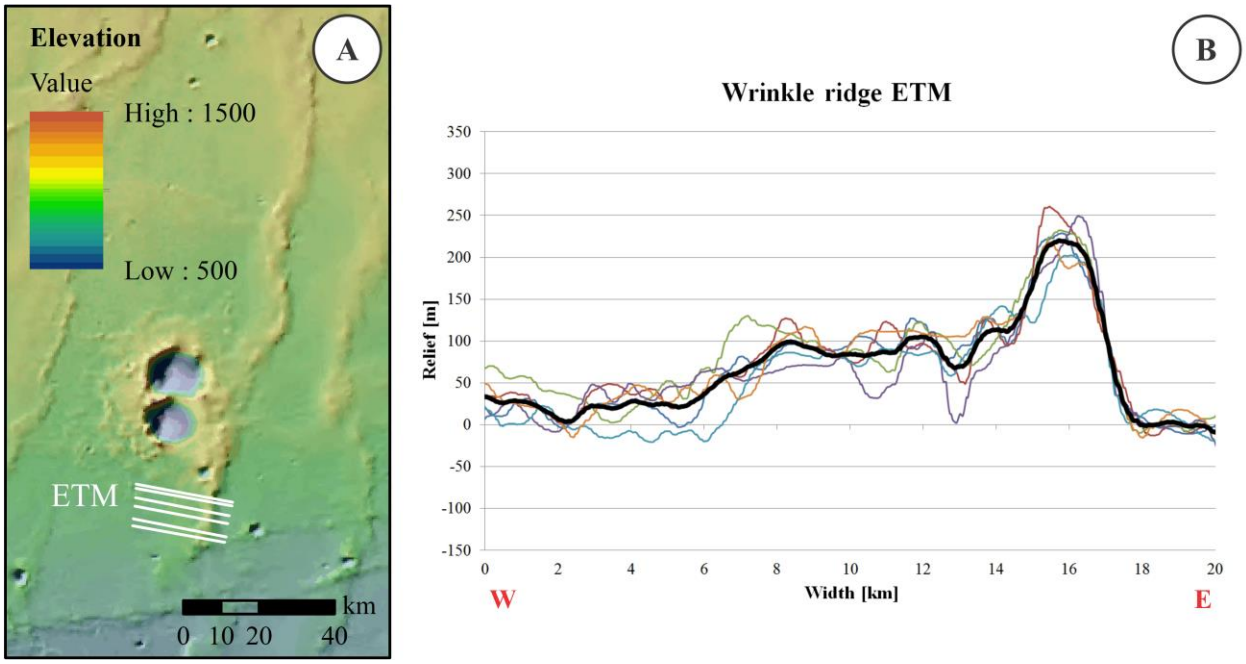

Figure 2-10: (A) East of Thaumasia Minor showing the measured topographic profiles over ETM and a (B) comparison of the measured profiles. 40x V.E. Thick black line is the average of all the measured profiles.

The results indicate that wrinkle ridges that surround Valles Marineris have similar morphology quantified with a relief of up to ~300 m and widths as wide as ~20 km. However, other ridge formations are observed on various plana of the Tharsis bulge not far from Valles Marineris. This is a case selected to be study within Ophir Planum (Figure 2-7) and will be analyzed in further sections.

2.5. Topographic expressions within Ophir Planum

2.5.1. Anomalous topographic ridges

Ophir Planum (OP) has three high relief ridges that trend ~045° (Figure 2-11A) classified as early Noachian highland based on crater counts [Tanaka et al., 2014]. These ridges (i.e. OP1, OP2, and OP3) are located near large impact craters without any apparent alteration, suggesting that they originated prior or during a similar period to the impacts.

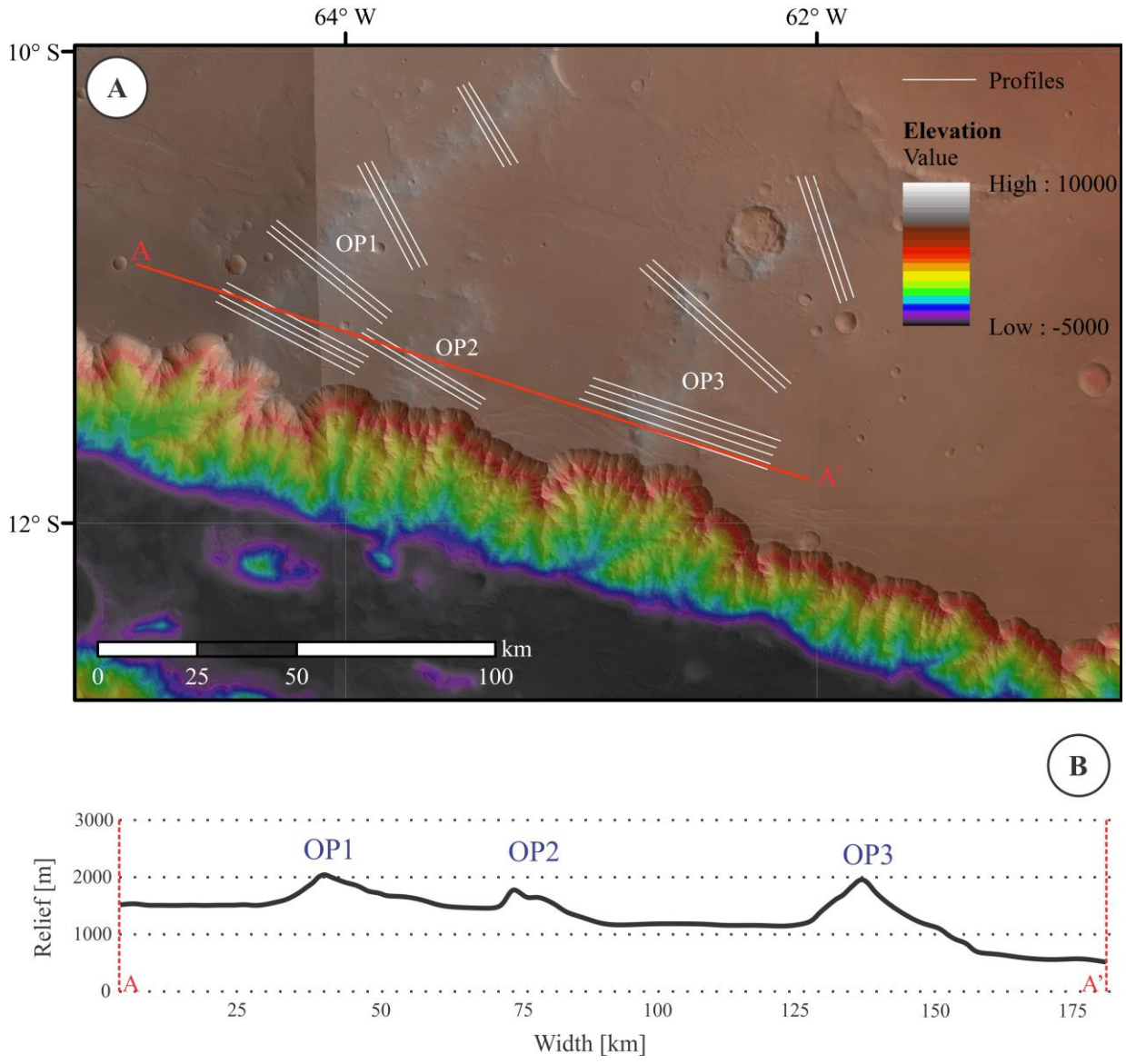

Figure 2-11 (A) Colorized elevation showing the three ridge formations OP, OP2, and OP3.Topographic profile A-A' across the three formations (red), and individual profiles (white) (B) Profile A-A'. 10x V.E.

OP1 extends along a length of ~150 km having a general form classified as quasilinear; OP2 and OP3 are shorter with lengths of ~30 km and ~120 km, respectively (Figure 2-11A). The extension of OP3 appears curved, ending abruptly near a large impact crater at its northern end. Although the fault associated with OP3 might continue under the crater, its visible length will be considered to go from the north wall of Coprates towards the northeast to the crater (Figure 2-11A).

2.5.2. Morphology of the OP ridges

The topographic relief of OP1, OP2, and OP3 is approximately 400 m, 350 m, and 800 m, respectively, above the surrounding plateau classifying them among the highest topographic features within the plateaus that surround Valles Marineris (Figure 2-11B). Comparison of these ridge formations with measured wrinkle ridges in Section 2.4 shows similar morphology, suggesting that these ridge formations are also wrinkle ridges (Figure 2-12). Their relief extends over an average broad width of 30-35 km marked by an asymmetric topography that lack the superimposed narrow ridge, which as discussed above is a key element to identify wrinkle ridges (Figure 2-12). Other events, like the deposition of volcanic material during the late Hesperian [Carr and Head, 2009], might have also altered the morphology of these formations. Because of their resemblance to wrinkle ridges and large scale in comparison to measured wrinkle ridges, they are considered to be Large Wrinkle Ridges (LWRs) with dimensions that go from 300-900 m in relief, 30-35 km in width, and 30-150 km in length (Figure 2-12). The identification of these LWRs led to a closer analysis of the region in order to determine the possible origin of their formation.

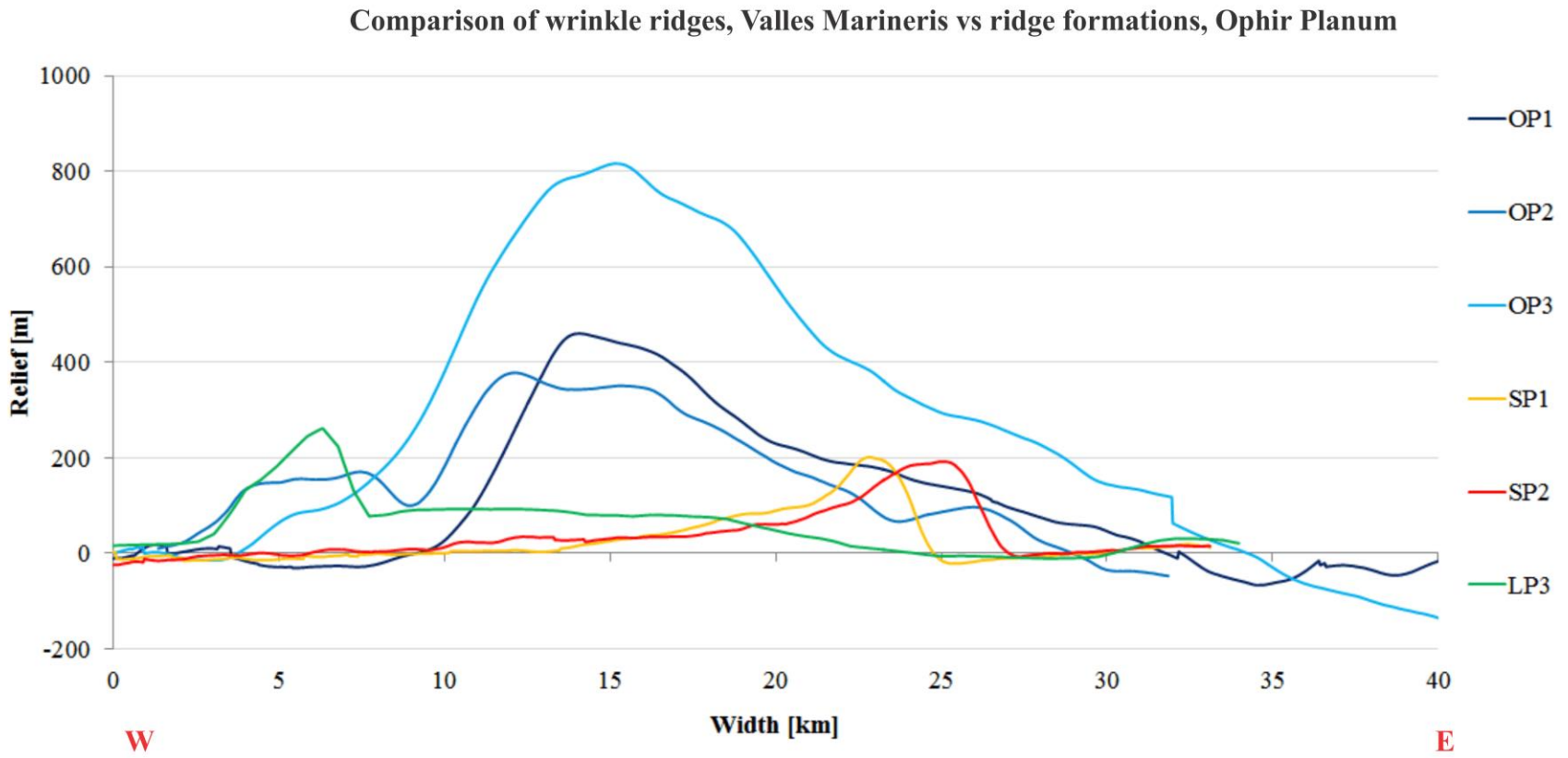

Figure 2-12: Comparison of the cross section morphology of wrinkle ridges that surround Valles Marineris with the ridge formations (OP1, OP2, and OP3) on Ophir Planum. 33x V.E. The profiles are compared to see the difference in scale between the OP ridges and the wrinkle ridges.

2.5.3. The walls of Coprates Chasma

The extension of the LWRs appears interrupted by the north wall of Coprates Chasma within the southwest region of Ophir Planum (Figure 2-13). This observation led to further inspection of the north walls of Coprates Chasma in order to identify any possible connection between the LWRs and the morphology of the walls.

The walls of Coprates Chasma consist primarily of the spur and gully wall morphology [Lucchitta, 1978]. The SG wall morphology formed as the result of extensional and erosional processes that left a series of ridges extending downslope on the surface of the wall. During the extension of the chasma, multiple faulting occurred dissecting the spur and gully morphology, resulting in the formation triangular facets approximately parallel to the wall [Peulvast et al., 2001, Fig. 7].

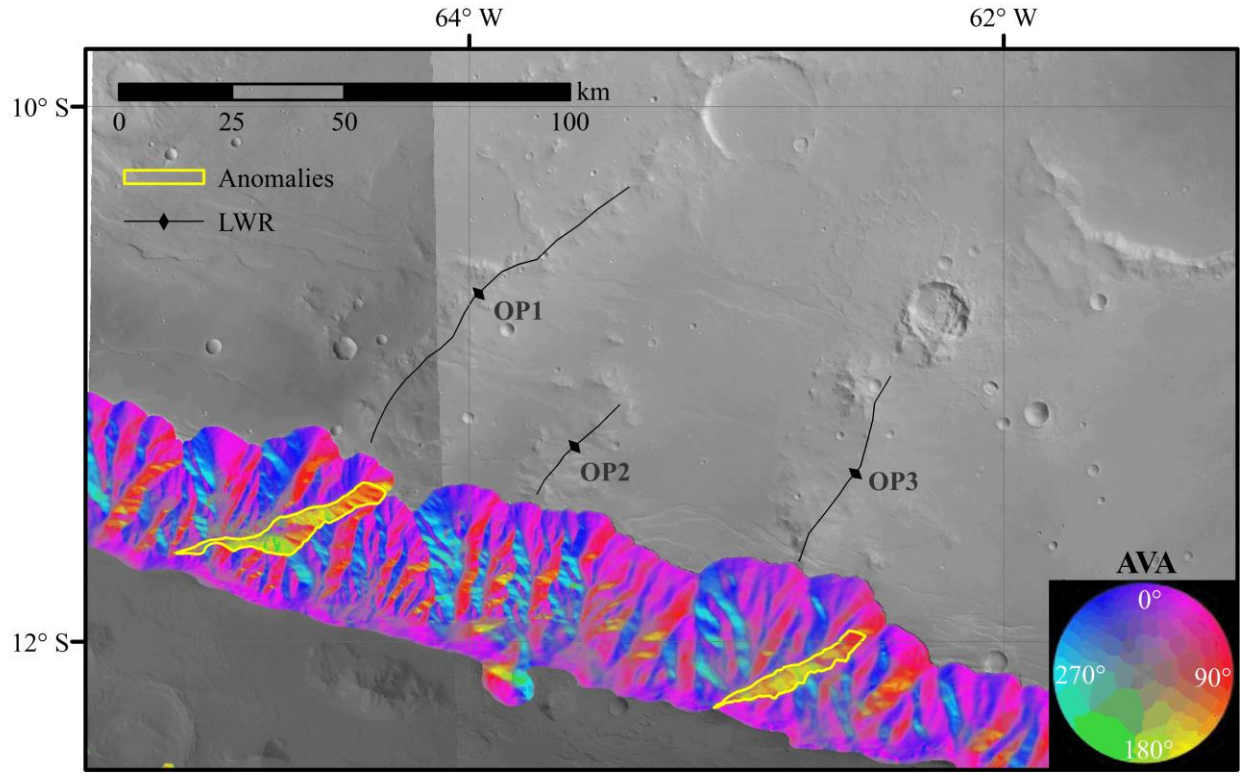

Figure 2-13: Ridge formations within Ophir Planum. The plateau is shown with HRSC imagery while walls and floor are shown with AVA color-scheme. Yellow lines highlight planar anomalies within the walls.

The topography of the SG wall morphology was analyzed using the AVA tool [Minin et al., 2015] to interpret the attitude of the walls with its color-scheme (Figure 2-13). The results show that the spurs pitch with variable angles along the walls of the chasma. The planes formed within the walls show strike values similar to the trend of the chasma, with some significant exceptions discussed below.

The trend of Coprates Chasma is ~105° a value that corresponds with the color pink for the north wall of Coprates according to the AVA color-scheme wheel. Measurements of the triangular facets have a similar color by striking 110 ± 20°. Other features as the flanks of the spur are within that strike 360 ± 20° and 180 ± 20°, appearing as blue and red, respectively. Most of these features have dips that vary from 20-30°, hence the consistent intensity of the colors.

Exceptions to the general spur and gully wall morphology appear on the AVA results as planes that have a distinctive color yellow-green. This color indicates that the planes strike 230 ± 30°, oblique to the main trend of the chasma, and dip with an angle between 20-30° into the walls of the chasm (Figure 2-13). Due the oblique attitude of the planes with respect to the walls and their anomalous dip direction, they will be referred to as Anomalous Planes (APs).

It is proposed that the APs are traces of faults visible on the walls due their oblique strike with respect of the walls, a concept similar to the observation of cross faults [Wilkins and Schultz, 2003; Andrews-Hanna, 2012a]. An alignment is observed between the LWRs and the APs (Figure 2-13) suggesting a possible relationship between them. It is inferred that the APs are the expression of the underlying faults of the LWRs exposed on the walls.

The upper section of the APs show small spurs that follow the dip direction, making the small spurs almost orthogonal to the ridge that forms the top of the APs simulating a small wall (Figure 2-14D). The intersection between the APs and the walls of the chasma appears filled with small deposits of debris resultant from the erosion along the planes (Figure 2-14D). This type of deposit is associated with relatively more recent erosional processes [Debniak et al., 2017], although this could also imply minimal erosion of the plane, just necessary to form the observed small spurs.

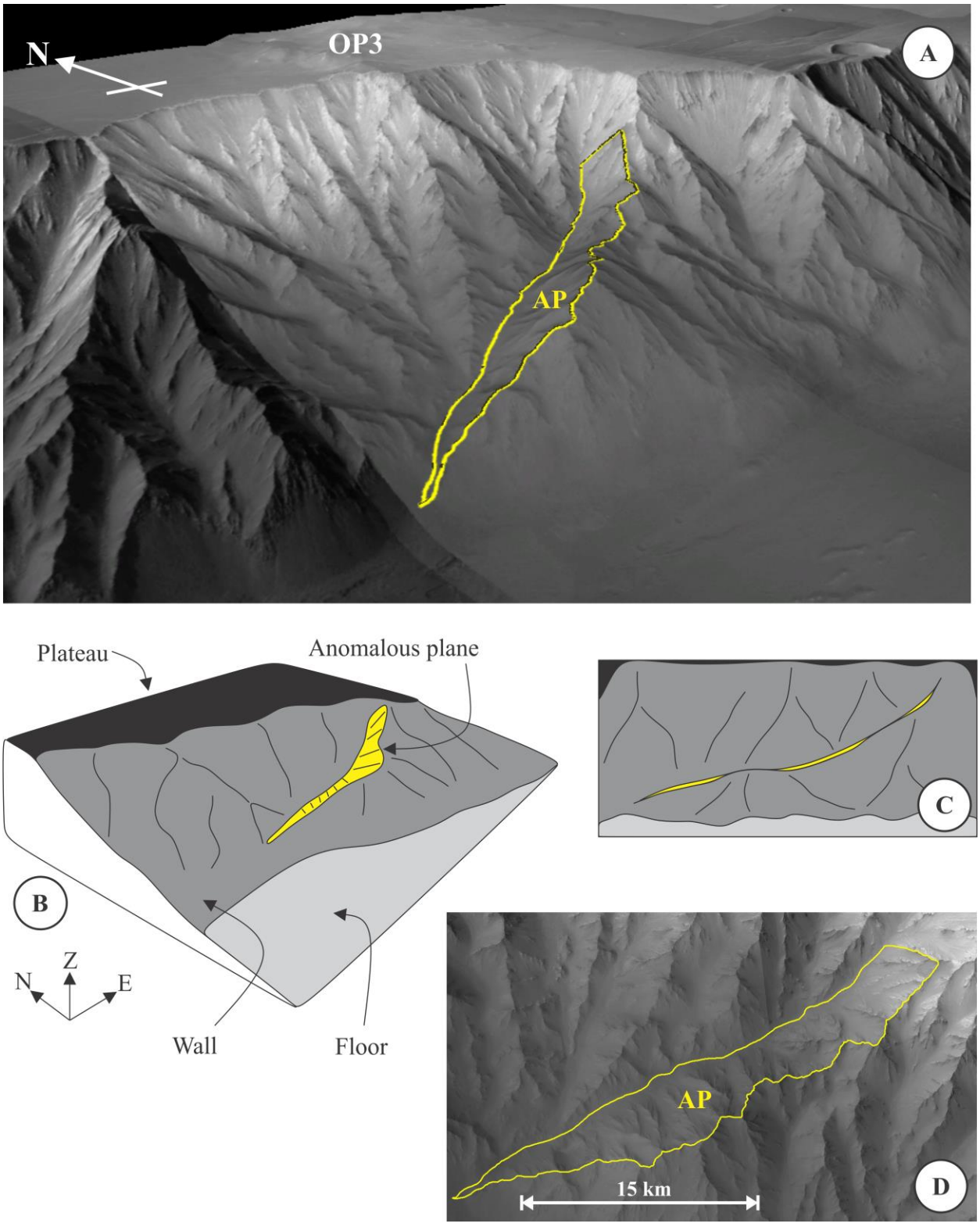

Figure 2-14: (A) 3D view of the AP subjacent to OP3. CTX imagery resolution ~5 m/px projected on MOLA-HRSC blend DEM, resolution ~200 m/px. 2x V.E. (B) scheme of the AP in color yellow with texture that indicates its dip direction towards the wall (C) schematic view of the AP suggesting it as the trace of a fault within the walls (D) close-up top view of the AP showing the orthogonal spurs.

2.5.4. Inference of structural influence

The morphology of wrinkle ridges has been proposed to be affected largely by the geometry of the underlying fault [Zuber, 1995; Okubo and Schultz, 2004; Watters, 2004], where the location and shape of the fault influences the relief and overall magnitude of the wrinkle ridge morphology. It has been suggested as well that the orientation of the fault influences the asymmetry [Okubo and Schultz, 2003, 2004; Watters, 2004]. These ideas indicate that the underlying structure of the LWRs possibly dips east based on the orientation of their asymmetry (Figure 2-11 and Figure 2-12). However, the possible connection between the LWRs and the APs subjacent to them suggest otherwise, considering the orientation of the APs (Figure 2-13 and Figure 2-14A).

It is proposed that the APs form the base of the underlying thrust-faults of the LWRs. The APs would be underlying listric faults based on their expressed geometry on the walls. This geometry indicates that the actual vergence of the underlying faults of the LWRs is towards the west (Figure 2-14A). This differs from the vergence from the asymmetric orientation of the LWRs suggests that the vergence of the underlying structures of wrinkle ridges cannot be inferred from their relief alone.

Detailed examination of the SG wall morphology subjacent to the LWRs implies that the underlying structure of the LWRs is more complex than a singular fault. The examination shows structural patterns that are possibly associated with pre-existing faults that formed the APs on the walls (Figure 2-15).

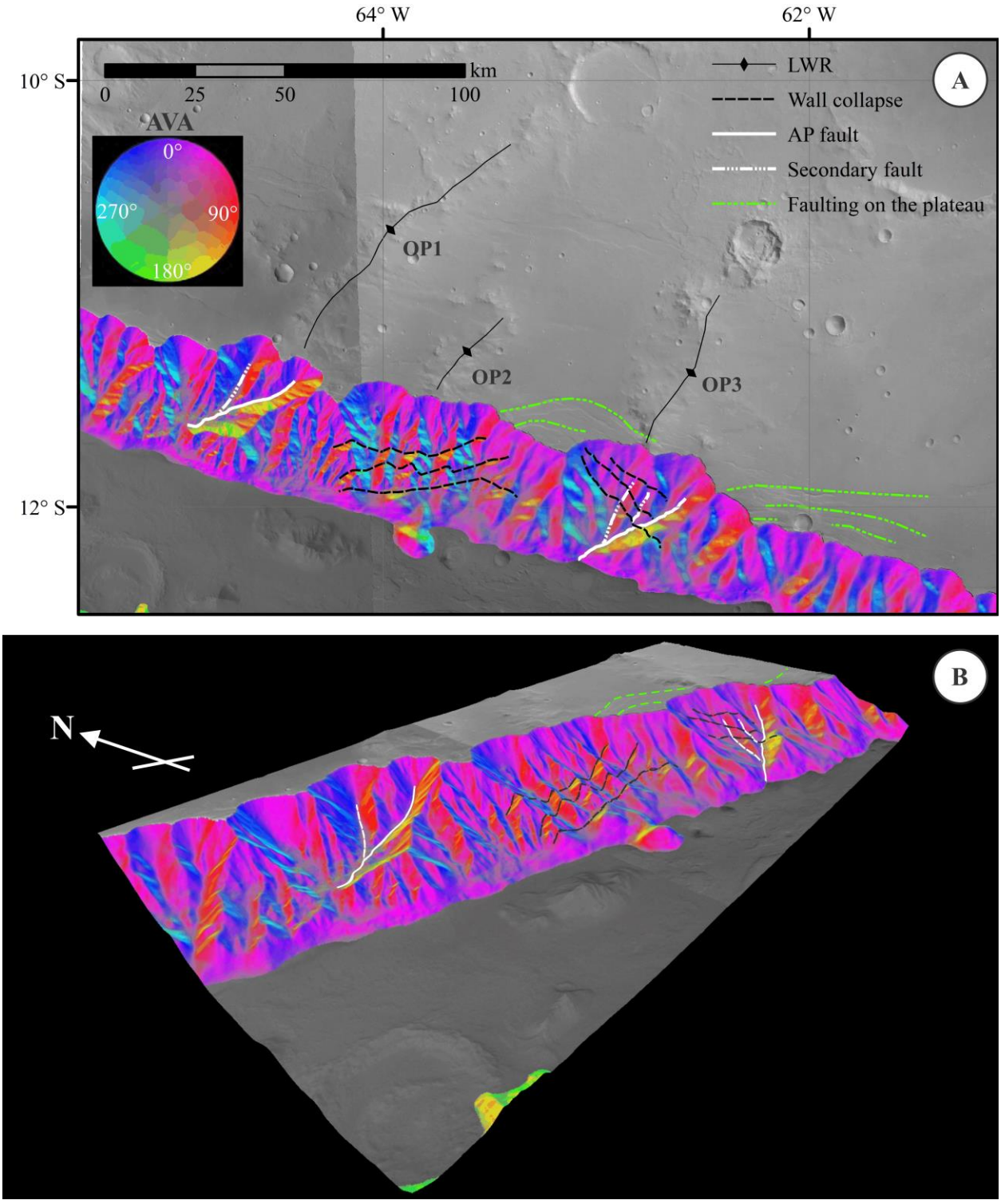

Figure 2-15: (A) Planar view and (B) 3D projection of a section of the northern wall of Coprates Chasma showing LWRs within Ophir planum and traces of the APs, possible secondary faults, and fault scarps associated with the extension of the walls and their collapse. Both figures shown using CTX imagery for the plateau and floor, and AVA results on the walls. The 3D projection uses the MOLA-HRSC blend DEM, resolution ~200 m/px. 2x V.E.

Inspection of the walls near the APs shows possible secondary fault planes that nucleate from the lower part of the APs. These secondary fault planes were identified along curved channels on the walls where it is suggested that they are located (Figure 2-15B). A secondary fault plane above the AP near OP1 appears clear as it extends on a deep channel within the wall. It is proposed that the APs and the secondary fault planes form in-sequence thrust formations for the underlying structures that formed OP1 and OP3 (Figure 2-15).

Remnants of wall collapse were identified on the walls using the AVA analysis. The collapses may have been the result of the collapse of neighbouring grabens since the traces of both features appear to align (Figure 2-15A). The traces of wall collapse align with the attitude of the grabens passing through the subjacent walls to OP2 altering the SG wall morphology in that surface. There is no visible AP observed subjacent to OP2 due the presence of the wall collapse yet it is considered that one was possibly located there based on the presence of the LWR OP2 (Figure 2-15B). The collapse extended partially over the AP aligned with OP3, slightly modifying the wall morphology in those areas in a smaller scale since the possible underlying structures are still visible (Figure 2-15A).

2.5.5. Possible origin of the APs

The large volume of the Tharsis province succumbed to the gravitational pressure of its own weight distributing the mass outwards. A schematic model of this was made showing the direction of the distribution of the load using a topographic profile parallel to the Ius-Melas-Coprates trough and nearly perpendicular to the three LWRs (Figure 2-16A).

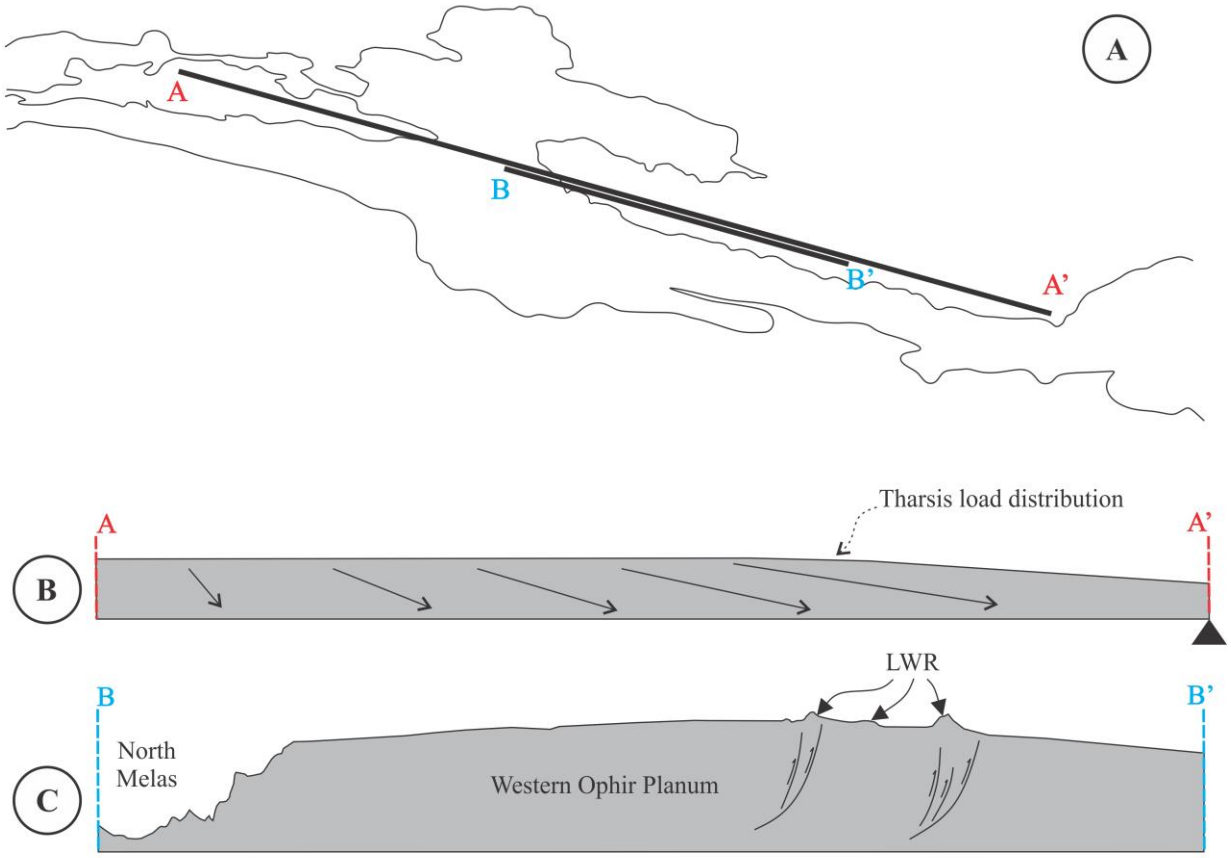

Figure 2-16: (A) Outline of the rim of the walls of central Valles Marineris (B) profile of the initial state and load distribution (C) elevation profile of the current topography of Ophir planum including the LWRs and a scheme of the possible underlying structures; All with 10x V.E.

The large mass movement led to the formation of faults within the Tharsis that might pre-date the formation of Valles Marineris. These pre-existing faults are considered to have nucleated the formation of the wrinkle ridges that surround Valles Marineris and possibly the LWRs (Figure 2-16C). The circumferential trend of the wrinkle ridges crosses the mid-section of Valles Marineris [Okubo and Schultz, 2003; Knapmeyer et al., 2006; Tanaka et al., 2014]; however, it is not possible to connect them across the chasmata (Figure 2-2).

No visible formations similar to wrinkle ridges appear within the chasmata [Witbeck et al., 1991; Okubo and Schultz, 2003; Tanaka et al., 2014], although many wrinkle ridges appear close to the rim of the outer walls of the Valles Marineris (i.e. northern and southern walls), including cases where they appear interrupted by the wall [e.g. Cole and Andrews-Hanna, 2017]. A connection between the wrinkle ridges on both sides of Valles Marineris can only be inferred in a larger perspective (Figure 2-2).

This comparison shows that the curved trend of the wrinkle ridges appears to be slightly different in attitude from the trend of the LWRs. It is possible to associate the difference in attitude to the isolated formation of the LWRs in mid Valles Marineris. The set of LWRs is notably smaller in population than the sets of wrinkle ridges that surround Valles Marineris.

The complexity of these structures (Figure 2-15) might be the result of accommodation of strain, or in the case of discontinuous deformation, the fault slip. This would occur if the LWRs coincide with the places where the total slip is much greater explaining the high relief of the LWRs. The underlying structure of the LWRs is proposed to be in-sequence blind faults suggested by the fracture patterns on the walls due possible weaker crust within that region of Valles Marineris (Figure 2-16). The combination of the in-sequence underlying structure produces a “piggyback”-type superposition of displacements, which may have caused the opposite topographic profile asymmetry of the LWR. It is proposed that complex underlying faults can lead to variations in the asymmetry of the relief by the addition of secondary faults, similar to the presence of a double arch formed by the presence of a backthrust [Okubo and Schultz, 2003].

It is proposed that the formation of the APs occurred during the extension following the Tharsis province loading. The slip of the AP-related faults and the suggested secondary faults may therefore be associated with creating the high relief of the LWRs. It is considered here that the faults are visible on the walls due to their oblique orientation with respect to the walls, which allowed them to erode the surface and create the planar expressions. This is explored with the use of elastic dislocation models to replicate the topography of the LWRs using the inferred underlying structures from the APs and the secondary faults as input for the models (Figure 2-15 and Figure 2-16).

2.6. Underlying structure of the LWRs

2.6.1. Modelling the LWRs

The model created using the USGS deformation and stress-change software (COULOMB) [Lin and Stein, 2004; Toda et al., 2005], which had previously been used for quantitative models of wrinkle ridges [Okubo and Schultz, 2004; Watters, 2004]. This software describes a 2D model that shows the outcome for the activation of the suggested system of listric faults inscribed within a homogeneous medium defined using mechanical properties such as Young's elastic modulus (E), Poisson's ratio (ν), and the friction coefficient (μ). The values used to describe the medium in which the APs are located are similar to those used in other elastic dislocation models of wrinkle ridges being E = 80 GPa, $\nu = 0.25$ and $\mu = 0.40$ [Schultz, 2000; Okubo and Schultz, 2004; Watters, 2004].

Previous studies have shown that the walls of Valles Marineris expose a lithology that varies from megaregolith, igneous rocks, and sedimentary deposition [Zuber, 1995; Ori and Karna, 2003; Williams et al, 2003; Vivianno-Beck et al., 2017]; however, such complex lithological differences cannot be considered in this model. Similarly, it is not possible to consider the presence of ice-rich volatiles within the model, since the software is limited to a homogeneous medium. This latter restriction limits the interpretation since the inclusion of ground ice has been suggested in the formation of wrinkle ridges as less competent horizons that facilitate the displacement of overlying fault blocks [Mangold et al., 1998; Okubo and Schultz, 2004; Montgomery et al., 2008]. However, the available parameters can be managed in order to make a representation of the effect of the ground ice.

In the computational model, the faults are represented by dislocations of the medium emplaced in a space with the same dimensions of the actual topography. The geometry of the faults is the result of measurements of the structural geometry from planar views. The planar sections are orthogonal to the trend of the LWRs allowing the measurement of the geometries of the faults on the walls subjacent to OP1 and OP3. Since OP1 and OP3 are the only LWRs with visible APs, they were the only ones being modeled (Figure 2-17). For the purposes of the software, the faults were divided into a series of planar segments in order to simulate the listric geometries inferred from the geometries on the walls (Figure 2-17). The attitude of each segment is the trend of their corresponding LWR and their respective dip. The faults are modeled as continuous segments forming the in-sequence listric geometries, avoiding crossing with each other.

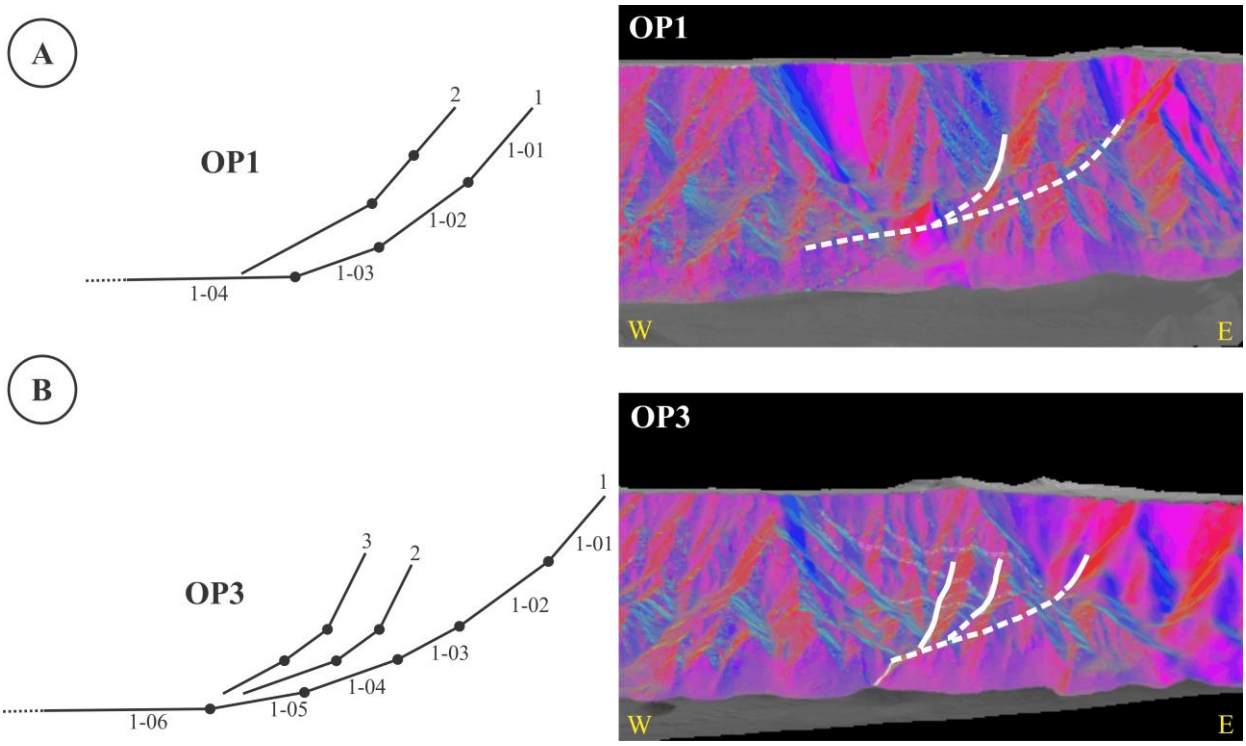

Figure 2-17: Geometrical scheme of the inferred faults used to model the LWRs (A) OP1 and (B) OP3. The label of each fault segment gives their respective LWR, fault number, and segment number. Both 2x V.E.

The variables describing each planar segment are length (L) of the fault segment, dip angle (θ) of each segment, and the depth (T) of the top end of the fault segment (Figure 2-3). Each segment of fault is considered for purpose of the software as a *receiver fault*. A receiver fault is a dislocation or fault plane defined within the medium to locate where the displacement or slip will have effect. The properties associated with the receiver faults are the dimension of the fault, the attitude of the fault, and the location of the fault. The slip or displacement (D) assigned to each fault or segment of fault is considered as a *source fault* since that is the one that defines the amount of deformation involved.

All these parameters are necessary to create the elastic dislocation model that simulates the formation of the LWRs (Table 2-1and Table 2-2), as required by the software. The values used to define the receiver faults are the result of measurements of the APs and the secondary faults projected onto the planar section/2D cross section (Figure 2-17). The source faults are defined comparable to values of displacements used in previous studies [Watters, 2004] considering that the faults nucleate on a less competent horizon.

Table 2-1: Best fitted model parameters for the OP1 underlying structure: length (L) of the fault segment, dip angle (θ) of each segment, and the depth (T), and slip or displacement (D).

Segment number	L (km)	θ (°)	T (km)	D (m)
OP1-1-01	4.6	30	0.30	10
OP1-1-02	5.8	20	2.60	500
OP1-1-03	5.2	10	4.60	700
OP1-1-04	26.7	0.5	5.50	700
OP1-1-05	13.4	0.5	5.73	600
OP1-1-06	13.4	0.5	5.85	500
OP1-1-07	8.9	0.5	5.97	300
OP1-1-08	8.9	0.5	6.04	100
OP1-1-09	8.9	0.5	6.12	10
OP1-2-01	2.9	30	0.30	10
OP1-2-02	2.9	30	1.73	500
OP1-2-03	8.3	15	3.15	700

Table 2-2: Best fitted model parameters for the OP3 underlying structure: length (L) of the fault segment, dip angle (θ) of each segment, and the depth (T), and slip or displacement (D).

Segment number	L (km)	θ (°)	T (km)	D (m)
OP3-1-01	4.0	30	0.30	10
OP3-1-02	5.8	20	2.30	500
OP3-1-03	3.9	15	4.30	700
OP3-1-04	5.8	10	5.30	700
OP3-1-05	5.7	5	6.30	700
OP3-1-06	12.7	0.3	6.80	700
OP3-1-07	4.2	0.3	6.87	600
OP3-1-08	4.2	0.3	6.89	500
OP3-1-09	4.2	0.3	6.91	300
OP3-1-10	6.4	0.3	6.93	100
OP3-1-11	6.4	0.3	6.97	10
OP3-2-01	2.8	45	2.30	500
OP3-2-02	2.9	20	4.30	500
OP3-2-03	5.8	10	5.30	700
OP3-3-01	3.3	45	2.00	500
OP3-3-02	2.9	20	4.30	500
OP3-3-03	3.9	15	5.30	700

These values of displacement are defined according to the location of the segment of the faults. Lower segments are considered to have highest displacements to compensate the unavailable ice-rich volatiles contact that facilitates the slip. Segments of faults located in the midsection of the wall are considered to be in the volcanic material that composes the Tharsis lithology assigning them smaller displacements in comparison to the lower segments (Table 2-1and Table 2-2). The segments located at the ends of the main faults have gradually decreasing displacement towards the end to simulate boundary conditions that are more realistic (Table 2-1and Table 2-2). The COULOMB software takes the given information of the medium, the receiver faults, and the source faults to simulate the deformation created by the displacement of the faults. The software shows the effect that occurs on the medium at a specific elevation or enables cross sections to view the effect of the run. Here cross sections or topographic profiles are used to compare the results of the model with the existing topography taken from DEMs.

2.6.2. Results

The underlying structures of the LWRs OP1 and OP3 were modelled together as a singular event that deformed the medium superposing the displacement of each fault segment. Several trials and combinations were performed varying the displacement values within the ranges fulfilling the defined conditions of displacement-location. The trials showed that the formation of these two LWRs can be modelled as a single event. This was made for convenience to compare the outcome of the two modelled LWRs simultaneously. The trials as well the values are presented in Table 2-1and Table 2-2.

The models are set up to show the deformation at an elevation of 0 km to observe the deformation at a surface level that would be comparable to the observed morphology from the DEMs. A contour map of the vertical displacement shows that the high relief of the LWRs was replicated (Figure 2-18).

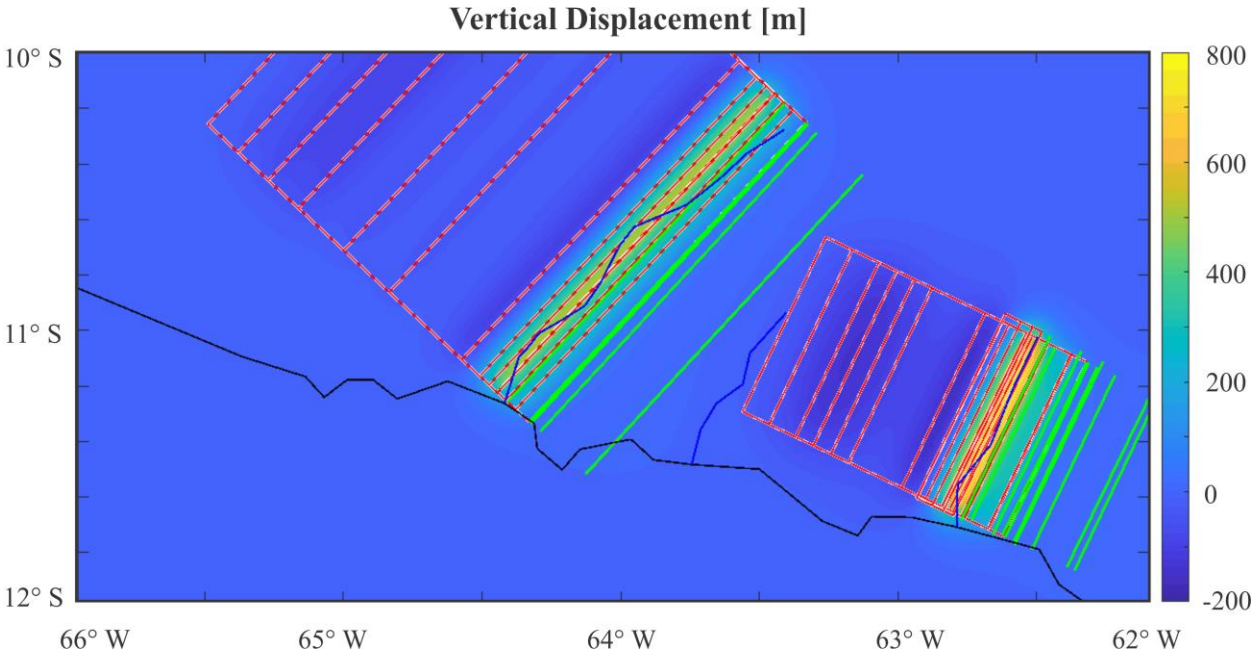

Figure 2-18: Contour map of the vertical displacement at the surface of the model (i.e. 0 km height) for the LWRs OP1 and OP3.

Cross-sections allow for the inspection of the asymmetry of the relief of the model and the location of the underlying structures relative to the topographic expression (Figure 2-19). This facilitated the comparison between the geometry of the model (Figure 2-19) and geometry of the projected imagery used to make the model (Figure 2-17 and Figure 2-20). Both the geometry of the model and the geometry of the projected imagery show similarities between the asymmetry of the LWRs and the alignment of the inferred faults from the walls and the topography of the LWRs on both the model and the DEMs. This indicates that the geometrical measurements obtained from the APs and the secondary faults used to make the models adequately represent the suggested underlying structures.

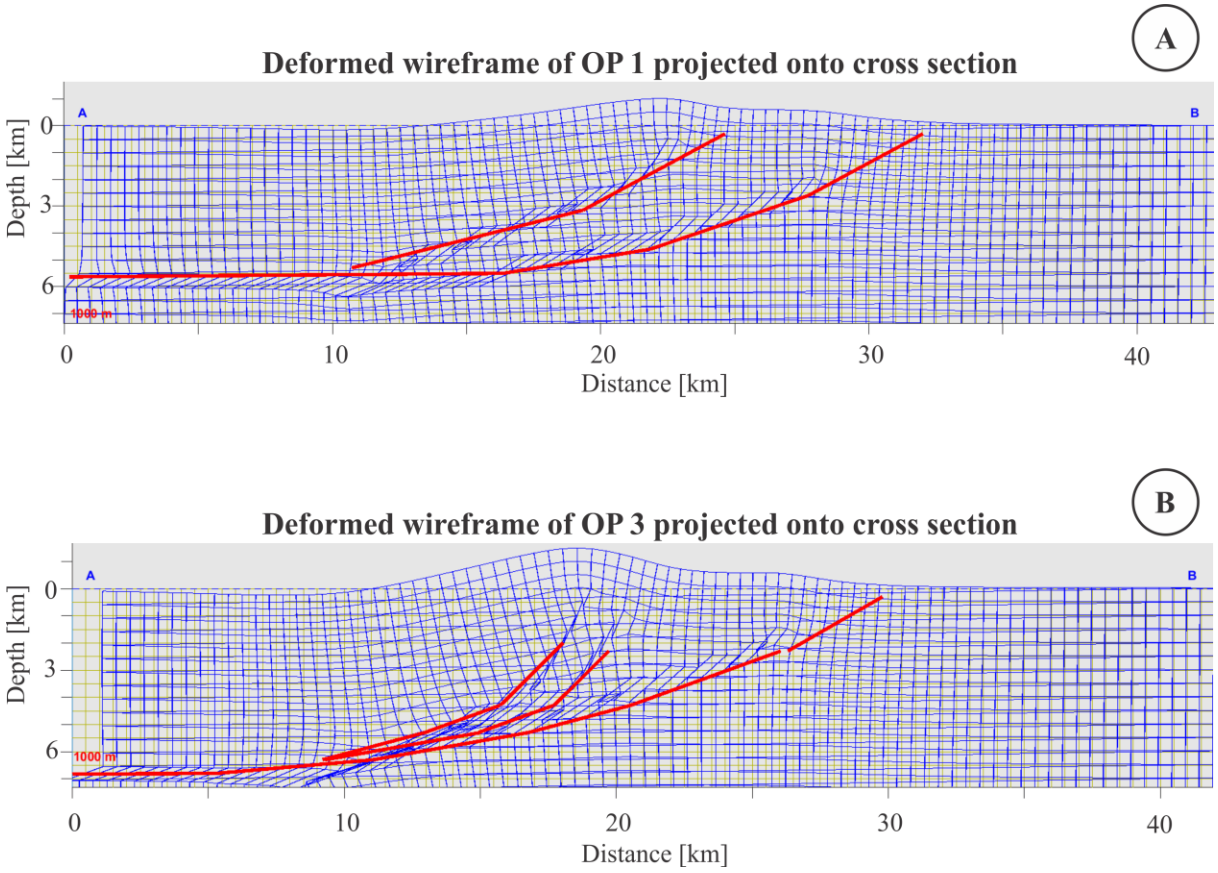

Figure 2-19: Cross-sections of the deformed grid of the medium (blue lines) 10x V.E. created by the LWRs (A) OP1 and (B) OP3 showing the underlying structures (red lines) 1x V.E.

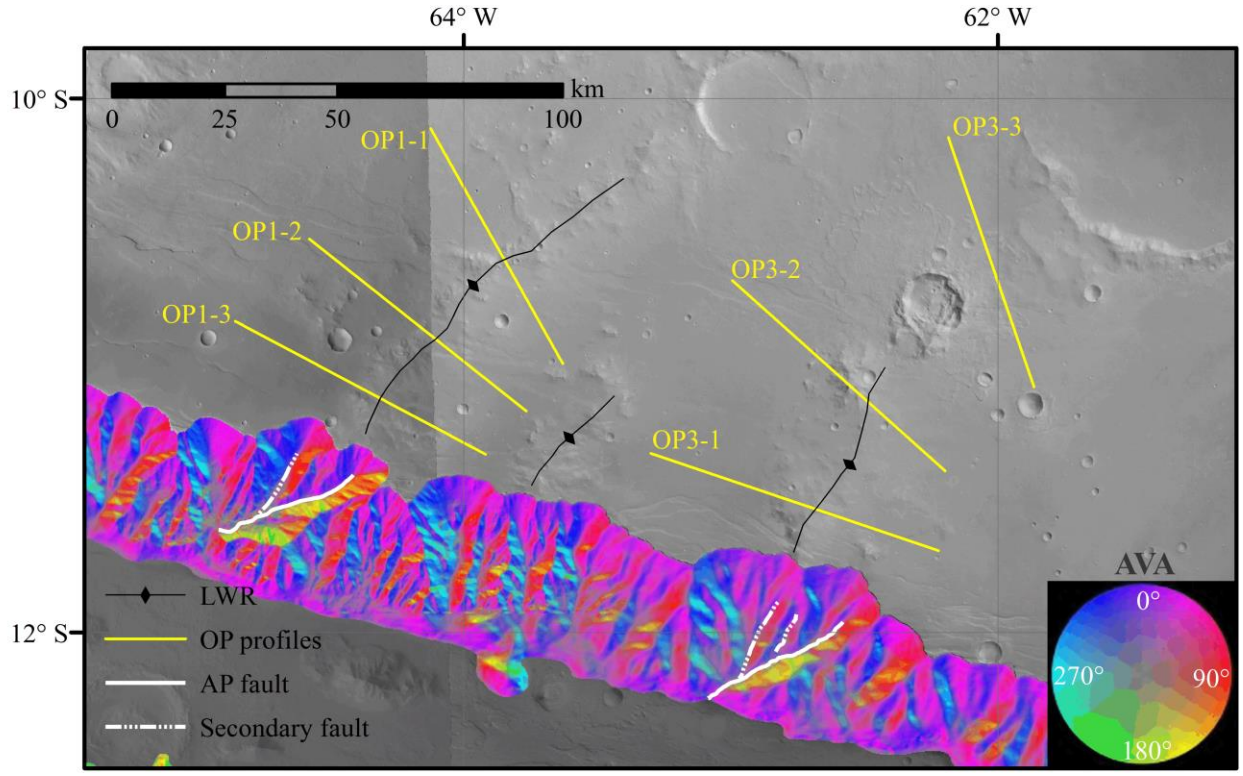

Figure 2-20: Inferred faults within the walls and selected topographic profiles of the LWRs OP1 and OP3.

Comparisons of the cross-sections of the LWRs on the models (Figure 2-19) with three profiles made covering the most representative parts of the extent of the LWRs OP1 and OP3 (Figure 2-20) show a high resemblance among the profiles with slight variations (Figure 2-21).

These results show a congruent outcome corroborating the replication of the relief and the asymmetry of the modelled LWRs (Figure 2-21). The connection between the LWRs and the APs appears validated by the fit between the topography of the model and the topography of the DEMs indicating that the observed geometries on the walls represent the possible underlying structure of the LWRs. The fit also suggests that the used displacement values are approximate to the possible displacements involved in the formation of the relief of the LWRs.

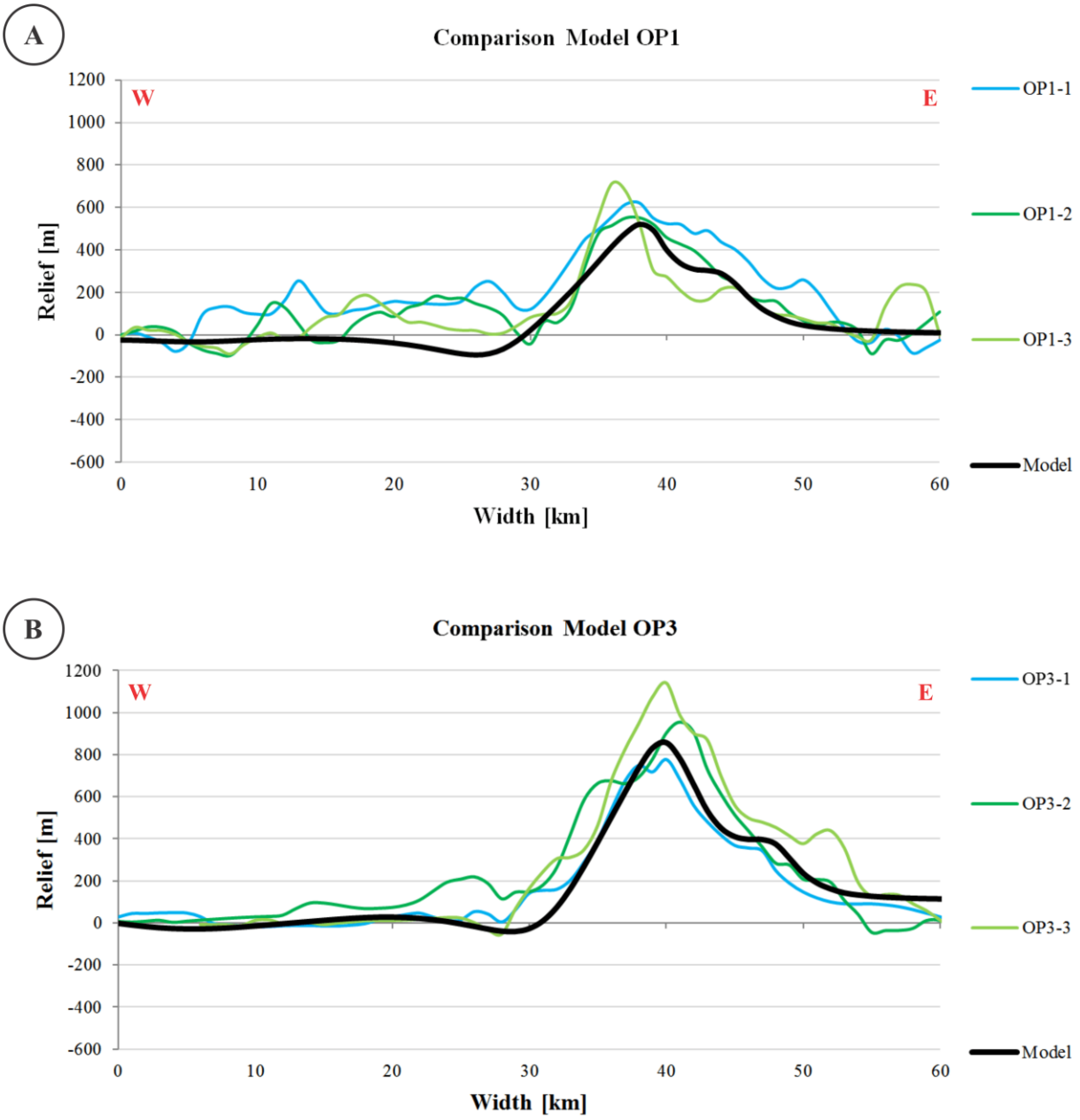

Figure 2-21: (A, B) Comparison of topographic profiles over the LWR OP1 (A) and OP3 (B), and the resultant topography from the model. 33x V.E.

The slight variations between the topography of the model and the observed topography can be attributed to later deposits and erosional process that might have altered the relief. Since the model only analyzes the formation of the wrinkle ridges based on the underlying structure, not taking into account other processes. Processes such as deposition, erosion, or even secondary

tectonism are not included in the results. Nevertheless, the replication of the asymmetry and the morphology of the LWRs validate the results of the model. The agreement between both morphologies (Figure 2-21) suggests that the geometries described in Table 2-1and Table 2-2 adequately represent the actual underlying structures of the LWRs.

2.7. Discussion

Comparisons of wrinkle ridges within several plateaus that surround Valles Marineris reveal morphological similarities, suggesting similar underlying mechanics. The formation of the relief of wrinkle ridges is associated with the geometry and location of the underlying structures. It is proposed that wrinkle ridges with complex fault systems could explain the variety of forms observed in cross sections of wrinkle ridges. The results show that the orientation of the underlying fault of wrinkle ridges can be inferred from the asymmetric relief only for wrinkle ridges formed by singular underlying faults. This was proven with the large wrinkle ridges since their asymmetry does not match the vergence of a simple listric fault system.

The model of the large wrinkle ridges shows agreement between the modeled topography and the actual topography of the formations (Figure 2-21). This demonstrates that their underlying structures are complex and appear expressed on the walls of Coprates as the anomalous planes and the secondary faults. It was shown that the anomalous planes likely represent the underlying structures of the large wrinkle ridges based on the comparable results of the model topographic profiles.

These results show that features within the walls may represent structural influence from pre-existing faults within the Tharsis in the formation of the spur and gully wall morphology. The unique form of the large wrinkle ridges indicates that complex structures can be associated with the formation of wrinkle ridges.

The isolated formation of these large wrinkle ridges may be the result of accumulated amounts of strain, based on their high relief. This is compared to other sets of wrinkle ridges that have lower relief and a higher number wrinkle ridges within the set or region (Figure 2-12). It is possible that complex structures can result from the accumulation of strain suggesting a relationship between the distribution of wrinkle ridges and the scale of their morphology.

2.8. Conclusion

This chapter shows a new perspective in the analysis of the formation of wrinkle ridges by using the walls of Valles Marineris. It was demonstrated that it is not possible to infer the vergence of the faults associated with wrinkle ridges, as it is possible that they have complex underlying structures. The formation and expression of wrinkle ridges can be associated not only with the complexity of the structures but also with the lithology of the region. The large wrinkle ridges are an isolated case where the underlying structure of a feature can be traced along the walls of a chasma. The presence of anomalous planes within the walls of Valles Marineris indicates that the formation of the walls involved more than erosional processes.

The use of elastic dislocation models is a tool that facilitated the analysis of deformation of underlying structures. Nevertheless, it must be considered that its use depends on the complexity of the region and the system. The limitations of the software must be considered in order to properly replicate the event.

Chapter 3 : Structural development of spurs and gullies

3.1. Introduction

In the last chapter, a special case of Spur and Gully (SG) wall morphology was discussed, showing the influence of pre-exiting structures on the wall morphology of Valles Marineris. Here I explore a more detailed analysis of the development of SGs.

3.1.1. SGs and Valles Marineris

Spurs are a series of ridges formed usually trending downslope on inclined surfaces. They cover large areas of the walls of Valles Marineris (Figure 3-1) [Lucchitta, 1978; Witbeck et al., 1991; Peulvast et al., 2001]. On Valles Marineris they have been classified as the most common wall morphology on the region, having formed during the late Hesperian [Lucchitta, 1978; Carr and Head, 2009]. Spurs are one of the morphologies that expose the interior of the Tharsis province [Golombek and Phillips, 2010]. On Earth is has been established that ridges and troughs form by slow erosional processes [Blackwelder, 1928]. These ridges and troughs are comparable to the SG wall morphology which is composed of ridges and troughs formed along slope of the walls [Lucchitta, 1978; Patton, 1990]. On Valles Marineris, their formation occurred during and following the formation of the chasmata, in the absence of catastrophic events such as landslides [Lucchitta, 1978; Wallace, 1978, Patton, 1990]. The formation of SGs depends on the location of the Tharsis bedrock [Lucchitta, 1978], an intrusive and extrusive magmatic deposit [Anderson et al., 2001], obscured on the walls due to events such as faulting that displaced sections of the walls during the retreat [Peulvast et al., 2001; Williams et al., 2003]. Nonetheless, the bedrock can be observed on certain areas within the walls [Ori and Karna, 2003; Williams et al., 2003; Viviano-Beck et al., 2017].

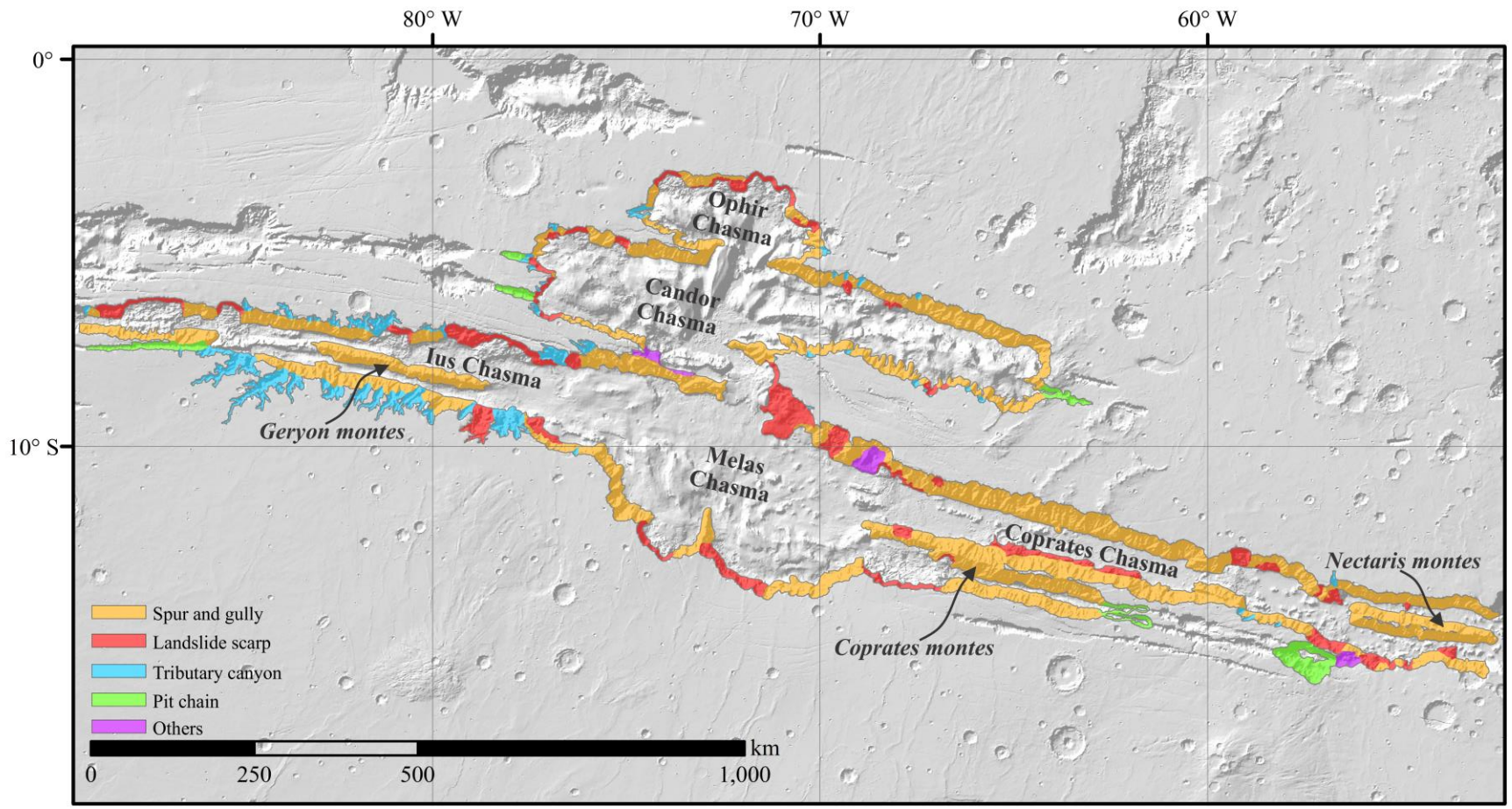

Figure 3-1: Mapped wall morphology of central Valles Marineris and other associated morphologies shown over Mars Orbiter Laser Altimetry (MOLA) Hillshade imagery.

Other wall morphologies such as tributary canyons and landslide scarps formed by different processes show small SGs within some of their surfaces. Landslides are considered to have occurred mostly during the Amazonian period although many appear to have occurred during the late Hesperian [Carr and Head, 2009]. They collapse over a range of elevations on smaller regions of the walls concentrating mostly in mid Valles Marineris (Figure 3-1) [Lucchitta, 1978, 1979; Peulvast et al., 2001]. SGs are noticed on landslide scarps, possibly reappearing over pre-existent structures that facilitated preferential erosion [Lucchitta, 1978] (Figure 3-2).

Both SG and landslide scarp morphologies are located on the flanks of montes in Valles Marineris (Figure 3-1). These montes are possible remnants of horsts formed simultaneously with Valles Marineris [Schultz, 1991, 2000; Mege and Bourgeois, 2011]. The SGs on Geryon Montes (Ius Chasma) and Nectaris Montes (Coprates Chasma) are similar although those on Geryon Montes are smaller and have lower elevation [Tanaka et al., 2014: Debniak et al., 2017].

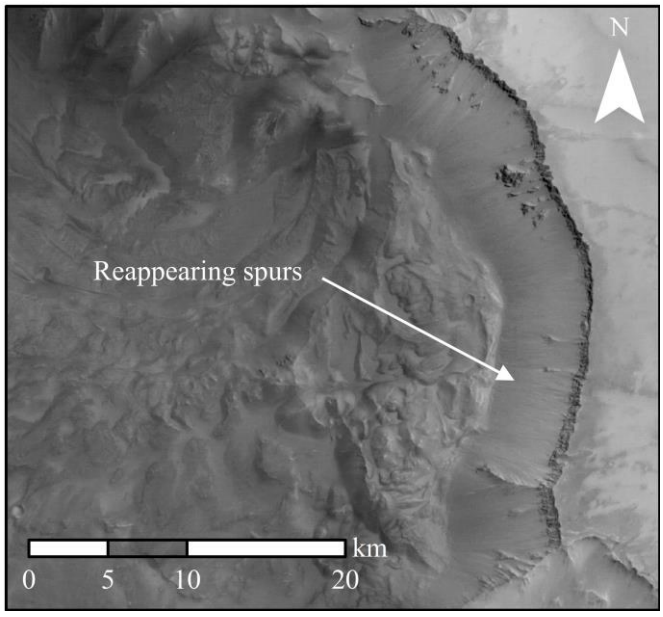

Figure 3-2: Example of reappearing spurs on the north walls of Melas Chasma near western Coprates Chasma shown using High Resolution Stereoscopic Camera (HRSC) Imagery.

3.1.2. Slope stability

The slope of planetary surfaces varies depending on gravitational and environmental conditions [Schultz, 2002; Kleinhans et al., 2011]. It has been suggested that the scale of slope dimensions (i.e. height and angle) is inversely proportional to the gravity of the planet [Caruso, 2002; Schultz, 2002] implying that the larger wallslopes on Mars are stable compared to Earth's [Schultz, 2002]. Schultz [2002] suggested that the stability of the slopes can be determined by using the slope or the height alone yet both height and angle must be considered in the analysis.

Schultz [2002] indicated that the layered wallrock of Valles Marineris has eroded into slopes of 10-30° in walls with SG wall morphology that have a height of 1-8 km. The large scale of the walls of Valles Marineris could explain the low dip of the Martian walls compared to the repose angle of Earth's deserts of 30-35° [Atwood-Stone and McEwen, 2013]. Factors such as a desert-like granular surface for the walls of Valles Marineris and the Martian low-gravity are involved in the stability of slopes [Schultz, 2002] indicate that the expected angles of repose are lower dynamic angles and higher static angles in lower gravities [Kleinhans et al., 2011].

3.1.3. Structural influence

It has been suggested that the walls of Valles Marineris initiated their formation during late Noachian through the late Hesperian, involving processes such as faulting, subsidence, and collapse [Carr and Head, 2009; Andrews-Hanna, 2012; Tanaka et al., 2014]. The extensional processes and flexural subsidence involved in the formation of Valles Marineris [Andrews-Hanna, 2012] implies the occurrence of wall retreat that altered the general shape of SGs [Peulvast et al., 2001].

Studies have suggested that faulting could have structurally influenced the morphology of the walls [Blasius et al., 1977; Lucchitta, 1978; Peulvast et al., 2001; Cole and Andrews-Hanna, 2017] where secondary scarps known as triangular facets formed within the SG wall morphology (Figure 3-3A) [Peulvast et al., 2001].

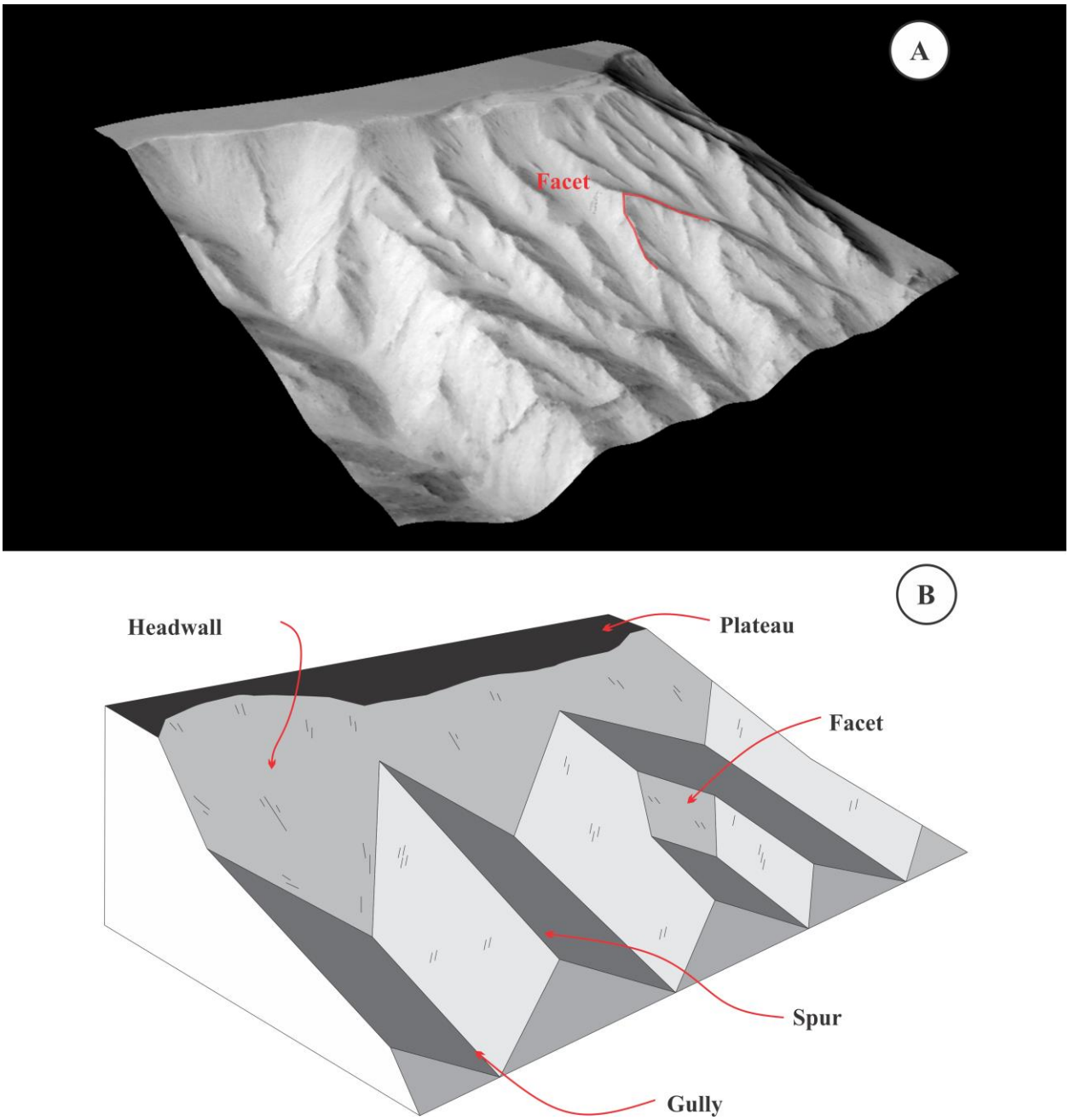

Figure 3-3: (A) 3D projection of tectonic control expressed by facet on the northern walls of Ophir Chasma (3°07'S, 72°54'W) (B) simplified SG morphology. All with 1x Vertical Exaggeration (V.E.).

Triangular facets form as fault planes cut and offset ridges; they reshaped the spurs reducing the crests. Their planar morphology is inherited from their bounded fault [Wallace, 1978; Peulvast et al., 2001].

In this study, the goal is to perform a detailed inspection of the walls of Valles Marineris focusing on the SG wall morphology and the nature of the origin of the spurs. This continues with observations introduced in Chapter 2, where a connection between the SG wall morphology and pre-exiting fault within the Tharsis was made. The connection proposes that structural influence from pre-existing faults is visible on the walls as anomalies and/or other characteristic morphologies. Detailed analyses made for the spurs and the SG wall morphology as a whole show several cases in further sections that indicate structural influence.

3.2. Preliminary work

3.2.1. Dataset selection

Spatial analysis of the Martian surface requires the use of datasets with diverse resolution depending on the subject under study. Here the study relies on datasets such as imagery and Digital Elevation Models (DEMs) of various resolutions. The DEMs vary from resolutions of ~450 m/px from interpolation of the Mars Orbiter Laser Altimetry (MOLA) tracks that cover the full extent of the Martian surface [Smith et al., 1999] to resolutions of ~50-150 m/px available from the High Resolution Stereoscopic Camera (HRSC) [Gwinner et al., 2016]. Recently a blended version of both datasets was released with resolution of ~200 m/px making the results among the chasmata comparable [Laura and Fergason, 2016; Fergason et al., 2017].

DEMs with higher resolution made from imagery of the Context Imager (CTX) have resolutions of ~18m/px. The DEMs are computed using routines from the NASA Ames Stereo Pipeline [Broxton and Edwards, 2008; Moratto et al., 2010]. These DEMs cover the overlapped

areas of the available imagery providing detailed results of the wall morphology of Valles Marineris. Further analyses will show that DEMs of different resolution provide similar results in terms of spatial distribution.

Multiple mosaic datasets made to facilitate the examination of the Martian surface cover the majority of the interior of Valles Marineris using the MOLA Hillshade, HRSC imagery, and CTX imagery with resolutions of 128 pixels per degree, ~12.5-50 m/px, and ~6m/px respectively [Smith et al., 1999; Broxton and Edwards, 2008; Gwinner et al., 2016]. They facilitate the identification and location of many formations and features on central Valles Marineris focusing in the morphology of the walls.

3.2.2. Simplified morphology

The geometry of the SG wall morphology is composed of several elements: downslope ridges or spurs, bounded down-streams or gullies, headwalls, and in some cases triangular facets (Figure 3-3A) [Blackwelder, 1928; Blasius et al., 1977; Lucchitta, 1978; Wallace, 1978; Peulvast et al 2001]. Closer analyses of the geometry of the walls require a simplification of the latter features by associating them with planes and lineations (Figure 3-3B). This allowed a simpler quantification and easier interpretation of the morphology. Features such as the trimline at the lower section of the wall is not considered as it is associated with the latest collapse and the possible presence of superficial ice making a glacial boundary [Mege and Bourgeois, 2011].

The simplified form of the morphology considers the SGs as linear features (Figure 3-3B). These linear features are the intersections of the flanks of the spurs. The flanks are planes considered as uniform surfaces (Figure 3-3B). Other planar features within the walls are the facets, which inherit their strike from the fault that originated them.

Other features within the morphology are the headwalls that are curved features on the surfaces of the walls formed by the isolated collapse or retreat of the rim. Here they are described as curved planes, almost conical, and are measured downslope along the center of the conical shape (Figure 3-3B). In general, these are considered as well-defined features whereas other features such as “recent” basal scarps (Figure 3-3A), or highly subdivided spurs are discarded in the measurements.

3.3. Analysis of the wall morphology

3.3.1. Techniques and methodologies

Analysis of the morphology and geology of the walls relies on the use of DEMs and imagery datasets. The geometry of the DEMs is analyzed using scripts within ArcGIS, some of them developed by Minin et al. [2015], which are described in detail below. The methodologies were applied over the full extent of the walls covering from the upper plateau that surrounds the chasmata to its floor. The floor is considered to be the lower horizontal surface that limits the extent of the walls; interior layered deposits and debris flows from landslides are included as part of the floor. It was noticed that the resolution of the DEMs affects the size of features that can be identified, yet this did not change the range of values obtained using these methodologies.

3.3.1.1. Dip analysis

The dip analysis calculates the slope of each pixel of a DEM using a 3x3 kernel. The kernel computes the inclination of a plane centered on a specific pixel and assigns the value to the output raster [Minin et al., 2015]. The results are grouped in ranges from 0-5°, 6-15°, 16-20°, 21-30°, 31-40°, and >41° to represent different features observed within the walls (Figure 3-4). This classification was based on the analysis of the dip values associated with observed features

within the walls and are explained in following sections. One of the uses of this methodology is the identification of "recently" eroded areas or areas that have accumulated material based on observation of a cluster of shallower dip ranges on the walls.

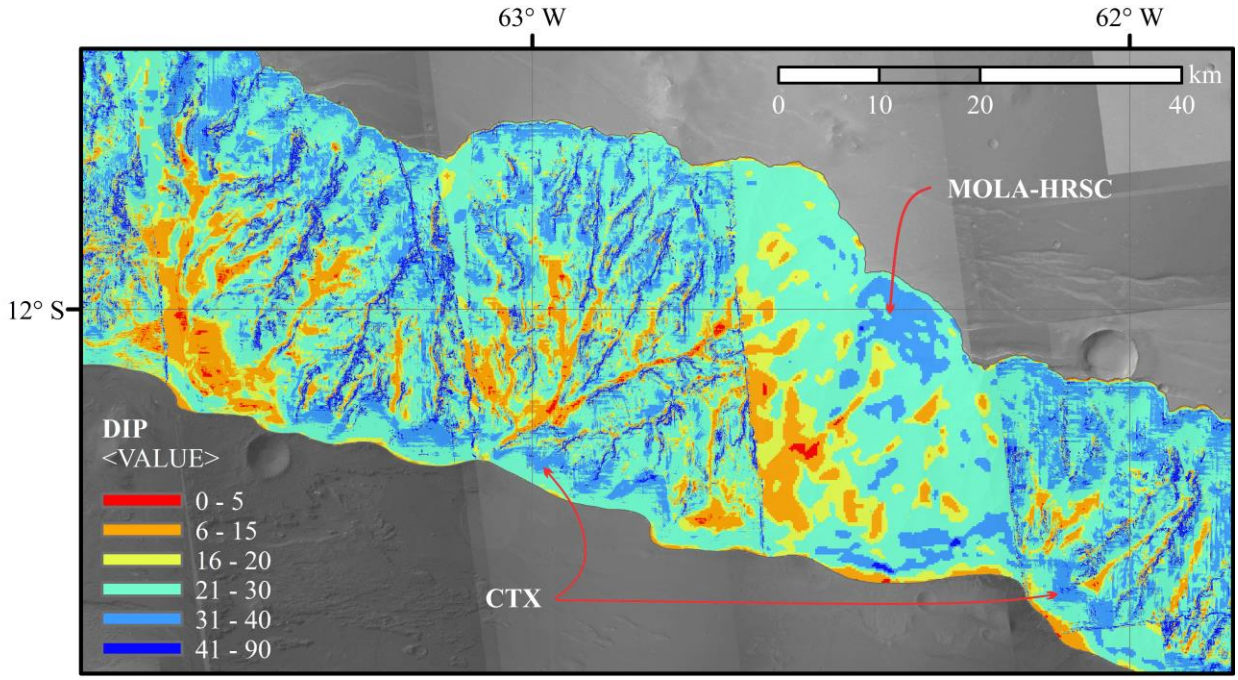

Figure 3-4: Dip analysis results of the wall morphology of the north wall of Coprates Chasma using the MOLA-HRSC blended DEM and CTX DEMs with resolutions of ~200 m/px and ~18 m/px respectively.

3.3.1.2. Mean Signed Squared Difference (MSSD)

The Least Square Regression is a method that mathematically analyzes surfaces [Davis, 2002]. Here it was used to identify planar forms on the DEMs, effectively highlighting formations such as ridges and troughs. The method has variations that cannot differentiate between convex and concave curvatures [Minin et al., 2015], which makes the distinction of ridges/spurs from troughs/gullies impossible. MSSD is a variation of the method that can differentiate convex from concave curvatures by multiplying deviations by their absolute values prior to averaging [Minin et al., 2015].

The method calculates the possible planes that fit the size of the kernel defined for the feature under study. In this case, it is associated with the ridges/spurs that are relatively large and well defined. To identify these spurs, trials varying the kernel size were made; finally, a size that covers an area of 11x11px (i.e. ~2x2 km for the used resolution) was selected to determine the distribution of competent ridges/spurs and troughs/gullies (Figure 3-5).

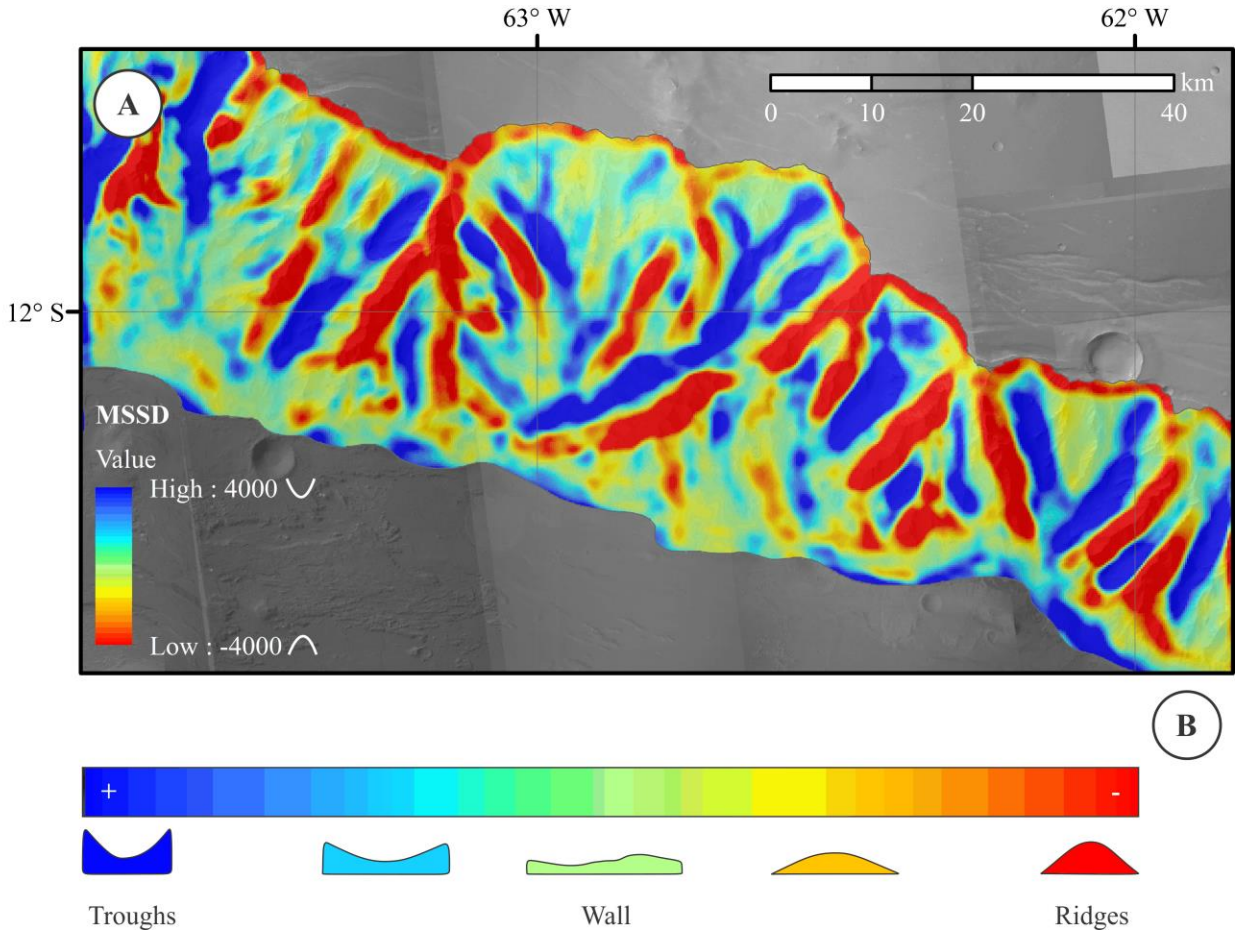

Figure 3-5: North wall of Coprates Chasma showing (A) MSSD results of the curvature of the surface and (B) MSSD color scheme range associated with the change in curvature of the relief of the features.

The results consider the maximum curvature values expected from the highly pronounced ridges and troughs being the negative and positive MSSD values respectively (Figure 3-5B). Intermediate values are associated with the transition between both features where the curvatures

are less pronounced (Figure 3-5B). Yet smaller features appear within these ranges and might not be noticed due the size of the kernel as it appears on headwalls and plane surfaces with small spurs (Figure 3-5).

3.3.1.3. Augmented Visualization of Attitudes (AVA)

In order to quantify changes on the surface of the walls, the AVA tool is used [Minin et al., 2015], which facilitates the interpretation of the features on the walls. The results are shown as a raster that shows the attitude of the surface using a color-scheme wheel [Minin et al., 2015]. The colors assigned to the northern and southern walls of Valles Marineris are pink and green, respectively (Figure 3-6). The assigned range of colors depends on the orientation of the walls and features in relationship with the color wheel [Chapter 2] (Figure 3-6). Features such as facets appear obscure or disguised since they have similar attitudes to the walls. However, this method makes recognition of features on walls an easier task due the contrast of colors.

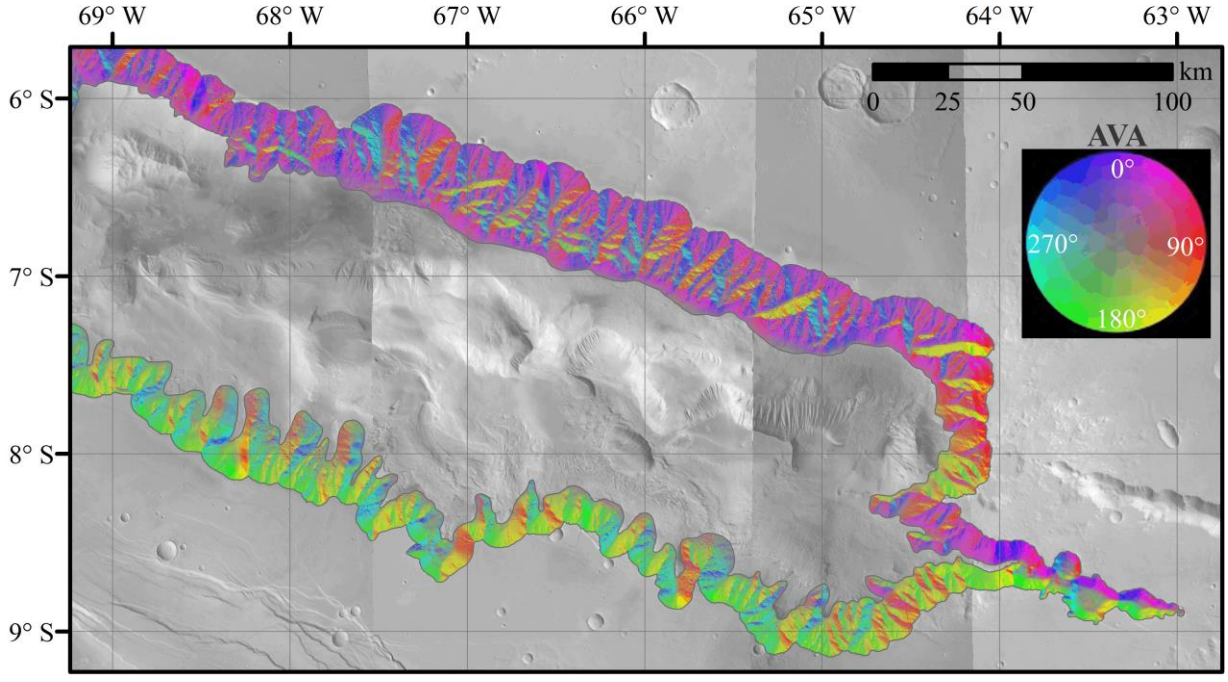

Figure 3-6: AVA results of the spur and gully wall morphology of East Candor Chasma; including the AVA color-scheme wheel.

3.3.2. Results

3.3.2.1. Dip analysis of the walls

The classification of dip ranges is the result of inspecting the distribution of dip values along the walls associating the ranges with different observed features. Ranges between 0-5° are associated with plana or plateau and shallower deposits such as debris flows from landslides (Figure 3-7A). Values between 6-15° are representative of shallow surfaces such as slumps [Schultz, 2002]. These ranges are based on observations along the walls of central Valles Marineris.

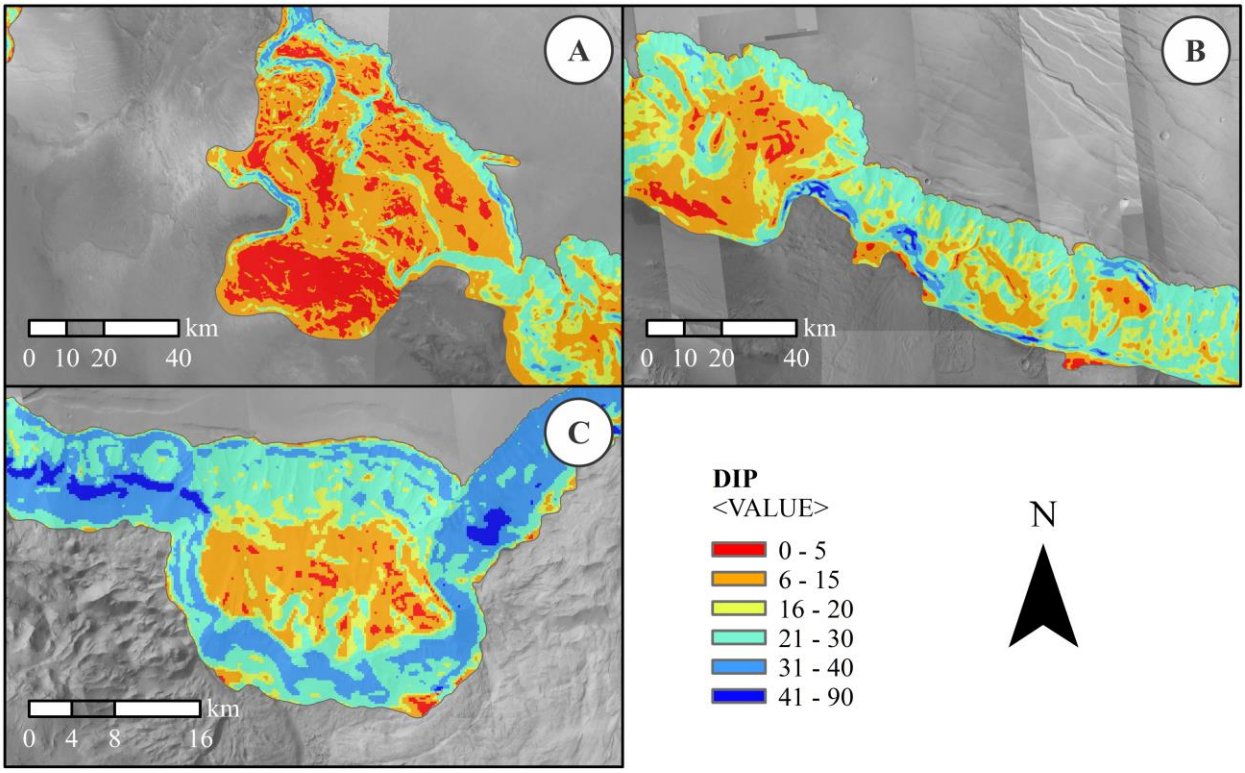

Figure 3-7: Dip results of shallow surfaces of (A) western Coprates Chasma – Melas Chasma (B) western Coprates Chasma, and (C) the north wall of Ophir Chasma.

The results indicate the possibility of "recent" mass movement based on the accumulated material. Examples of these ranges appear on Ophir Chasma and Coprates Chasma (Figure 3-7 A-C) where these surfaces have been associated with detached walls and remnant of landslides that slump along the walls [Witbeck et al., 1991].

Large concentrations of debris appear within tributary canyons such as those at Ius Chasma (Figure 3-8 A&B) where the values are associated with possible eroded material that covered or buried the area. The presence of accumulated material, similar to younger deposits, can obscure or hide fault planes exposed on the walls [Carr and Head, 2009]. Steep dip values within a range of 16-20° describe deposits on gullies or disrupted surfaces possibly indicating "recent" erosional activity on the walls based on the shallow dips associated with this range (Figure 3-8C).

Ranges between 21-30° describe the stable slope of the walls [Schultz, 2002; Kleinhans et al., 2011] dominating the extent of the walls of Valles Marineris (Figure 3-9A). The mean dip value of the walls is ~24° (Figure 3-9B), based on calculations for the dip distribution for the CTX and MOLA DEMs. Both distribution are highly similar to each other which indicates that relatively high and low resolutions can show congruent results (Figure 3-9C).

Dip values greater than 30° may represent possible inherited structural characteristics such as basal scarps and others, observed on ranges between 31-40°. The dip distribution decreases rapidly for values >35° (Figure 3-9 B&C), associating those values with "recent" collapse scarps based on the observed values in areas such as landslide scarps and the upper sections of headwalls (Figure 3-7C, Figure 3-8). Later erosional processes may have stabilized the slope leading to the shallower angle of repose whereas collapse of the walls is expressed with steeper surfaces.

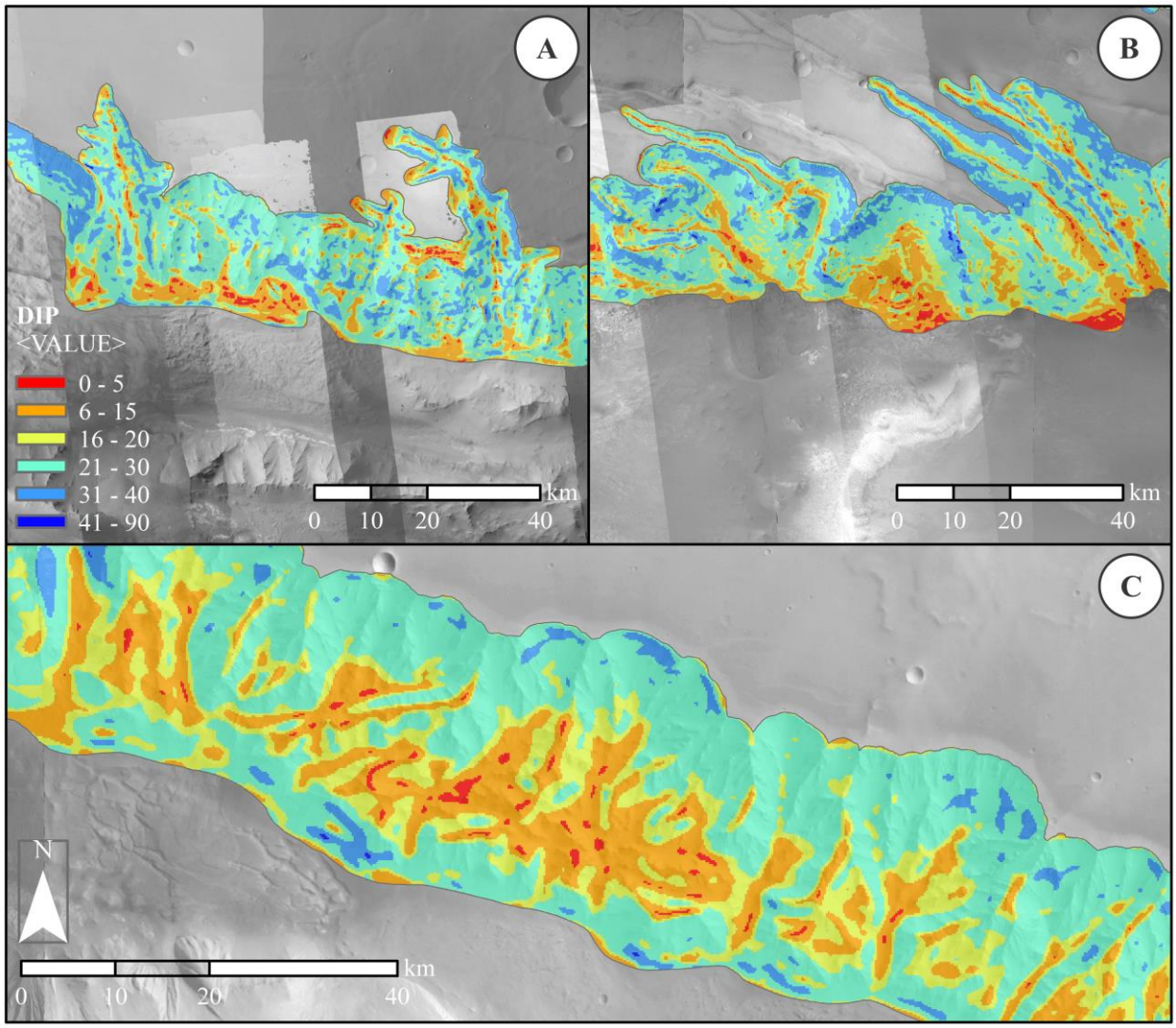

Figure 3-8: Dip results of accumulated debris and deposits within (A,B) tributary of Ius Chasma, and (C) the north wall of East Candor Chasma.

Values greater than 41° are rare associating them with the most recent collapse or faulting of the walls. They appear in areas such as the walls of Ophir Chasma (Figure 3-7C) and Melas Chasma. The southern walls of Melas Chasma walls appear to be formed by wall collapse and landslides (Figure 3-9).

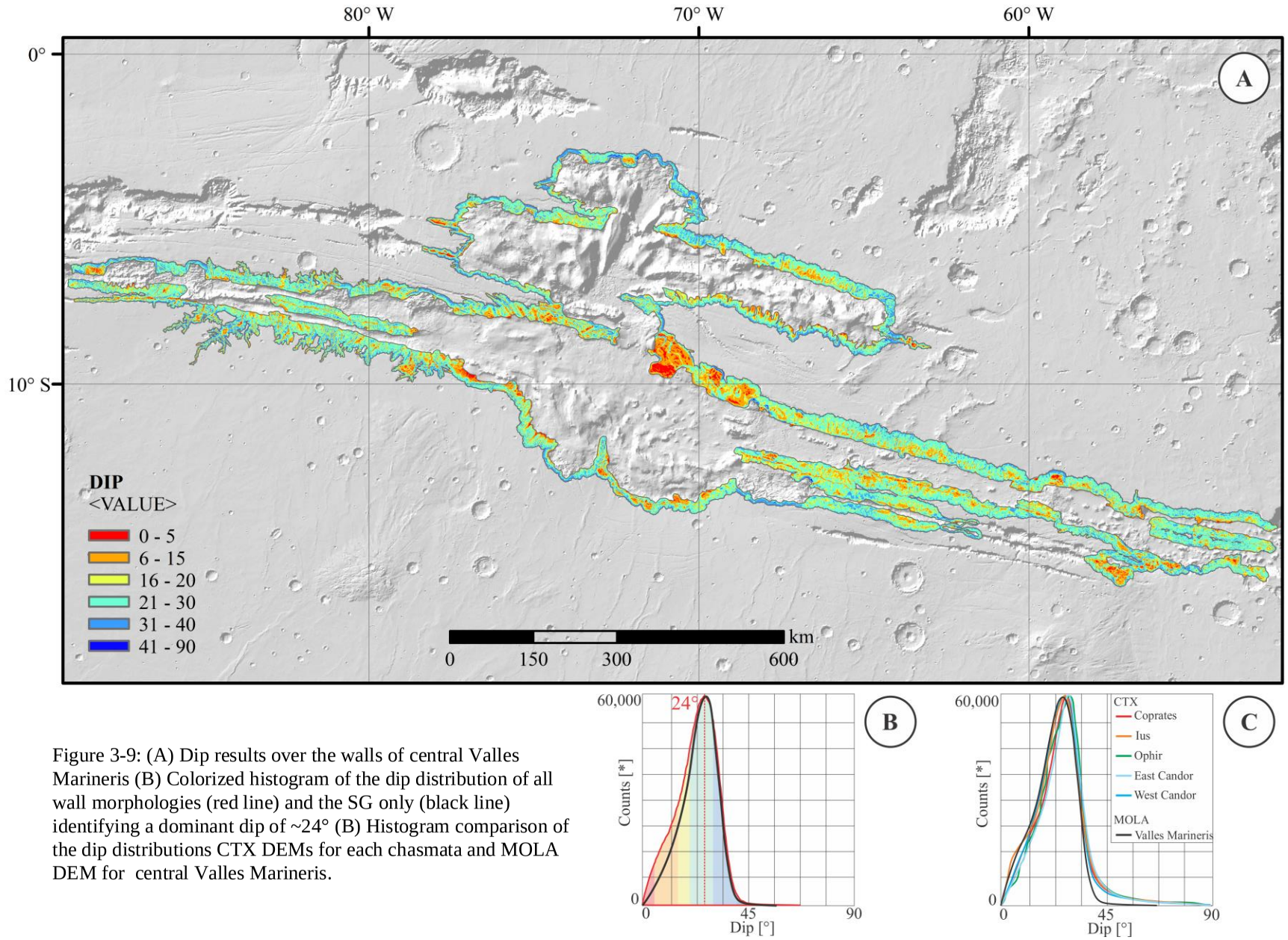

Figure 3-9: (A) Dip results over the walls of central Valles Marineris (B) Colorized histogram of the dip distribution of all wall morphologies (red line) and the SG only (black line) identifying a dominant dip of ~24° (B) Histogram comparison of the dip distributions CTX DEMs for each chasmata and MOLA DEM for central Valles Marineris.

The steep sections of the walls are associated with the faulting that formed the scarp. The comparison of the dip distribution at different resolutions shows a discrepancy for values >40° (Figure 3-9C). The discrepancy appears on Figure 3-9C as a lower distribution of pixels. This is associated with the quality of the DEMs since CTX DEMs made in-house have artifacts such as spikes and voids in them, while HRSC DEMs are smooth. This can be noticed on Figure 3-4 where both resolutions are used and compared.

Inspection of the distribution among the chasmata suggests that the walls of Coprates Chasma have possibly suffered the most recent erosion based on the amount of shallower areas within its surface in comparison with other chasmata (Figure 3-10A). Candor Chasma shows shallower areas with smaller ridges near the interior layered deposits of the southern side floor (Figure 3-10B). Clusters of shallower dips on the southern walls of Candor appear to be the result of the wall including the southernmost extent of the interior layered deposits (Figure 3-10B). As has been demonstrated elsewhere, these interior layered deposits drape on top of wall morphology [Fueten et al., 2017]. Noticeably, the northern wall of Candor Chasma show clusters of relatively shallow slopes that are related to faulting along the wall. This location will be explored in further sections.

The connection between the dip ranges and certain features is the result of observations and comparison of the areas where the dip ranges formed cluster and what feature is observed on that exact location. The ranges provide suggestions of what possible features and formations could be located on the walls prior to inspection of the imagery.

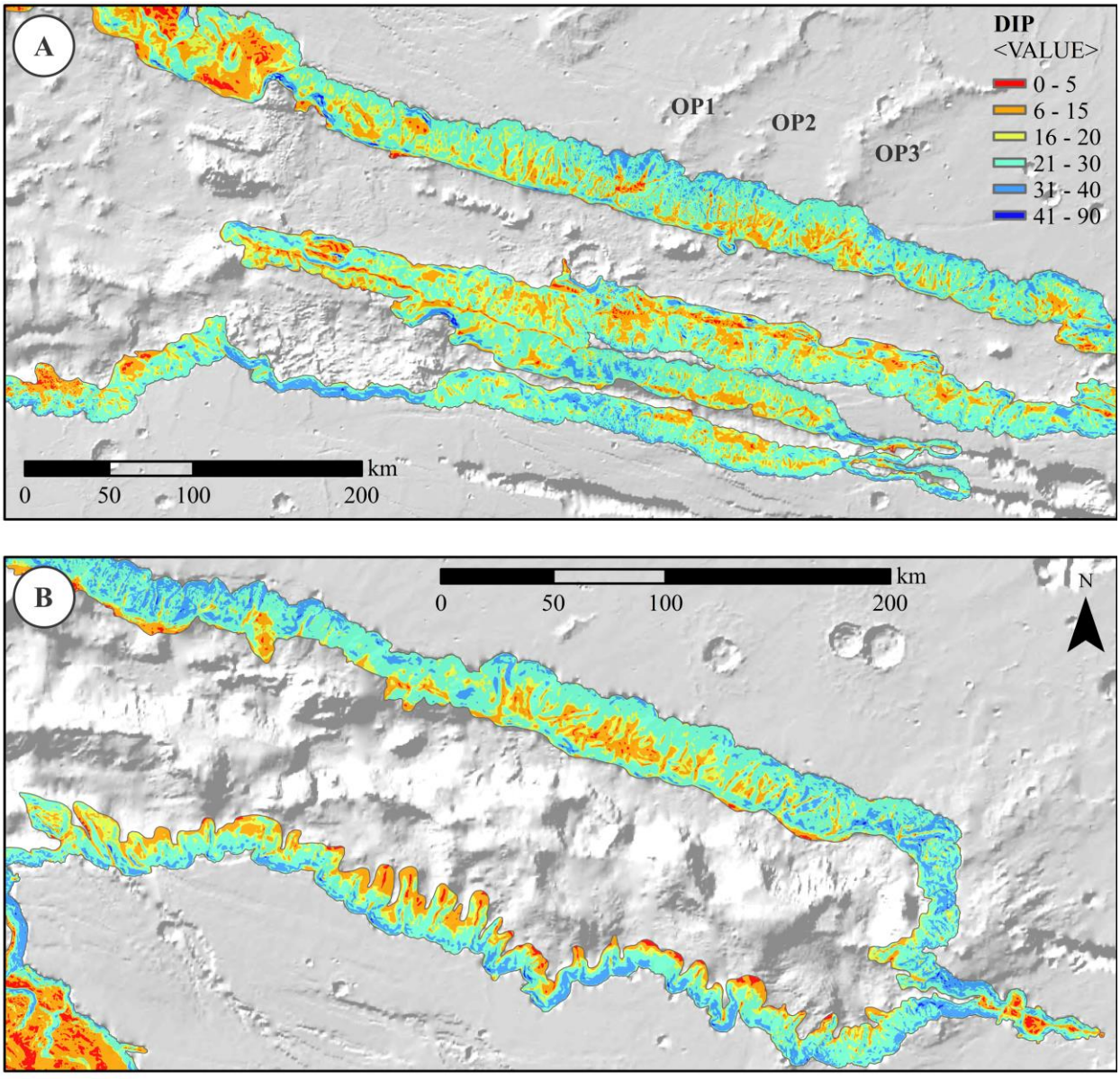

Figure 3-10: Dip results over the walls of (A) Coprates Chasma, and (B) Candor Chasma.

3.3.2.2. Identification of ridges and troughs

The dip analysis inferred which features are associated with certain slopes and the stability of them. This section will analyze the ridges and troughs that can be identified within the walls. To do so the MSSD analysis was used. The MSSD results highlight the large concentration of tributaries located at Ius Chasma including the identification of ridges formed by the intersection of these tributaries (Figure 3-11A). The results shows that the spurs on the flanks of Geryon Montes are less pronounced compared to the well-defined spurs identified on the northern walls of the chasma (Figure 3-11A). The north walls of Ius Chasma show well defined spurs at various angles along the walls differing from the expected downslope orientation (Figure 3-11A).

Ophir Chasma has surfaces with similar, less pronounced spurs and few pronounced or well-defined spurs scattered around the walls of the chasma (Figure 3-11B). This probably relates to the processes and conditions involved in the formation of the chasma [Sharp, 1973; Lucchitta, 1978]. The irregular shape of Ophir Chasma limits any dominant orientation of the spurs in comparison to other chasmata such as Ius Chasma, which has a long rectangular shape. The shape of Ius chasma allows the comparison of the formed spurs on facing walls.

Comparison of the walls of Ius Chasma shows that the spurs that formed near the tributaries are large long spurs that have a similar orientation as other formations like grabens, as seen on the mid-section of the northern wall (Figure 3-11A). In Chapter 2, a similar case was introduced where spurs formed over pre-existing structures in the Tharsis province as suggested for the long ridge that extends from the walls of Melas Chasma (Figure 3-11C), although not all the chasmata have large long spurs.

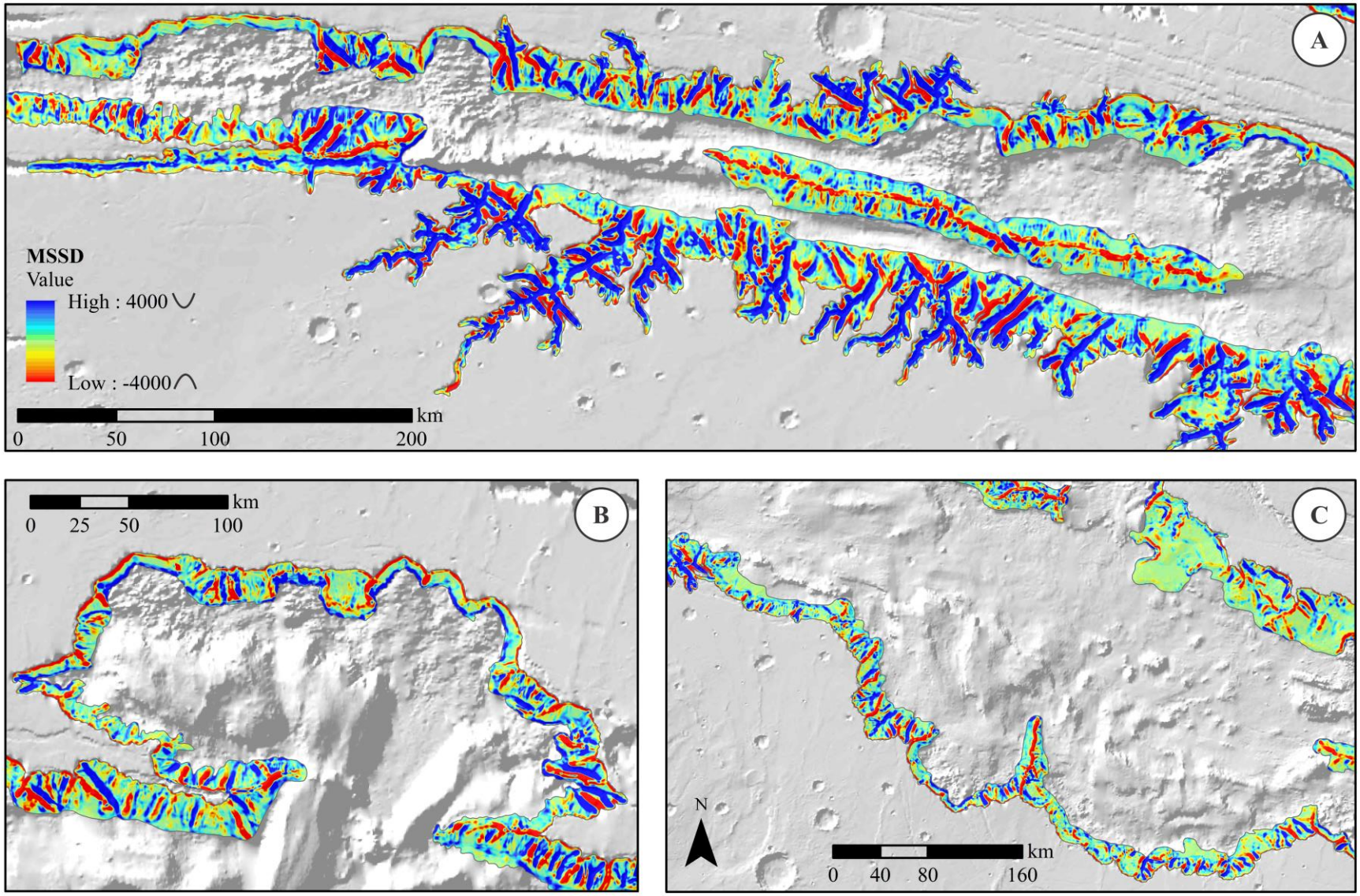

Figure 3-11: MSSD results of the walls of Valles Marineris showing the distribution of ridges and troughs on (A) Ius Chasma, (B) Ophir Chasma (C), Melas Chasma.

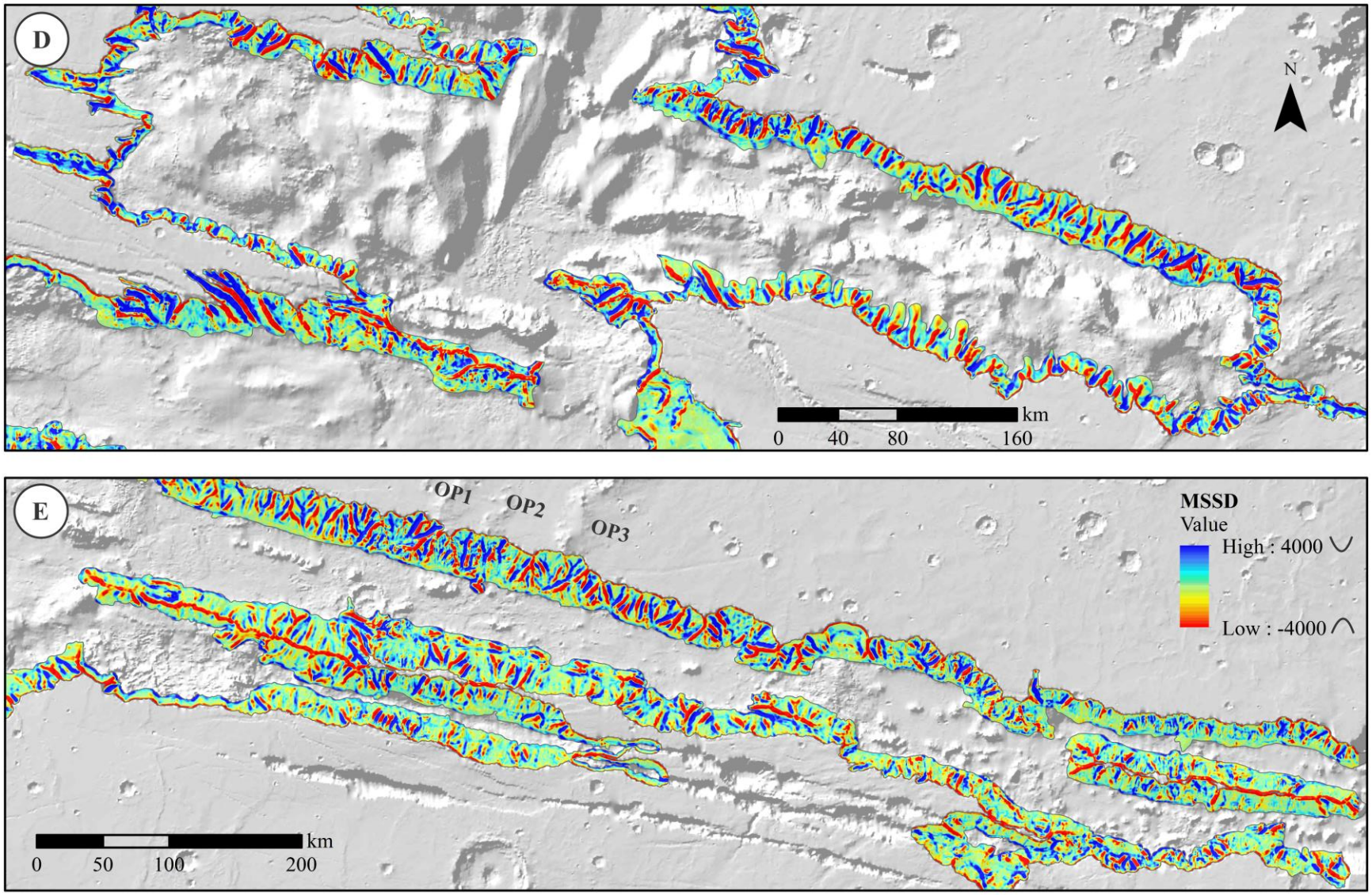

Figure 3-11: (D) Candor Chasma, and (E) Coprates Chasma.

Notably, Candor Chasma has a variable formation and distribution of spurs (Figure 3-11D). Comparison of West and East Candor Chasma shows a variation from east to west and between facing walls (Figure 3-11D). West Candor appears to have less pronounced spurs compared to East Candor Chasma. The south wall of West Candor Chasma has not only less pronounced but also fewer spurs (Figure 3-11D). When comparing both facing walls of East Candor Chasma, it appears that the south walls have fewer spurs than the north walls (Figure 3-11D).

Coprates Chasma has a similar distribution of spurs to Candor Chasma along the north walls of western Coprates and the north walls of East Candor (Figure 3-11 D&E). The distribution of spurs from western to eastern Coprates Chasma varies from large and highly pronounced (i.e. sharp crest) spurs to shallower and narrow spurs (Figure 3-11E). This variation of spurs from west to east indicates an association between the depths of the chasma that affected the morphology of the spurs as it is noticed that large highly pronounced spurs are located on walls of greater dimensions.

The south walls of Coprates Chasma have a similar distribution to the facing northern walls having less pronounced spurs towards east (Figure 3-11E). Other areas within the chasma such as Coprates Montes have shorter wall with less pronounced spurs, similar to Geryon Montes (Figure 3-11E). This is also noticed within the southern small trough at western Coprates formed by the extension of pit chains that formed parallel to the chasma.

The presence of tectonic features near western Coprates, such as wrinkle ridges visible on the surrounding plana and grabens located on Ophir Planum and Coprates Montes, indicate that pre-existent faults formed the base for the large long spurs (Figure 3-11E). Proof of this appears on the spurs of the north wall adjacent to Ophir Planum. Within this wall, some well-defined

spurs have been linked to structural influence (Chapter 2). Along Coprates Montes large E-W faults systems run leaving traces of structural influence on the montes (Figure 3-11E).

Long, narrow spurs observed along on the walls of chasmata such as Ius Chasma and West Candor Chasma (Figure 3-12) appear as an expression of erosion due to dry mass movements along the faults of the grabens on the surrounding plateau (Figure 3-12 A, C, & E). Their formation is possibly associated with the relative orientation of the fault planes to the walls. This is suggested due observations of large gullies associated with localized erosion of the walls, possibly because of pre-existing conditions or weakening of the wallslope eroding the walls into the plateaus changing the attitude of the walls. It is suggested that these spurs are the result of structural influence since they might have formed along the pre-existing fault planes from where they inherited their attitude (Figure 3-12).

Long spurs lead to the appearance of other features such as secondary spurs or small spurs that extend along the eroded flank of the large long spurs (Figure 3-12 B, D, & F), although the small spurs do not appear on all the eroded flanks since small spurs are not identified within the surface of tributary canyons (Figure 3-12 A&B). The presence of these small spurs along the flanks indicates structural control based on their alignment with features on the plateau such as grabens (Figure 3-12 A&E). Nonetheless, not all the features are associated with faults or fractures may be visible on the surface as it appears on the wall of Ius.

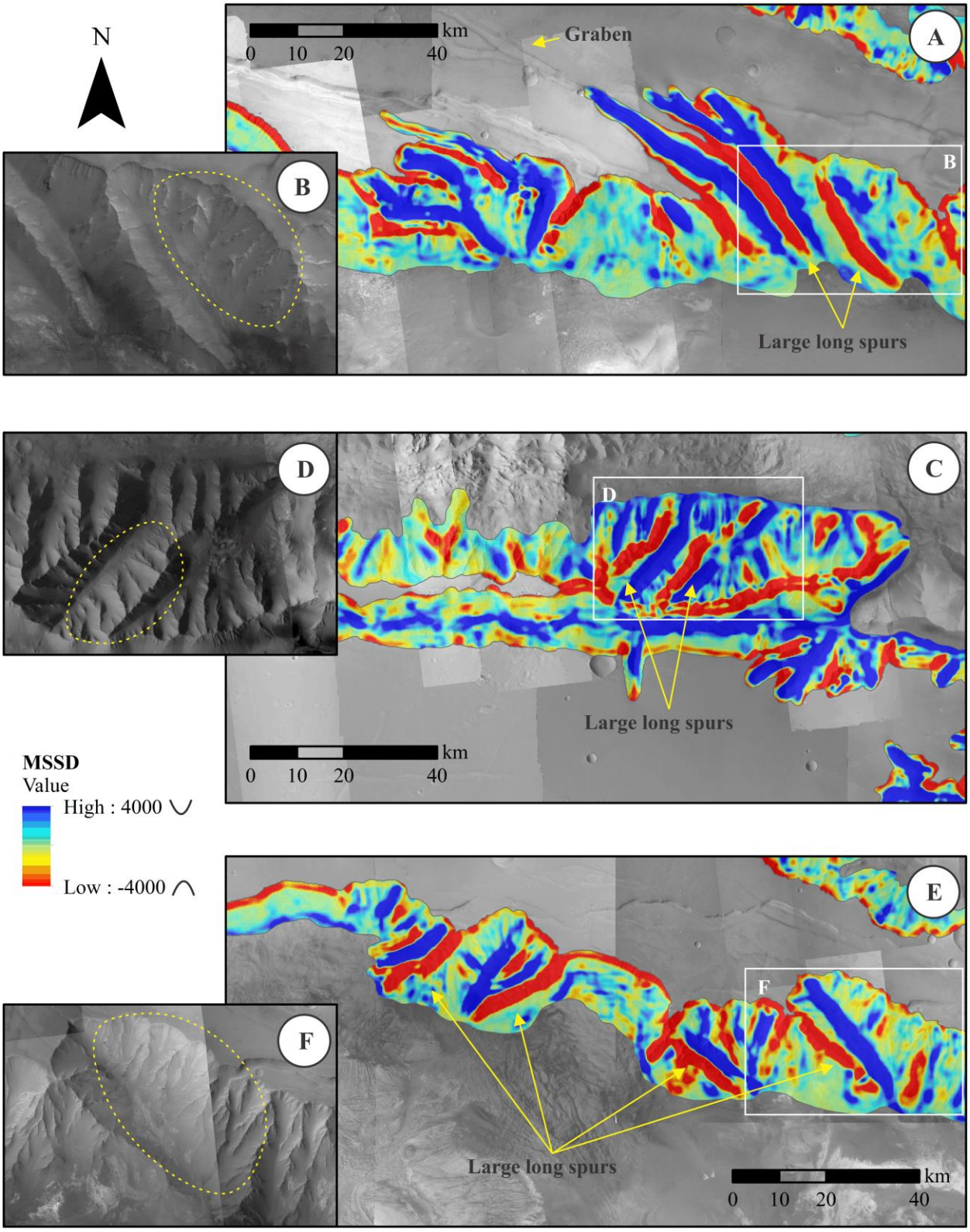

Figure 3-12: (A,C,E) Large long spurs on the walls of (A) East Ius Chasma (C) West Ius Chasma, and (E) West Candor Chasma. (B,D,F) close-up with dashed circled areas that show secondary spurs or small spurs on the flanks of the large long spurs.

3.3.2.3. Patterns and anomalies on the walls

The walls of Valles Marineris have a wide range of attitudes, however a general attitude can be inferred for those chasmata with rectangular shape. The processes that involved collapses and breakthroughs (e.g. landslides, tributaries) changed the attitude of the walls. Similar changes in attitude are observed near structures such as grabens and wrinkle ridges, these ones leaving traces of their influence [Blasius et al., 1977; Lucchitta, 1978; Peulvast et al., 2001; Cole and Andrews-Hanna, 2012].

For example, previously suggested traces of structural influence on the walls of East Candor Chasma (Figure 3-13D) [Blasius et al., 1977] appear as a distinctive disrupted SG wall morphology. The disruption of the surface is noticed within the dip (Figure 3-13A) yet this was not easy to differentiate from other type of features. The MSSD recognized an anomaly but was not able to indicate a possible origin due the specified sampling size. The use of the AVA appears to facilitate the recognition and interpretation of this type of geometry on the walls (Figure 3-13 C&D), as it readily highlights the contrasting colors of the attitudes (Figure 3-13C). This indicates that each methodology has uses and criteria necessary to properly analyze the morphology of the walls.

In Chapter 2, certain features appear highlighted using the AVA analysis due to their anomalous attitude, which differs in orientation from that of the surrounding walls (Figure 3-14). These features were referred to as Anomalous Planes (APs) in Section 2.5 where it was suggested that their presence is associated with pre-exiting faults formed during the extension of the Tharsis bulge. These APs are the expression of the pre-exiting faults on the walls, visible due the relative angle between the faults and the walls (Figure 3-14).

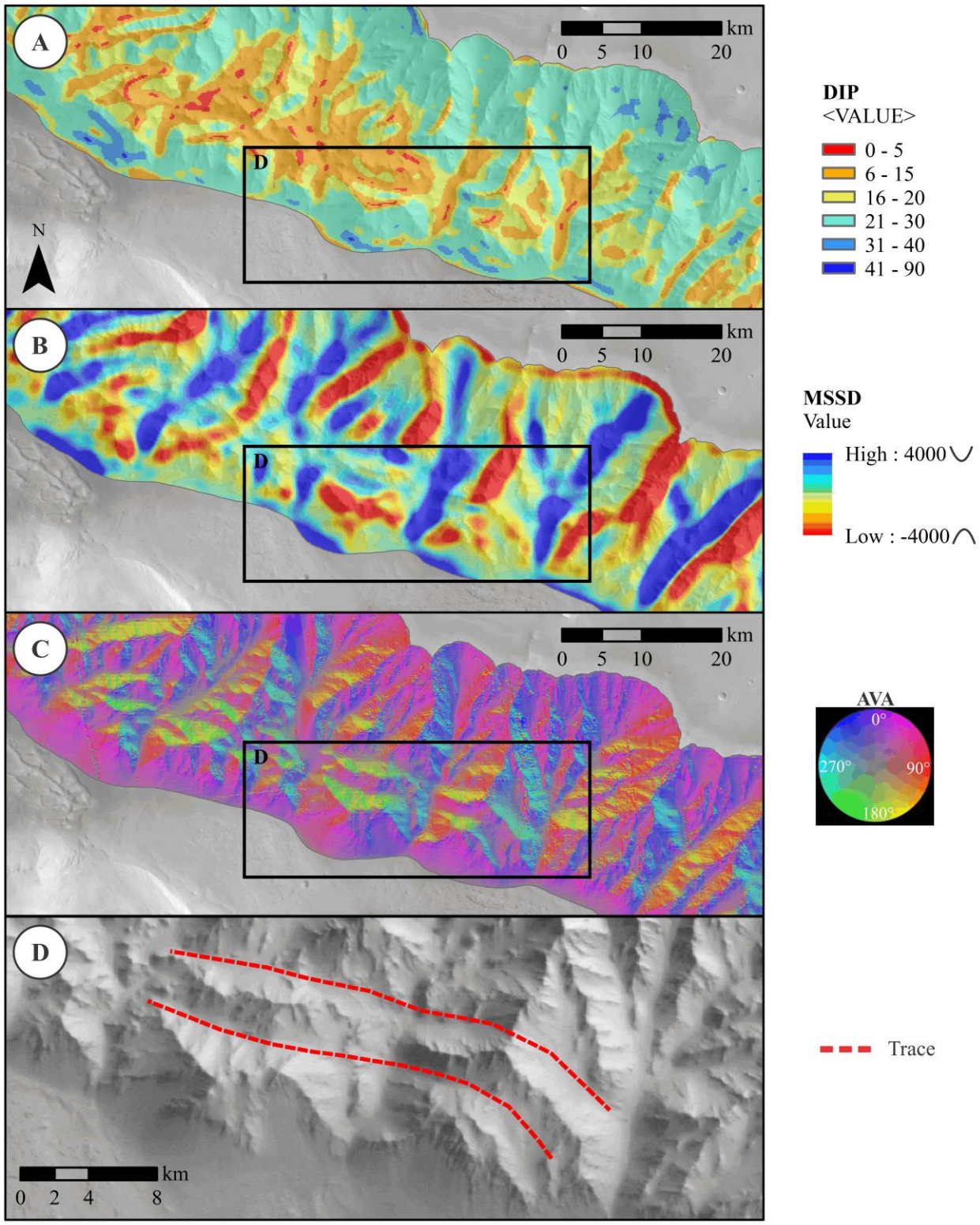

Figure 3-13: (A, B, C) North wall of East Candor Chasma using (A) dip, (B) MSSD, and (C) AVA analysis. (D) Close up of wall collapse, red dashed lines represent traces of fault planes.

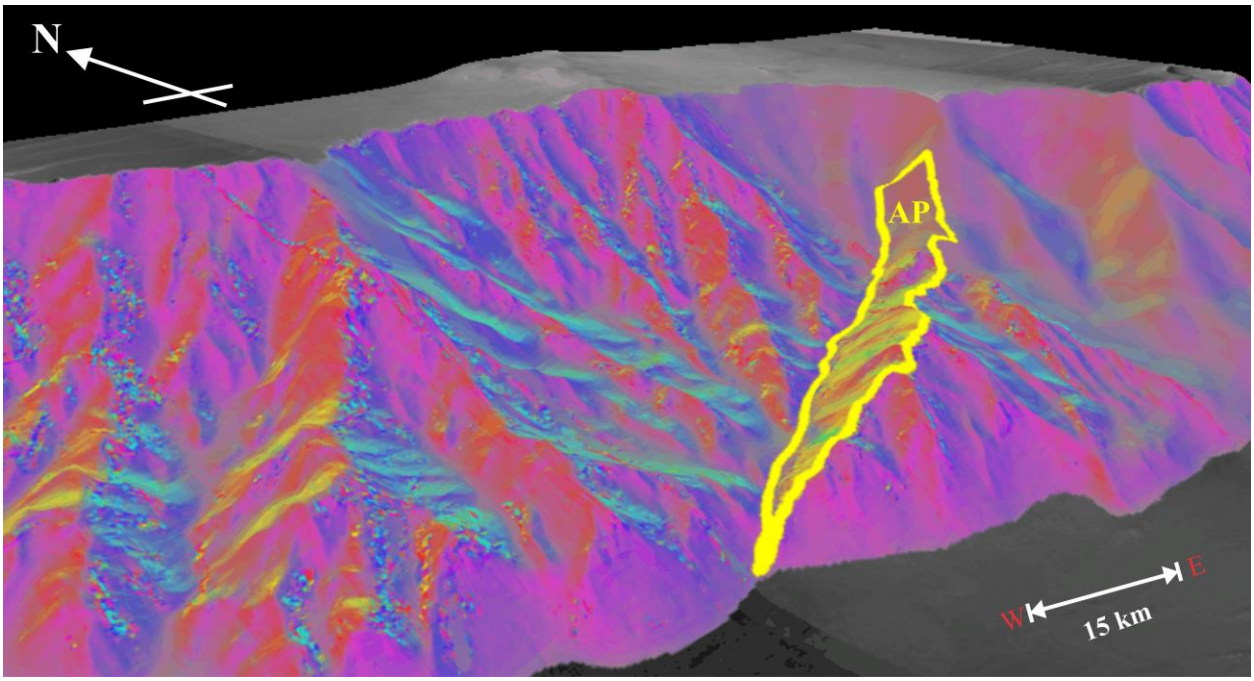

Figure 3-14: 3D projection of an AP on the northern wall of Coprates Chasma using the AVA color scheme [Chapter 2]. 2x V.E.

The anomalies differentiate by their morphology where the disrupted pattern on Figure 3-13C is considered the result of chasma producing faults, since they extend along the strike of the wall. The anomaly on Figure 3-14 is considered the result of pre-exiting fault planes and it will be referred to as APs due its attitude that dips into the wall and its diagonal extent on the walls. A total of 24 APs were located within the walls of central Valles Marineris (Figure 3-15). These planes were recognized due their anomalous attitude and are considered as expressions of pre-existing structures within the Tharsis province. It is possible that more APs might have existed yet the processes involved in the formation of Valles Marineris might have erased the APs. It is also probable that some faults do not have an expression on the walls due their orientation relative to the attitude of the walls. Observation of the identified APs shows that they appear only on the north and south facing walls, but not the east and west facing walls. APs on the north walls stand out due the contrast of colors unlike those APs on the south walls that may not stand out as readily (Figure 3-15).

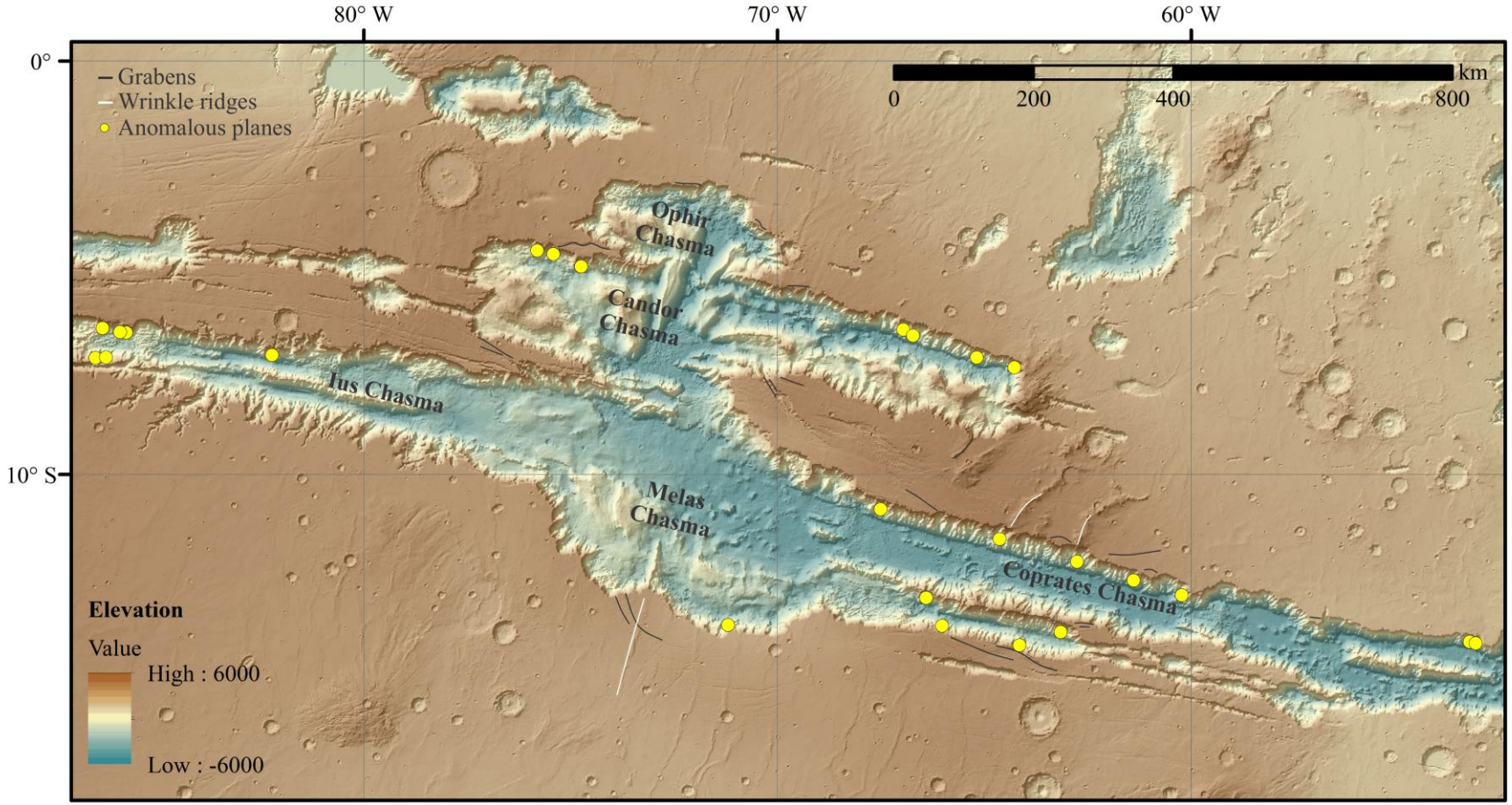

Figure 3-15: Identified APs on the walls of central Valles Marineris and structures crossing the walls suggesting a possible connection among some of them.

3.4. Detailed analysis of the spurs and SG wall morphology

3.4.1. Techniques and methodologies

The detailed analyses of the spurs and the SG wall morphology, examines the associated geometry between the SGs and the walls. The analyses rely on the use of DEMs to measure specific values of the SG wall morphology observed on the imagery.

The geometric elements include the length, throw, and slope of the walls, as well as the geometry of the elements that compose the SG wall morphology. It also includes the orientation of the spurs along the wall (i.e. rake). These methods are applied to those areas of the SG wall morphology that show competent spurs and exclude all the areas where no spurs are observed or where spurs are disrupted due to collapse. The excluded areas cannot provide reliable information associated with the studied geometry.

3.4.1.1. Division of the walls and applied criteria

The walls of central Valles Marineris are divided to differentiate the areas that have the most consistent and representative SG wall morphology. The walls are described as inclined surfaces that link the nearly horizontal surfaces of Valles Marineris (i.e. the plateau and floor). Sections of the chasmata where large areas of the floor are covered by interior layered deposits [Fueten et al., 2008; Murchie et al., 2009; Tanaka et al., 2014] are included in the analyses since the adjacent walls appear competent. Certain areas within Coprates Chasma were excluded due to breakthroughs across them formed by possible faulting [Witbeck et al., 1991].

Coprates Montes and Nectaris Montes were included for the analyses of the walls due the presence of SGs on their surfaces even though MSSD results show that the spurs in those areas are smaller in comparison to the spurs on the walls. These montes have remnants of plateau that emulate competent upper horizontal surfaces even though their original elevation might have been different. Geryon Montes in Ius Chasma is excluded due the lack of an upper horizontal surface, as well as having a low relief in comparison to Coprates Montes and Nectaris Montes (Figure 3-16) [Witbeck et al., 1991].

Other criteria related to the consistency of the shape of the SGs and their developed geometry exclude sections of the wall with no spurs or disrupted ones (e.g. south wall of West Candor Chasma). Part of the criteria used to select sections of the walls take into account the simplified geometry of the SGs and the results from previous analyses (i.e. dip analysis, MSSD analysis, and AVA analysis). As result, several sections of the walls within the SG wall morphology were selected to measure the geometry of the walls and the orientation of the spurs in these areas (Figure 3-16). The following sections show analyses made using: Length-Throw-Slope analysis and pitch or rake analysis.

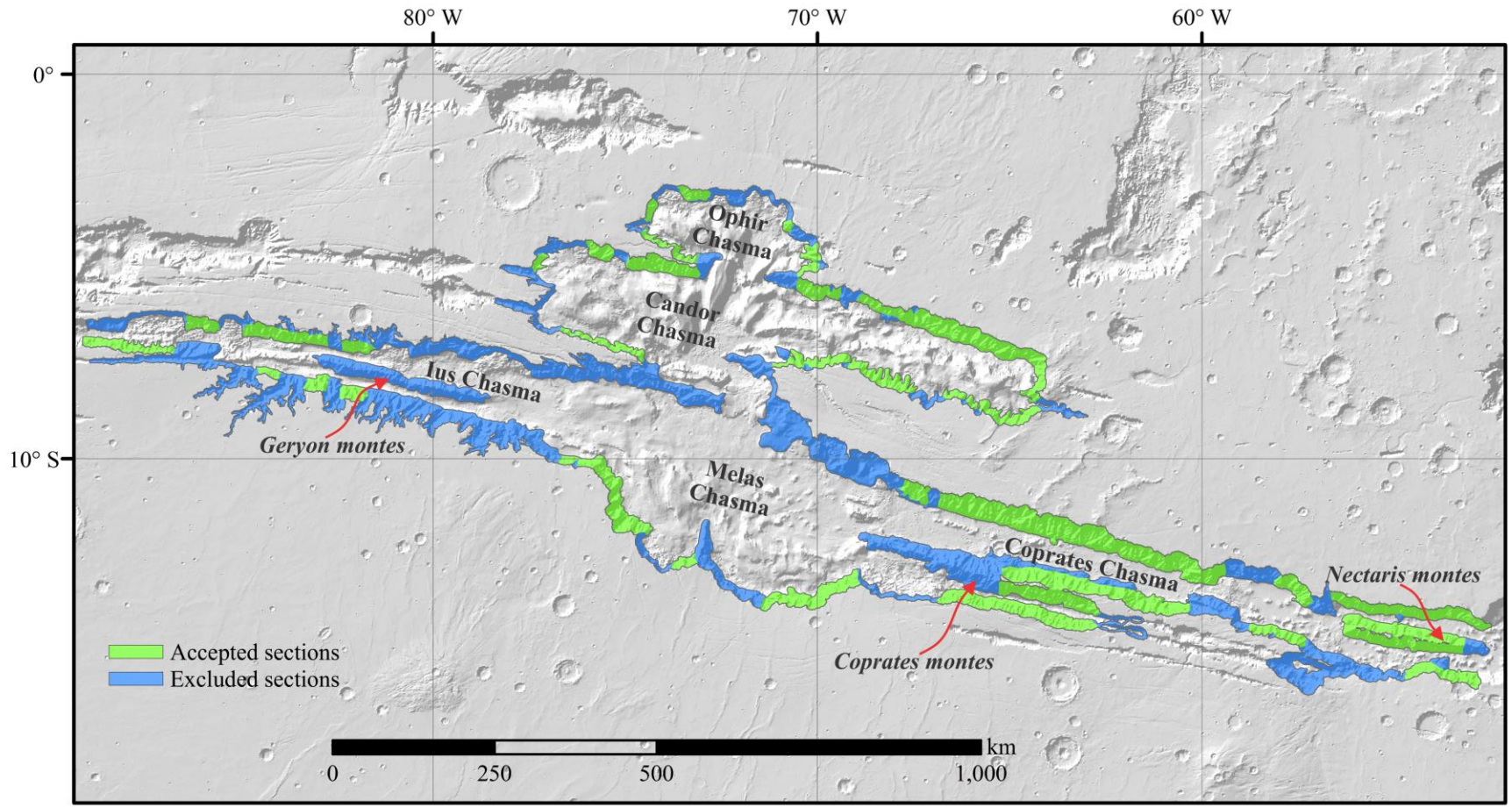

Figure 3-16: Division of the walls of central Valles Marineris where the green areas highlight the accepted sections to be analyzed and blue highlight the excluded sections.

3.4.1.2. Length-Throw-Slope (LTS)

The LTS methodology measures topographic profiles along the dip direction of the walls to determine the general geometry of the walls. The profiles are measured along the selected areas of the SG wall morphology (Figure 3-16). The profiles are perpendicular to the strike of the walls, usually tracing along spurs varying in length depending on how eroded the wall is and avoiding the headwalls (Figure 3-17). Each profile is analyzed in order to determine any change in the curvature of the spurs and the wall. The results are comparative graphs like a Length – Throw graph or diagram with all the measurements from the chasmata.

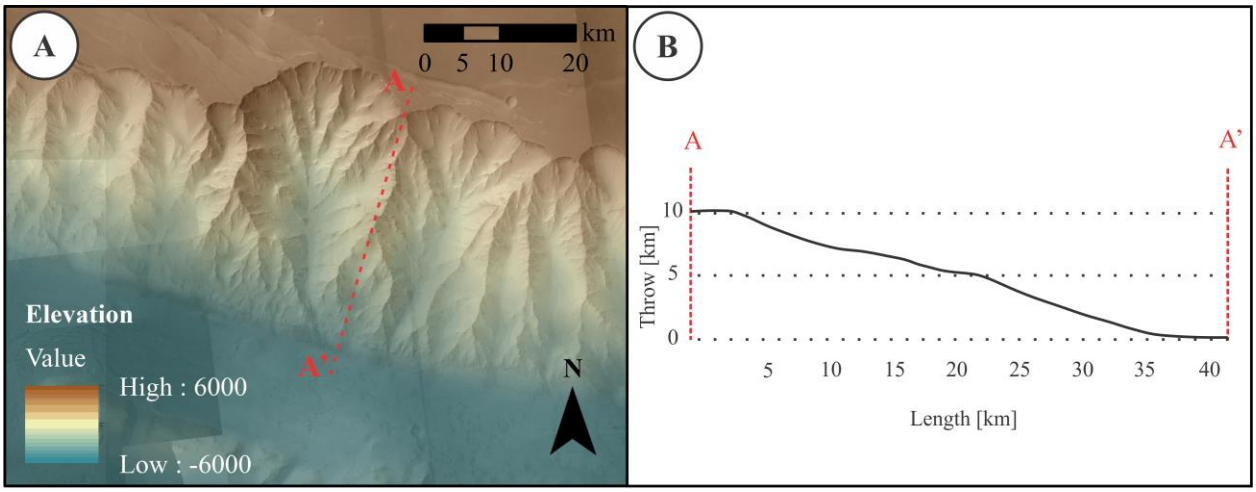

Figure 3-17: (A) North wall of Coprates Chasma showing a (B) topographic profile A-A' along a well-defined spur 4x V.E.

3.4.1.3. Pitch or rake analysis

Linear features were drawn over the crests of spurs going from the highest to the lowest elevation of the spurs along their respective chasma and section of the SG wall morphology and following the right hand rule (Figure 3-18A). The selected spurs are those that show higher curvature values in MSSD and have representative lengths (e.g. lengths >10 km), although smaller spurs like those on West Candor Chasma and Nectaris Montes are included as well in the analysis.

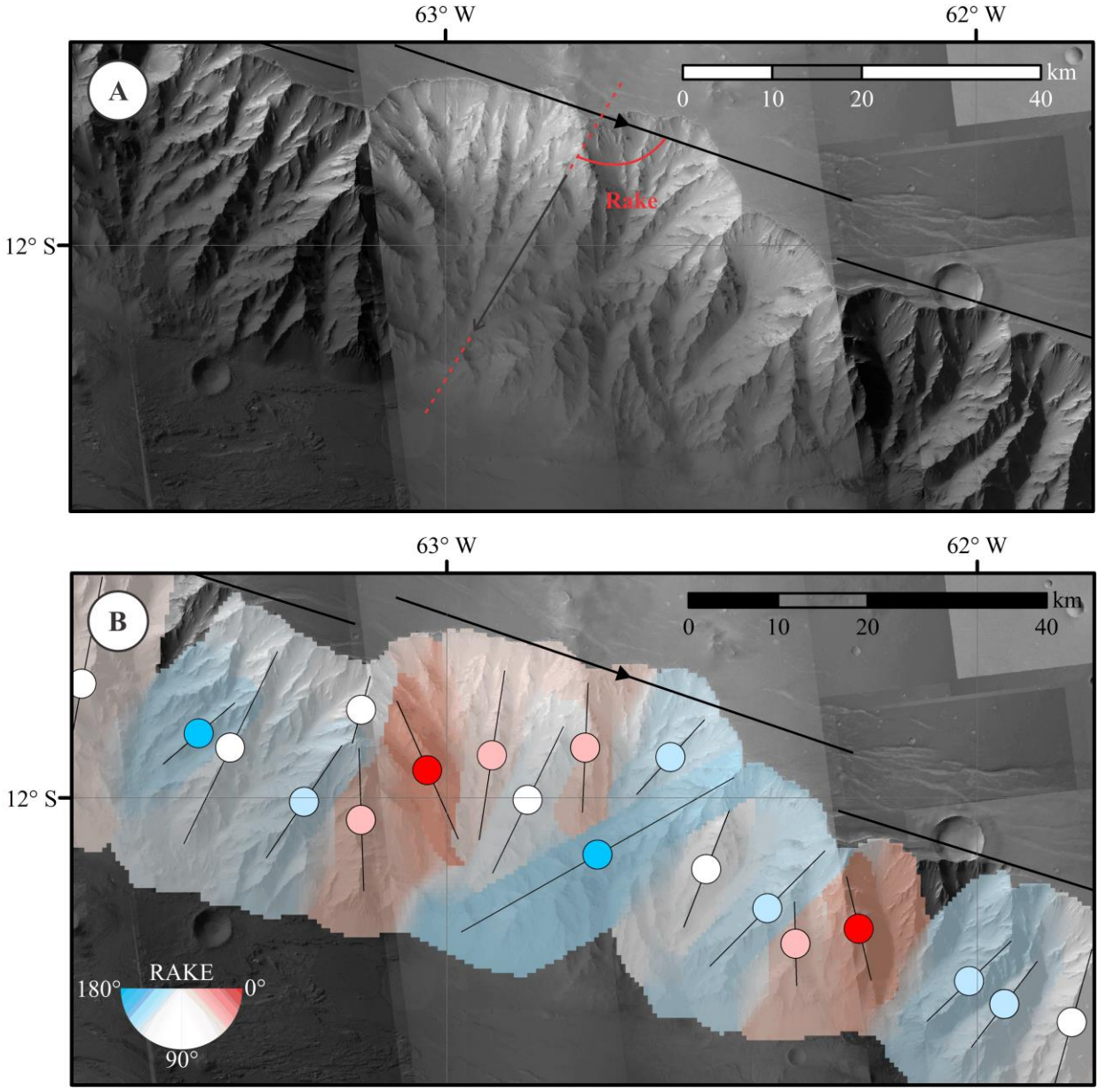

Figure 3-18: (A) Measurement of the rake of a spur on the north wall of Coprates Chasma (B) Example of results of the rake analysis with its characteristic color scheme.

The calculation of the attitude of the spurs considers the attitude of the nearest reference plane of the wall, as follows. The strike of the wall is drawn as a linear feature orthogonal to the dip direction of its respective surface, disregarding the presence of the headwalls (Figure 3-18A). The rake angle represents the relative angle of the spur crest on its respective section of the wall

(Figure 3-18A). The rake is the inner angle between both features and is determined on a projected horizontal plane. The use of the angle projected on a horizontal plane does not affect the rake value since it was calculated on a horizontally rotated plane. The rake angle is classified using a color scheme that indicates the orientation of the spurs showing its deviation from the expected downslope orientation (Figure 3-18B).

In order to have a better interpretation of the results, a line density distribution is determined to show the most significant rake values of the spurs within each selected section of the wall (Figure 3-18B). The line density distribution appears as a raster projected over the walls to help the visualization, and interpretation of the results. Histograms are calculated as well to determine the distributions of the rake and any possible dominant orientation within the distribution are made for each chasmata.

3.4.2. Results

3.4.2.1. Length of the spurs wallslope

The topographic profiles measured the extent of the walls with SG wall morphology along the spurs (Figure 3-19 A&B) resulting in the recognition of different shapes of wall profiles (Figure 3-19 C&D). These spurs appear on walls in many areas of the SG wall morphology with an average length of ~20 km.

The profiles reveal that the spur crests have a shape that varies from a straight line to slightly concave (Figure 3-19 A&C), yet some spurs have a convex shape as seen in the north walls of Ophir Chasma (Figure 3-19 B&D). This convex shape suggests that this section of the walls might have internally failed creating subsurface movement that buckled the wallslope (Figure 3-19D).

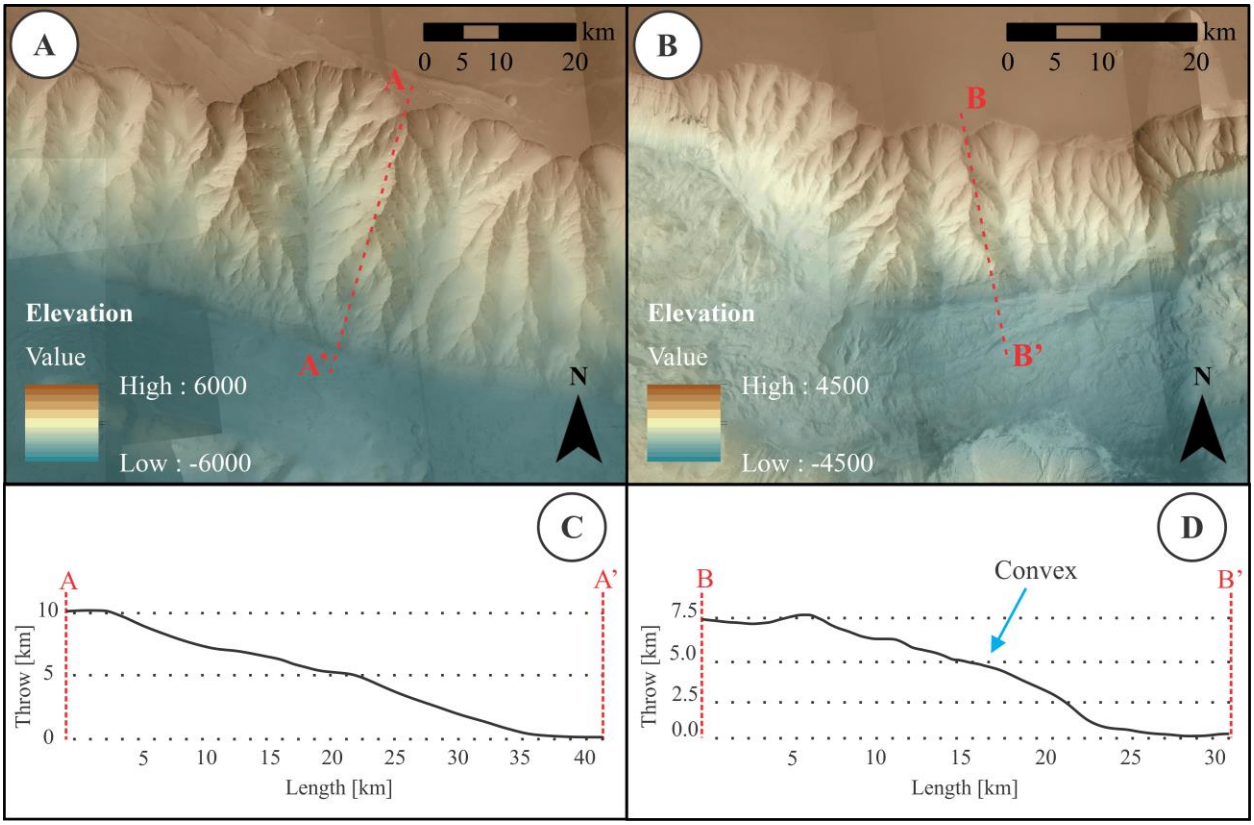

Figure 3-19: (A,B) North wall of (A) Coprates Chasma and (B) Ophir Chasma showing the respective topographic profile (C) A-A' and (D) B-B'; both 4x V.E..

A total of 164 LTS measurements were made throughout central Valles Marineris to compare the extent of the walls of the chasmata (Figure 3-20). The comparison indicates that chasmata such as Coprates Chasma, Ius Chasma, and Candor Chasma have greater range of surface extent (Figure 3-20) suggesting that these chasmata are deeper and hence the spurs have a greater throw and length.

Coprates Chasma has the wider range of extent in comparison to the other chasmata having a throw between 4-10 km and a length that goes from 10-35 km (Figure 3-20). The values decrease gradually towards east of the chasma (Figure 3-16). This resembles the observed variation on the MSSD results that indicate that the walls of Coprates have shorter and less pronounced spurs on the eastern region.

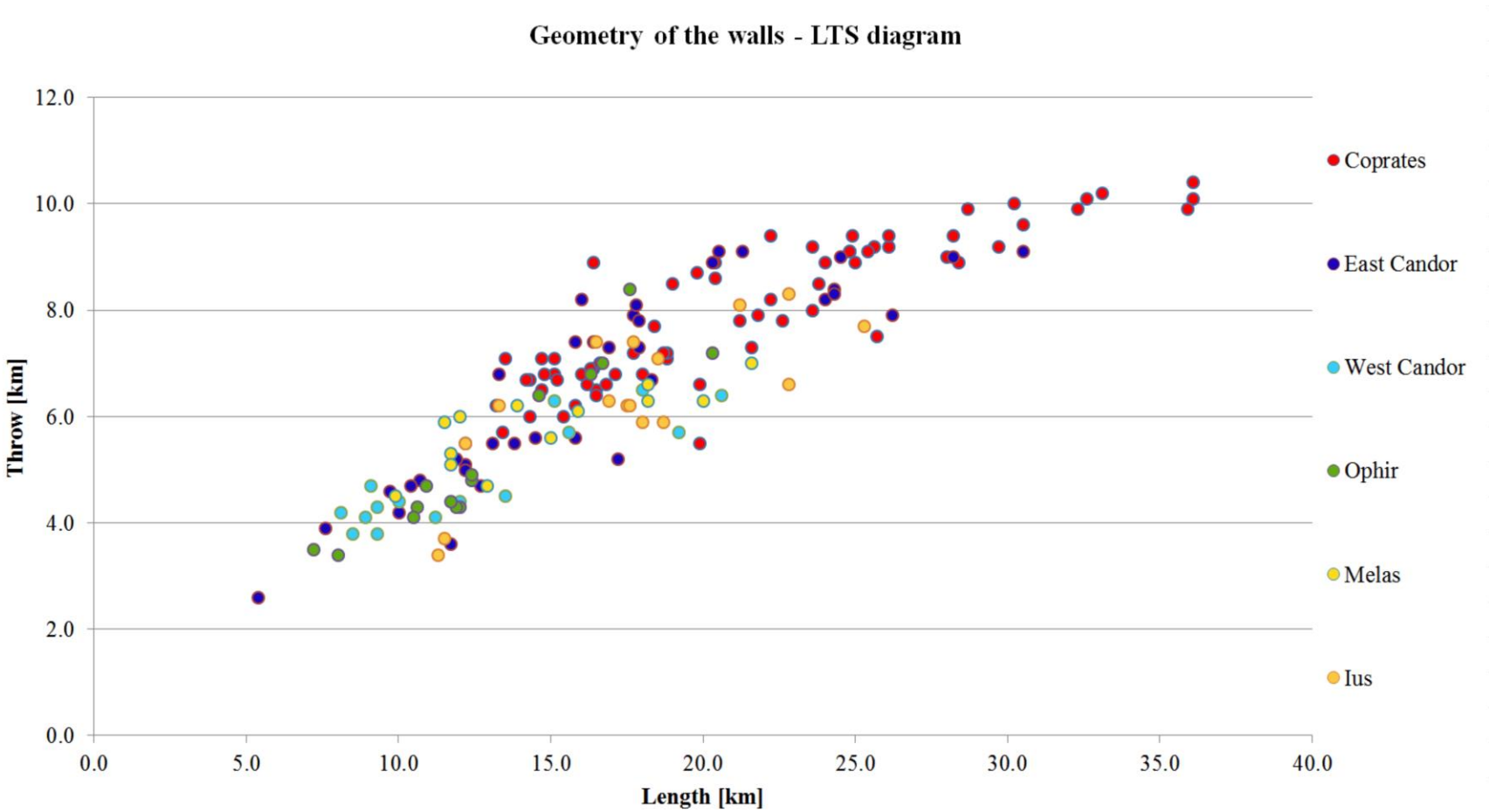

Figure 3-20: Comparison of the geometry of the walls of central Valles Marineris using the length and throw from topographic profiles across SG wall morphology.

The profiles were used to calculate an average slope of the walls using the spur crests resulting in a value of 21 ± 3°. This result is a slope that agrees with the dominant inclination of ~24° found from the dip analysis (Figure 3-9B). The dip analysis considered every pixel of the DEM that covers the walls to identity singular planes of the overall surface whereas the LTS analysis determines the dip in those areas with well-defined spurs. The similarity of these values suggests very consistent slopes for the chasmata similar to the stable slope of Mars [Schultz, 2002; Kleinhans et al., 2011]. The results were compared to Rock Mass Rating (RMR) values used by Schultz [2002] to evaluate the stability of the spurs of Valles Marineris (Figure 3-21).

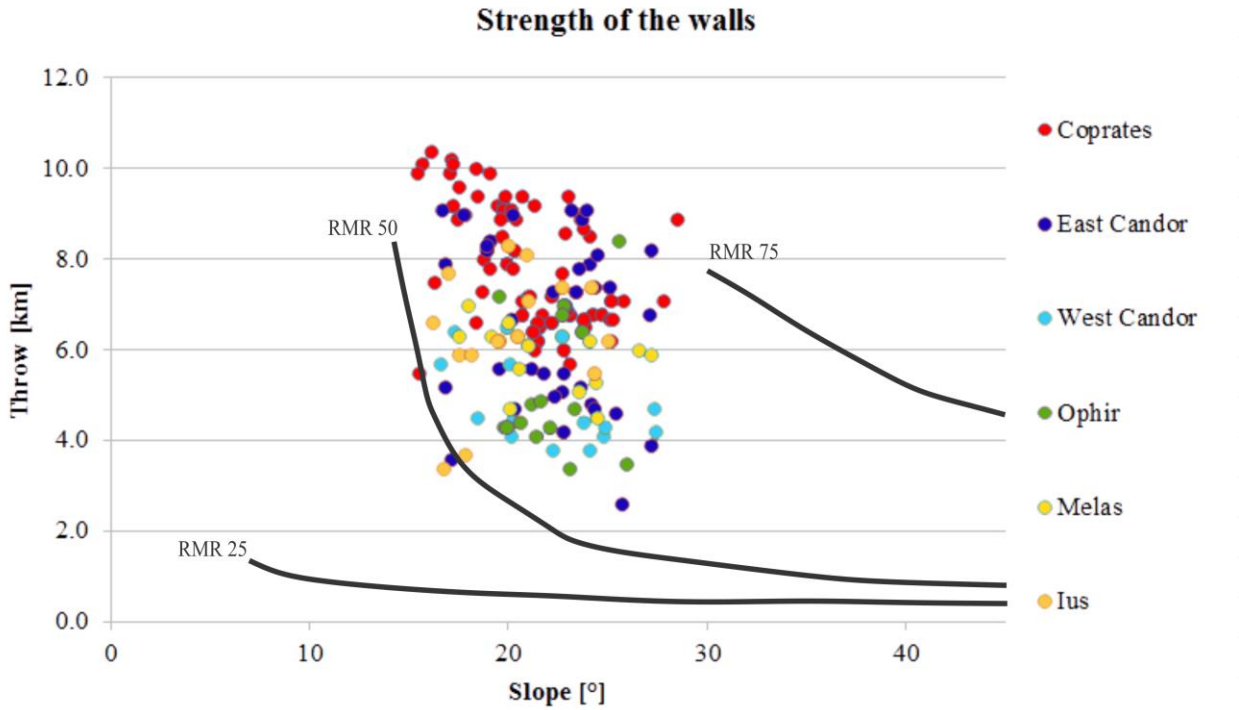

Figure 3-21: Comparison of the geometries of the walls of central Valles Marineris as a strength diagram using RMR values from Schultz [2002].

The RMR quantifies the stability of slopes based on their geometry, the stresses involved, and the conditions of the rock using mechanical properties of rocks that are comparable to the lithology of Mars [Bieniawski, 1993; Schultz, 2002]. According to Schultz [2002], the strength of the wallrock is observed within a RMR range of 50-65 suggests that the measured sections of SG wall morphology are stable.

3.4.2.2. Characteristic values of the SG morphology

The average attitudes of the elements of the SG wall morphology were measured using the topographic profiles. The results indicate that spurs plunge within values of 10-25° on the walls (Figure 3-22A). This range describes the angle of spurs of various lengths including the well-defined and small spurs. Forming the sides of the spurs are the flanks, planar features with dips between 25-35° where the higher values for those planes are associated with structural control. Observations of the flanks of the spurs show the presence of lateral spurs. These lateral spurs are considered as remnants of the extensional processes linked to the facets (Figure 3-22B).

Located at the top of the wall are the headwalls with curved outlines formed by the collapse or retreat of the rim that covers the surface with talus (Figure 3-22A). The surface of headwalls dips 20-30° concentric to gullies shaped like a conical segment or an amphitheater that ends into a gully. The eroded material from the surface and the flanks flows as debris accumulating and covering the gullies and sometimes creating small basins that dip 5-15° (Figure 3-22A). Triangular facets form as fault planes cut and offset ridges [Peulvast et al., 2001]. Their attitude becomes shallower than the fault that originated them, currently appearing with angles of 15-25° (Figure 3-22A).

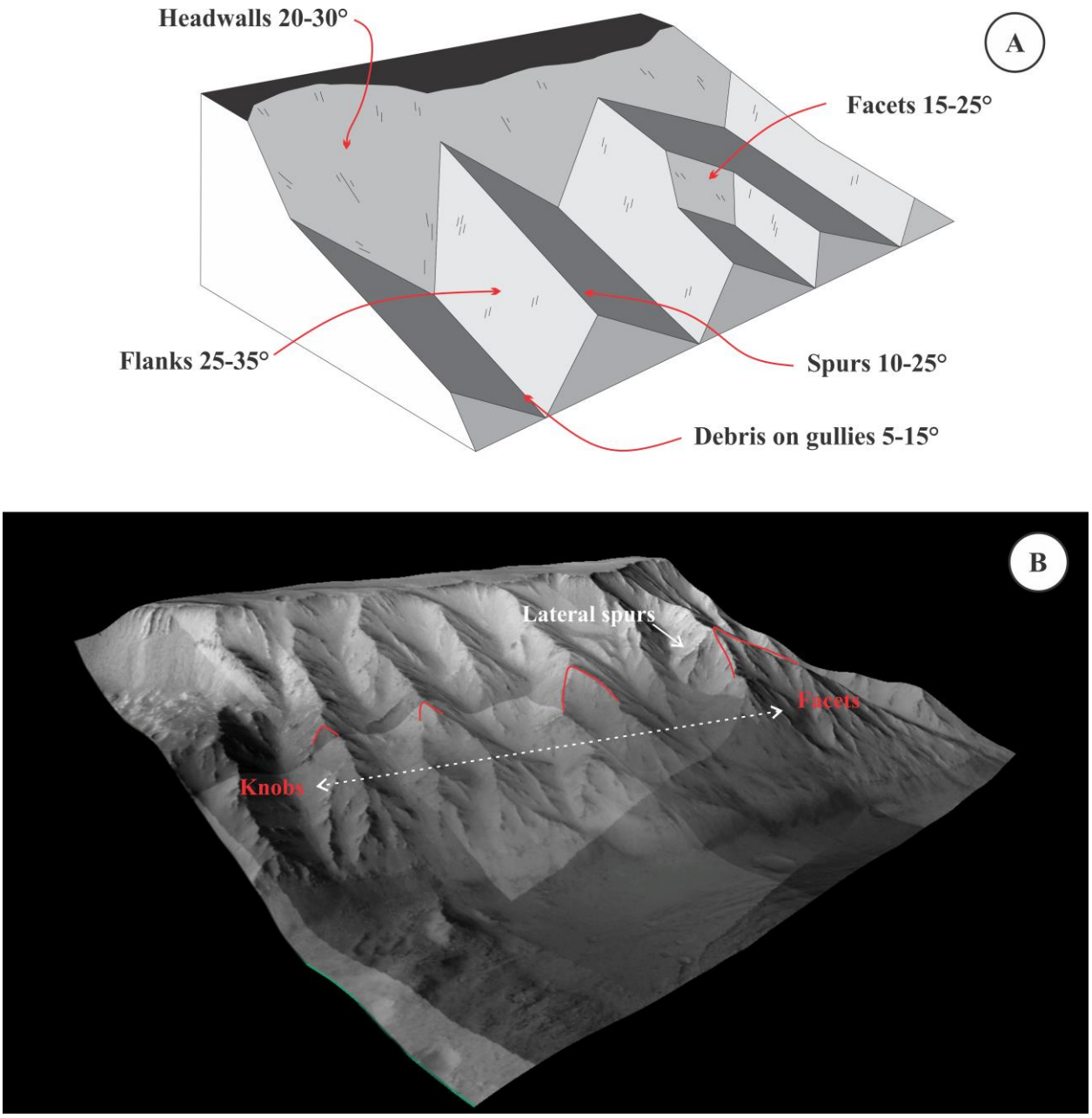

Figure 3-22: (A) Scheme and ranges of plunge/dip values for the elements of the SG wall morphology (B) north wall of Coprates Chasma highlighting the triangular facets and their transition to knobs. 1.5x V.E.

The presence of facets indicates the occurrence of faulting in the walls, yet when faulting occurs with small displacements the facets have a smaller size appearing as a small crest along the ridge, here referred to as a knob (Figure 3-22B). The formation of both features indicates a

variation in displacement of faults along the walls. A transition from knob to facet and vice versa appears marked on Figure 3-22B indicating the connection between both features.

The presence of knobs suggests that faulting might have occurred at a smaller scale making the knobs possible indicators of faulting that involved smaller displacements. This suggests that spurs with multiple knobs along their length may have undergone multiple stages of faulting. Scarps associated with these observed features were located on various areas at different elevations.

3.4.2.3. Orientation of spurs

The rake analysis considers that spurs and gullies will form pitching along the wall with an angle of 90 ± 15°, essentially downslope. The analysis uses a color scheme that highlights the rake of the spurs along the walls (Figure 3-23). The analysis confirms that the dominant orientation is approximately 90 ± 15°. This can be observed on Figure 3-23 as a large coverage of white tones on the walls. However, the results show spurs within the SG wall morphology with orientations highly deviated from the downslope angle of 90°.

Deviated spurs have a greater visual impact within distributions located in Coprates Chasma and Candor Chasma (Figure 3-23). These deviated spurs can indicate the location of structural influence revealing the location of underlying structures as seen on Chapter 2 (Figure 3-23).

The orientation of these deviated spurs is associated with the erosion of the walls along pre-existent fault planes. These cases appear similar to the documented extension of a ridge along an underlying fault of a wrinkle ridge on the wall of Melas Chasma [Cole and Andrews-Hanna, 2017] (Figure 3-15 and Figure 3-24D).

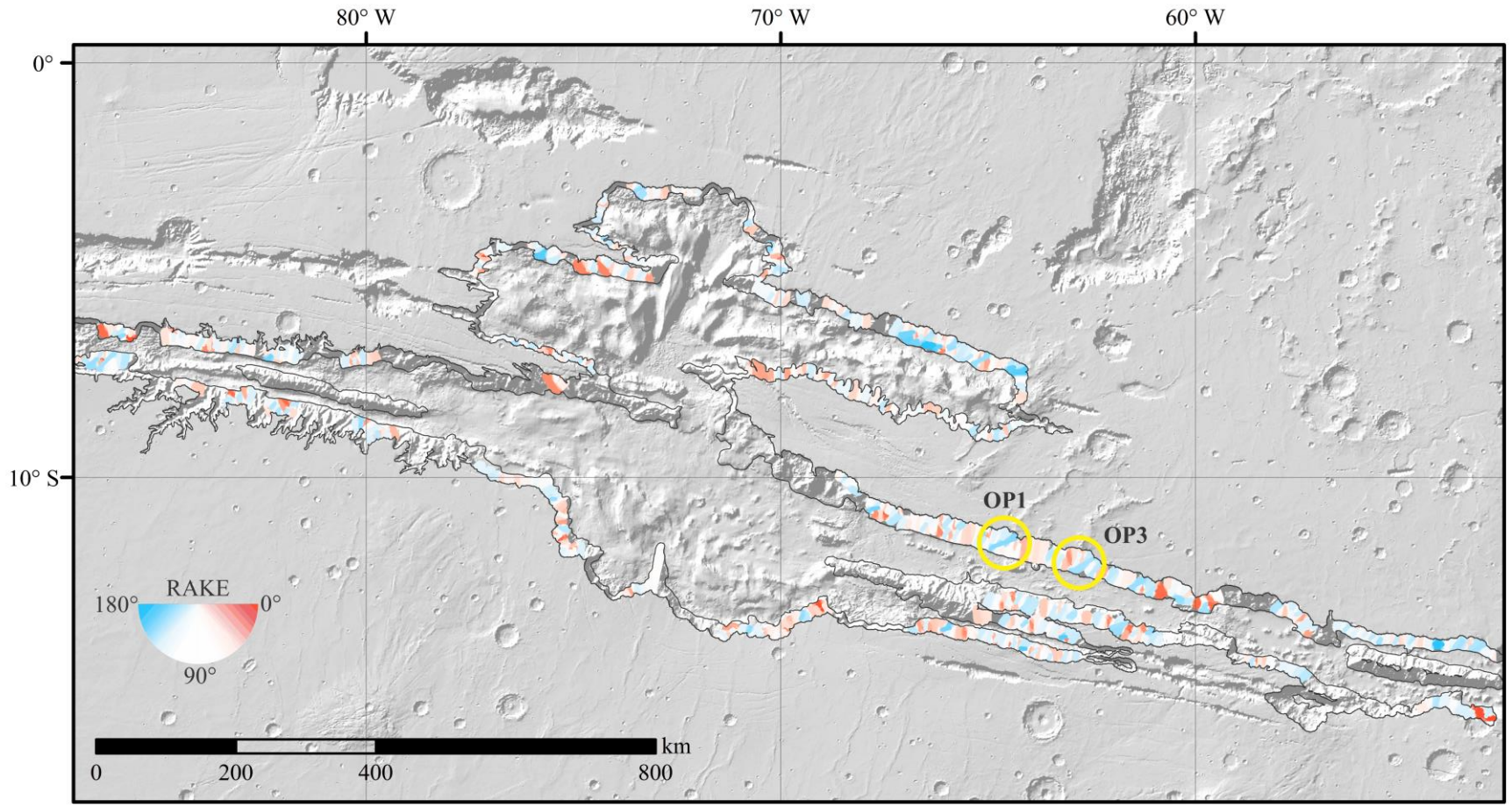

Figure 3-23: Rake analysis results of the SG wall morphology of central Valles Marineris. Yellow circles highlight the APs studied on Chapter 2.

The MSSD results from Ius Chasma, Melas Chasma, and West Candor Chasma show large long spurs associated with the extension of tributary canyons and grabens, suggesting the influence of internal structures in the formation of ridges (Figure 3-24 A-C). These spurs appear pitching along the wall with angles significantly deviated from the downslope angle of 90° which coincides with the results from the rake analysis (Figure 3-24 A-C).

East Candor has disrupted spurs that appear highly deviated, being almost parallel to the strike of its northern wall (Figure 3-25). It has been suggested that this area is structurally controlled [Blasius et al., 1977] and using the AVA analysis it was corroborated that the disrupted pattern is associated with the collapse of the walls (Figure 3-13C). The orientation of these spurs is suggested to be the result of an "ancient" massive collapse of the walls, its relative age inferred from its highly eroded surface and the observed displacement.

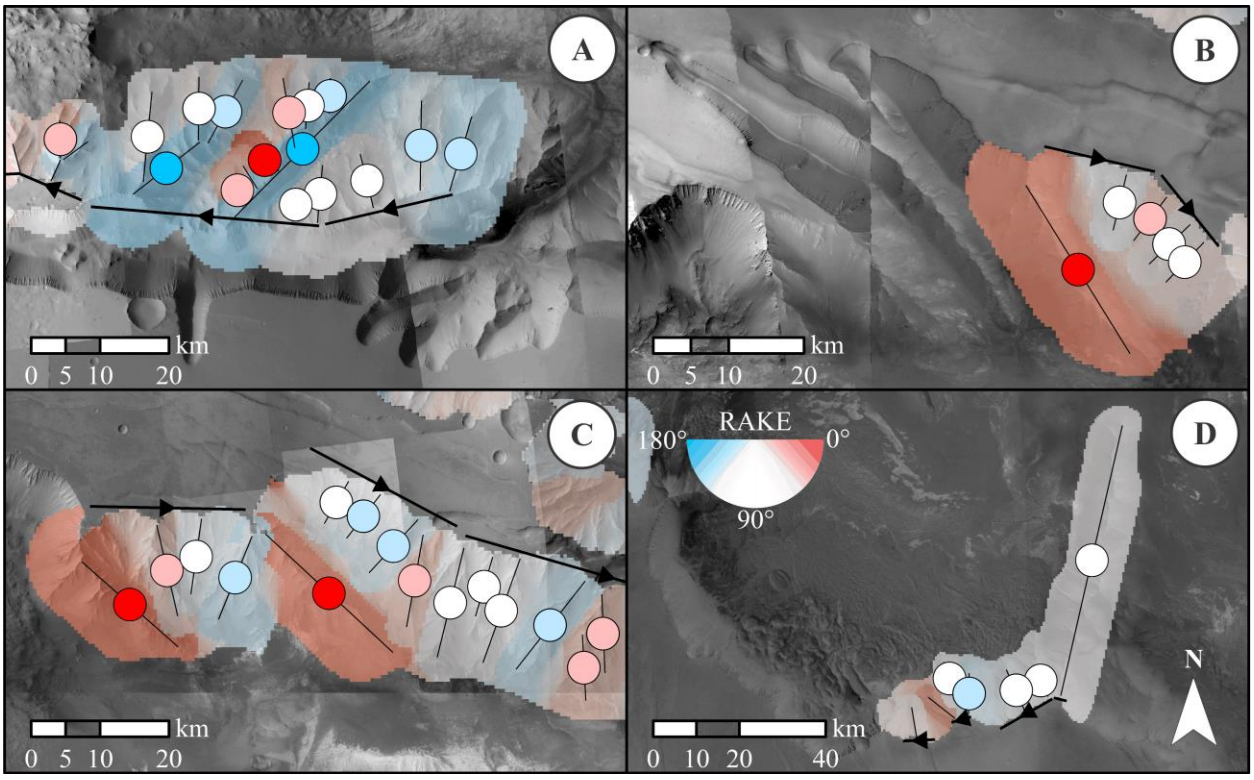

Figure 3-24: Rake analysis of spurs on (A) western Ius Chasma, (B) eastern Ius Chasma (C) West Candor Chasma, and (D) Melas Chasma.

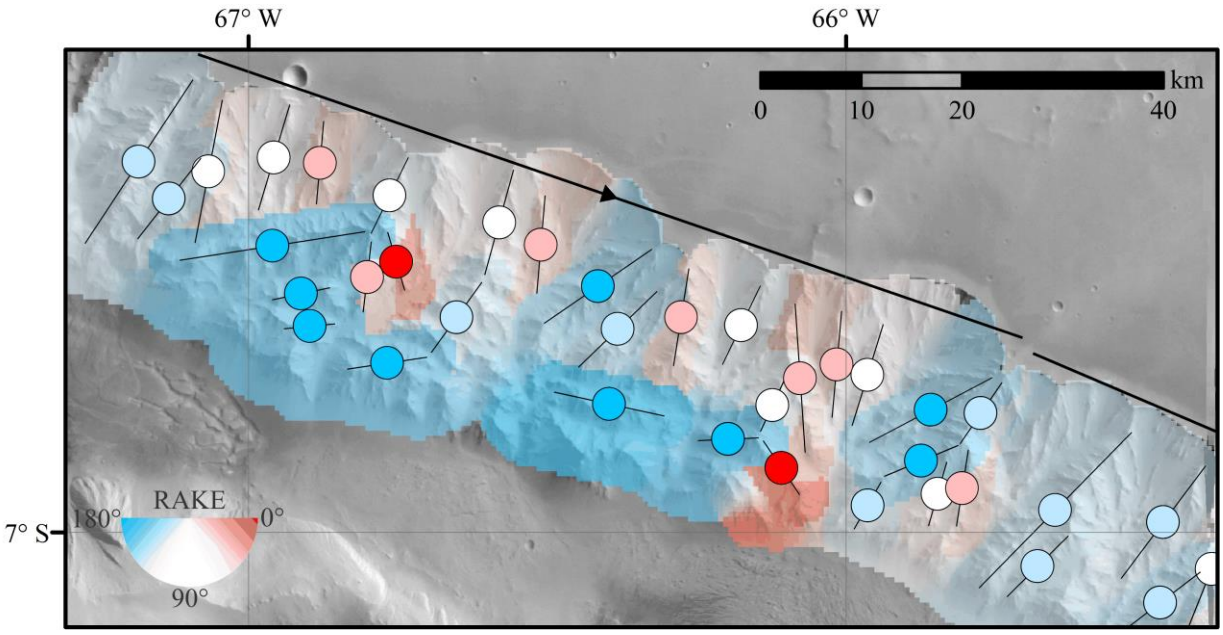

Figure 3-25: Rake results of the north wall of East Candor Chasma showing highly deviated spurs (bright blue areas) associated with a major fault along the wall.

A similar pattern is observed on the northern walls of Coprates Chasma (Figure 3-26) which have been previously classified as the collapse of the wall to produce a fault scarp [Witbeck et al., 1991]. Other spurs with similar orientation appear on the walls of Coprates Chasma suggesting that the formation of spurs is possibly associated with faulting.

Based on previous observations that show difference between facing walls, the rakes of the north and south wall of each chasma were computed into histograms (Figure 3-27). The histograms help to identify any changes in the distribution of spurs on the walls. It appears that Coprates Chasma has a normal distribution of orientation of the spurs on its north walls although two spikes appear remarkably high at ~30° and ~120° (Figure 3-27A). These two orientations are associated with the wall collapse observed on mid Coprates and the presence of the APs, respectively (Figure 3-23). Smaller spikes appear out of the norm for values >140° associated with the fault scarps in eastern Coprates (blue field in Figure 3-27A).

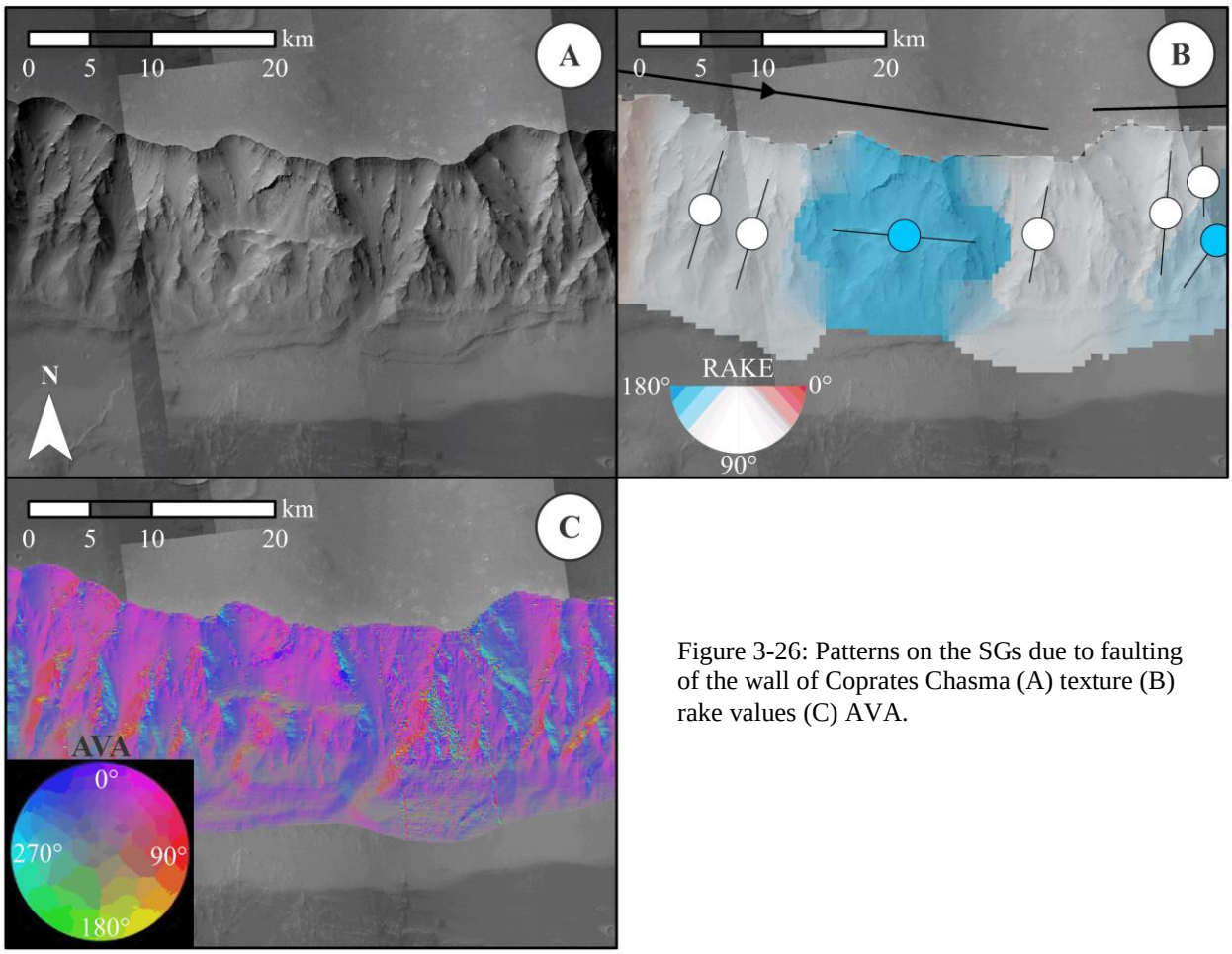

Figure 3-26: Patterns on the SGs due to faulting of the wall of Coprates Chasma (A) texture (B) rake values (C) AVA.

The south walls of Coprates have many spikes; one of them has an orientation of ~110° indicating a pitch towards east on these walls. The spurs on the north walls have a slight preference to deviate towards the west while the ones on the south wall deviate in the opposite direction (Figure 3-27 A-B).

Candor Chasma has a distribution where most spurs appear to pitch downslope within the expected range. A spike at ~155° appears on the distribution, this one is associated with the area of the northern wall that was suggested to involve collapse (Figure 3-27C). Observation of the distribution and the rake map (Figure 3-23) shows that several spurs pitch towards west on both north and south wall (Figure 3-27 C-D). The east end of the chasma appear to have orientations possibly associated with a cross fault due their location (Figure 3-23).

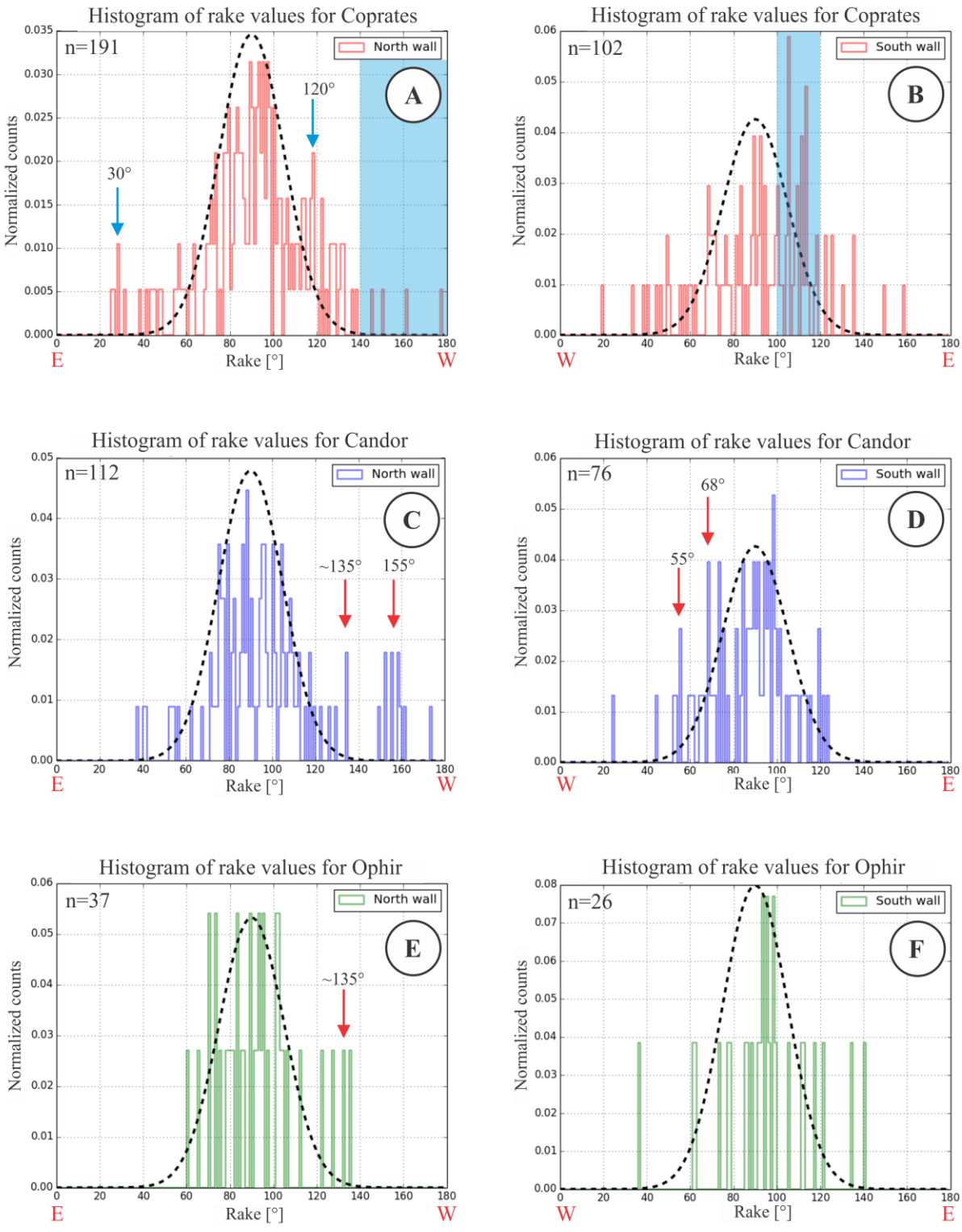

Figure 3-27: Histograms of rake values for each chasma compared with a normal distribution that uses a mean of 90° and a deviation of 15°. The peak of the normal distribution matches the peak at 90° for each facing wall of each chasma. Arrows (blue and red) highlight relevant rakes out of the norm. The chasmata are (A-B) Coprates Chasma, blue areas highlight intervals of interest for this chasma, (C-D) Candor Chasma, (E-F) Ophir Chasma.

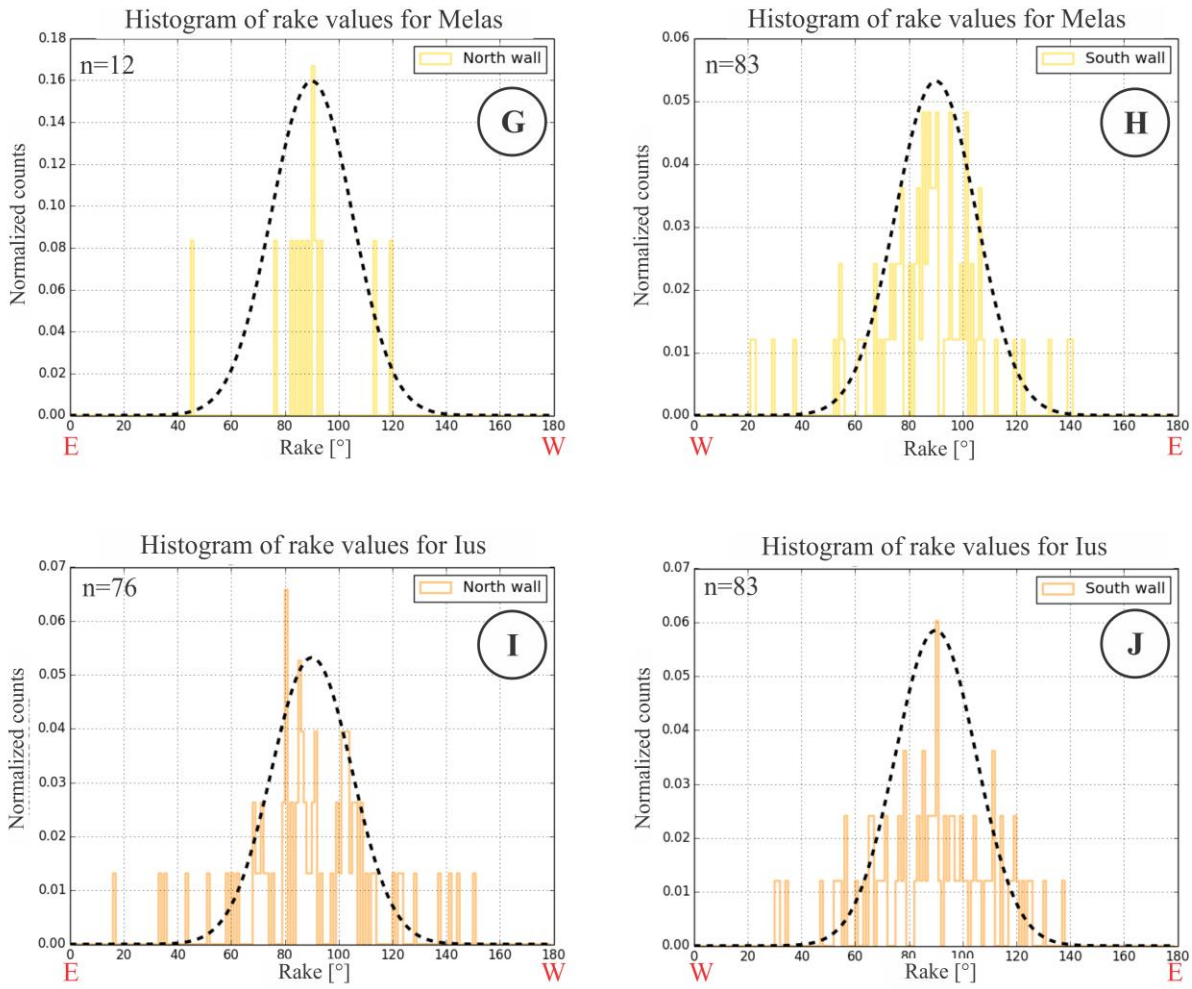

Figure 3-27: (G-H) Melas Chasma, and (I-J) Ius Chasma.

Ophir Chasma and Melas Chasma have small populations of spurs compared to the other chasmata, based not only on the dimensions of the chasmata but also with the number of landslides located on their walls (Figure 3-1). The spurs on these chasmata have a spread distribution within the expected orientation of downslope spurs (Figure 3-27 E-H). The spreading is possibly related to the various attitudes of the walls altered the relative orientation of spurs. Several spurs within the walls of Ius Chasma are considered to be influenced by the structures observed on the plateau such as grabens. This is seen in the histograms of the orientation of its spurs; the spikes in the distributions are associated with the orientations of the grabens (Figure 3-27 I&J).

3.5. Discussion

3.5.1. Analysis of the walls

The results of the analyses of the SG wall morphology show that the orientation of the spurs is dominantly downslope plunging with angles of 10-20°. These values are lower than the resulting values from the dip analysis of the walls and the LTS analysis that are ~24° and 21 ± 3° respectively. These results were compared to RMR values from Schultz [2002] indicating that the measured walls of central Valles Marineris have reached stable slopes. The measured section of walls indicate that the SG wallslope is 16-28° (Figure 3-21A) which is within the range of the martian repose angle. The LTS results suggest that most of the walls of central Valles Marineris have similar dips, yet there is a slight difference of ~2° for Ius Chasma and Coprates Chasma, having lower dips than the other chasmata. This might be associated with the multiple faulting involved in their formation of both chasmata as inferred from their rectangular shape and the observed faults along their length.

The range of wallslopes appears to be greater for Coprates Chasma on the LTS results (Figure 3-20). Notably, not only the height of the walls but also the spurs on Coprates walls decrease in length from western Coprates to eastern Coprates. This could indicate a possible formation in stages for Coprates Chasma. This concept is suggested based on the results of the MSSD, AVA, LTS, and rake analyses which show a marked difference between western and eastern Coprates Chasma (Figure 3-11D, Figure 3-15, and Figure 3-23) and will be explored in the next chapter. The decrease cannot be the result of sediment infilling the floor since larger deposits are observed on western Coprates, which would infer that that region should have shorter wallslopes.

3.5.2. Indicators of structural influence

As inferred in Chapter 2 and previous studies [Blasius et al., 1977; Lucchitta, 1978; Peulvast et al., 2001; Cole and Andrews-Hanna, 2017], structural influence can be found within the walls. This study shows how the geometry of the SG wall morphology has been structurally influenced. Structural influence has been proven to affect the orientation of the spurs as they deviate from their expected downslope direction. The direction of spurs along the walls is considered dominant within the range of 90 ± 15° as seen on the results of the rake analysis (Figure 3-23). However, within the rake distribution of each chasmata, deviated orientations appear highlighted as they are far from the norm (Figure 3-27). These orientations are associated with most of the spurs that have higher curvature values on the MSSD results (Figure 3-11). They also have pronounced relief and greater lengths than other spurs within the walls. Examples of these are noticed within the walls of Candor Chasma where it appears that spurs trend more towards west on both facing walls of the chasma (Figure 3-27 C&D). This deviation observed on both walls could be associated with the collapse of the chasma.

The MSSD, AVA, and rake analysis demonstrate that chasmata with rectangular shape are those where the presence of structural influence is more notable on their walls, as it appears that these chasmata interact subparallel to the grabens, and sub-perpendicular to the wrinkle ridges observed on the Tharsis province (Figure 3-11, Figure 3-15, and Figure 3-23). The AVA results indicate the location of 24 APs within the walls of central Valles Marineris where many of them appear within the rectangular shape chasmata (Figure 3-15 and Figure 3-23). The APs are the representation of structures in the interior of the Tharsis that expressed on the walls as planar features with anomalous attitudes [Chapter 2] working as indicators of structural influence.

Other indicators of structural influence where found using MSSD results that show that large long spurs can be indicators as well. Additionally, other indicators are observed within the wall that is the case of the small spurs on flanks, and knobs. The knobs are similar to facets associating them with faulting with smaller displacement (Table 3-1).

Table 3-1: Indicators of Structural Influence

	Fault association	Process involved	Attitude	Involved structure	Shape	Size	Secondary feature
Fault Scarps	Chasma producing faults	Collapse	Parallel to wall		Linear	km Scale	
Facets	Chasma producing faults	Fault displacement	Parallel to wall		Triangular surface	2-5 km	
Knobs	Chasma producing faults	Fault displacement	Parallel to wall		Crest with lateral spurs	< 2km	
Secondary spurs	Chasma producing faults	Wall retreat /Collapse	Parallel to Fault	Grabens	Linear	~2 km	
Long narrow spurs	Pre-existing faults	Erosion	Along involved structure	Grabens	Linear	km scale	Spurs parallel to dip of fault Facets
				Wrinkle ridges	Linear		
Anomalous planes	Pre-existing faults	Erosion	Dips into wall	Wrinkle ridges[1]	Curved surfaces	km scale	
				Cross faults	Planar surfaces		

[1] Could involve other structures

The formation and morphology of the spurs is not only affected by fault planes as it is possible that the size of the walls and local conditions of erosional processes might have influenced as well. Well-defined and highly pronounced spurs are observed to have formed within areas of the chasmata with greater walls (i.e. greater lengths of slopes) such as western Coprates Chasma (Figure 3-11D).

3.5.3. Relative orientation of the walls and interior faults

The large long spurs are the result of erosion along fault planes of grabens or wrinkle ridges that cross the walls (Figure 3-28). The fault planes are considered to extend into the wall and into the Tharsis province. However, not many of these structures have a topographic surface expression [Schultz et al., 2007; Cole and Andrews-Hanna, 2017; Chapter 2]. The spurs are influenced by the fault planes eroding in different forms, sizes, and orientations. These planes influenced the formation of the spurs and the shape of the spurs is dependent on the horizontal angle between the fault planes and the walls of the chasmata.

The following relationships between fault to wall angle and the developing structure are suggested:

(1) If the angle between the fault plane and the wall is small, the wall will erode onto the fault plane regardless of whether the fault was formed by extension or compression. The wall will erode and become the flank of the ridge/spur using the fault plane as a base for its formation. The erosion alters the original attitudes of the wall and the fault planes making it difficult to obtain such values.

(2) If the wall is crossed by a fault system, the orientation of the faults will form a different morphology such as a channel or a ridge (Figure 3-28). This case appears at various locations of the walls where channels formed along grabens and scarps. Features associated with

this type of influence are observed on chasmata such as Ius Chasma, West Candor Chasma, and Melas Chasma where major faults cut through the walls of the chasmata (Figure 3-15). These faults appear to be deeply rooted as inferred from a possible connection at the breach between Ophir Chasma and Candor Chasma [Mege and Bourgeois, 2011].

The reasons for the differences between these cases are not fully understand yet. The angle between the walls of the chasma and the fault planes of pre-existing structures is not the only factor involved in the formation of structural influence indicators. The lithology and environment of the region might affect as well the exposure of the pre-existing faults exposed on the walls.

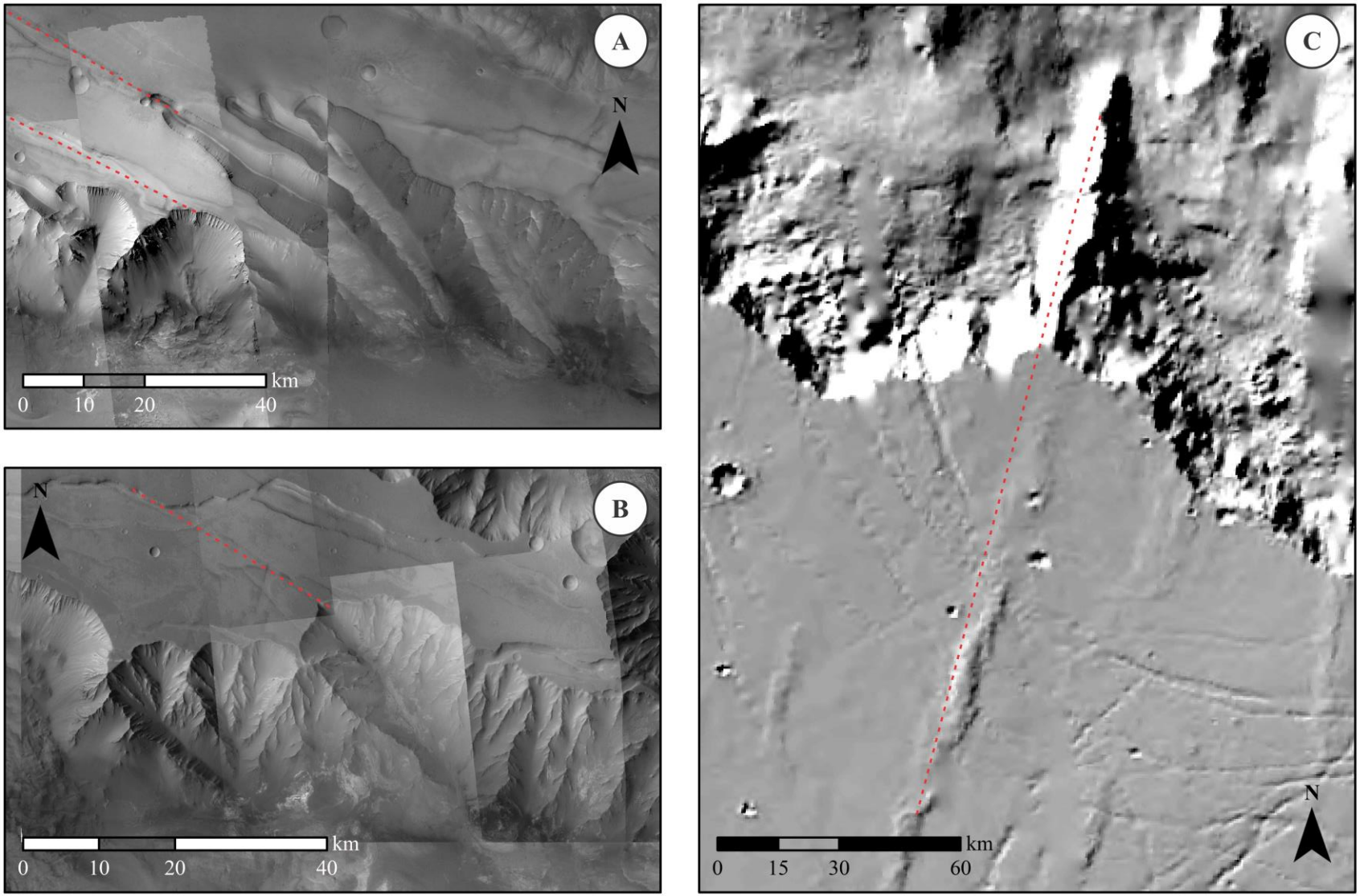

Figure 3-28: Intersection between fault planes and walls forming (A) tributary canyons (B) SGs (C) large long ridges.

3.6. Conclusions

Comparison of the applied methodologies shows that the spur and gully wall morphology can be structurally influenced in many forms including previously suggested ones [Blasius et al., 1977; Lucchitta, 1978; Peulvast et al., 2001; Cole and Andrews-Hanna 2017]. The geometry of certain features on the walls can be linked to faults within the Tharsis province. These geometries were recognized and classified as indicators of structural influence.

The suggested indicators of structural influence are associated with the orientation of the ridges/spurs on the walls. Large long ridges extending along the walls suggest the presence of structural influence where grabens facilitated the formation of tributary canyons. The graben becomes a channel while the faults associated with the structure led to the formation of ridges along the fault planes. Other large long ridges that formed planes with anomalous attitude are also indicators of the presence of faults. These cases show that the pre-existing faults planes work as a strong base for the formation of flanks eroded on the walls.

Further study might include new alternatives to determine structural influence. The presented methods demonstrate that they can be used to determine the effects of the influence of faults within the Tharsis on the walls of central Valles Marineris.

Chapter 4 : Special isolated cases of structural influence

The previous chapter presented a detailed analysis of structural influence on the spur and gully (SG) wall morphology of central Valles Marineris. The results suggest possible indicators of the influence of chasma-producing faults [Chapter 3] and pre-existing faults within the Tharsis bulge [Chapter 2 & 3]. In this chapter, special isolated cases explore the use of these indicators to determine the origin of formations located within the walls in an attempt to connect them to visible structures on the surrounding plateau. The use of previous methodologies such as dip analysis, Mean Signed Square Difference (MSSD), and Augmented Visualization of Attitude (AVA) are required to identify the indicators of structural influence.

4.1. Comparison of different types of V- shaped channels within the walls

This section compares the morphology of two different shapes of channels within the walls of central Valles Marineris. The comparison is made between the tributary canyons observed at the west end of Ius Chasma (Figure 4-1B) and a channel located near the north and east wall of Candor Chasma (Figure 4-1A).

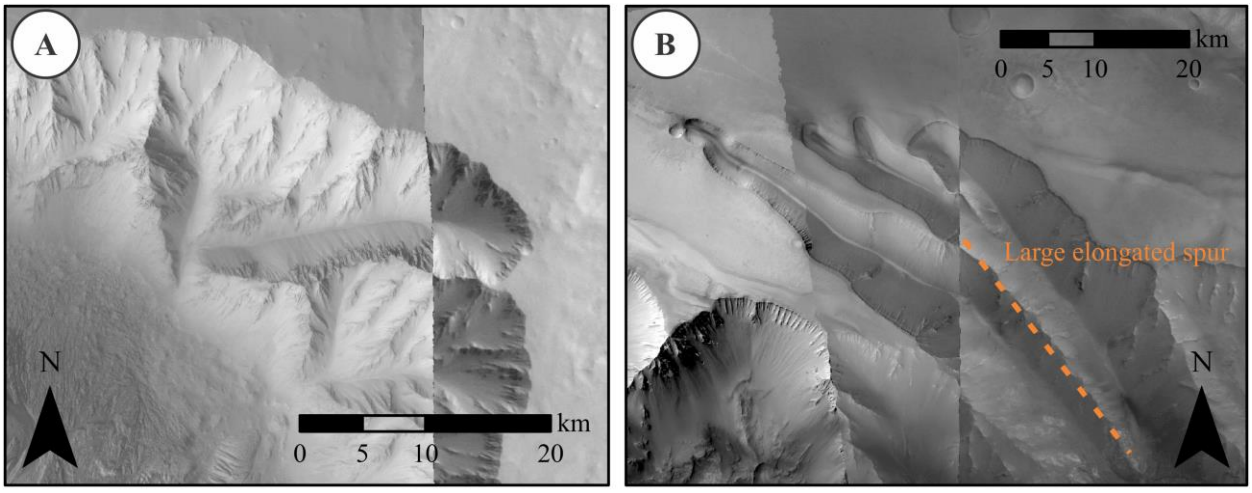

Figure 4-1: (A) Channel within East Candor Chasma and (B) tributary canyons at western Ius Chasma shown using a mosaic of High Resolution Stereo Camera (HRSC) and Context Imager (CTX) imagery.

The tributary channels at Ius Chasma were suggested to have formed over grabens that cross the wall of the chasma [Chapter 3]. This connection was suggested due the presence of large long spurs (Figure 4-1B). In Chapter 3, it was proposed that these spurs formed along the fault planes of the grabens.

The channel in Candor Chasma was identified using the AVA analysis where an Anomalous Plane (AP) appears on the wall of the chasma as part of the channel. The observed AP and a fault scarp on the north wall form the channel. The fault scarp extends from the mid-section of the north wall of East Candor towards the east wall trending parallel to the wall chasma (Figure 4-2A).

The AP dips into the north wall of the chasma (Figure 4-2B). The north side of the channel is possibly associated with the extensive fault observed on the north wall of the chasma as both have similar trend with facing dip directions. Both planes appear to have a perfectly planar surface towards their upper section merging with the headwall (Figure 4-2C).

Inspection of the surface of the north-facing wall of the channel suggests that this one formed by the extensive fault on that wall of the chasma. This is confirmed by the presence of coarse ribs at the top of the plane (Figure 4-2C). Such ribs are the expression of the exposed bedrock due the collapse [Lucchitta, 1978].

Dip analysis shows that the walls of the channel have consistently relative steep dips of 30-40° (Figure 4-3A). This range corresponds to a resistant wall-slope [Schultz, 2002] and in cross-section the planar walls form a V-channel (Figure 4-3 C&E).

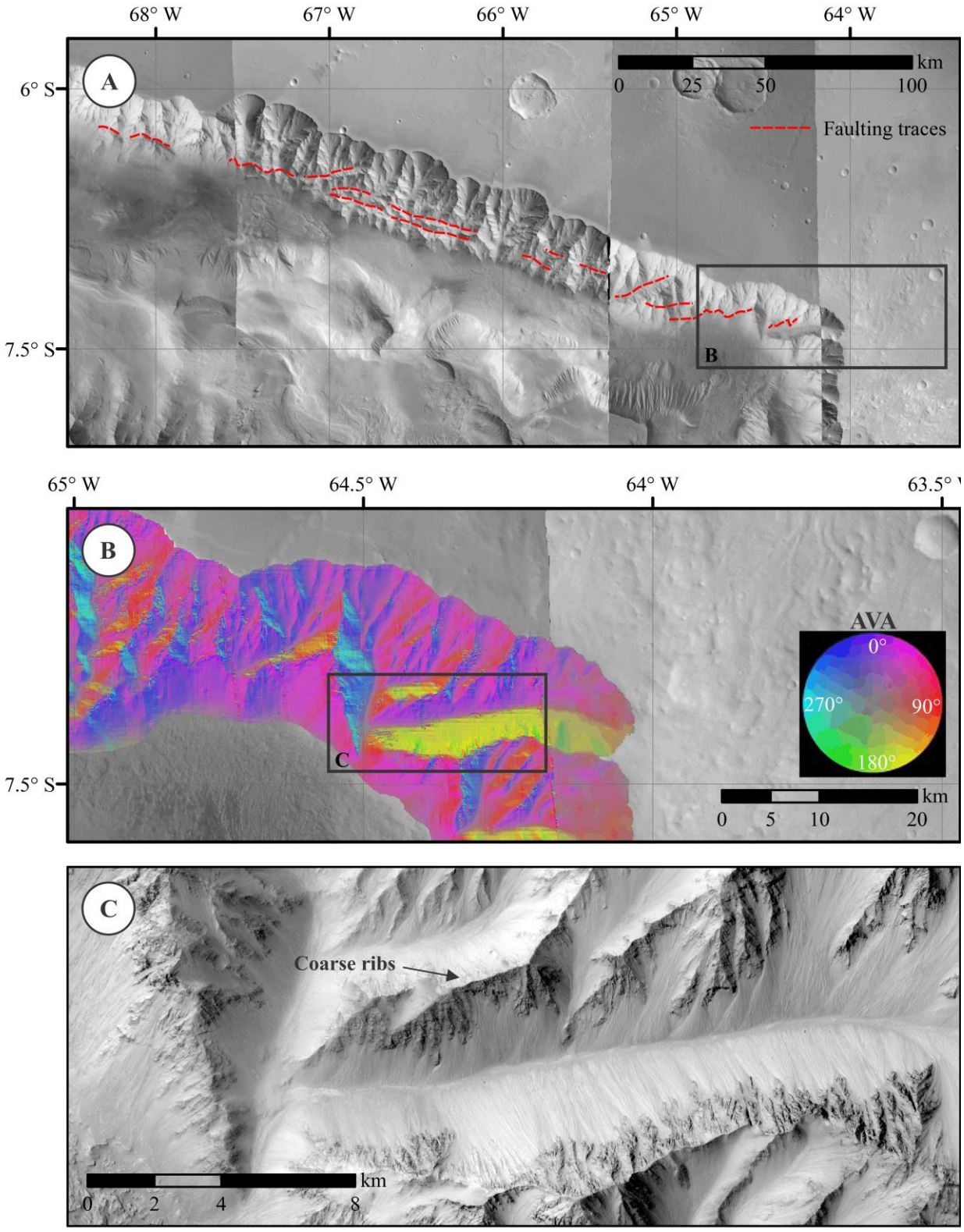

Figure 4-2: (A) Fault scarp along the northern walls of East Candor Chasma (B) AP between the north and east wall of East Candor Chasma visible with the Augmented Visualization of Attitude (AVA) color-scheme (C) texture of the plane shown using CTX imagery, resolution ~5 m/px.

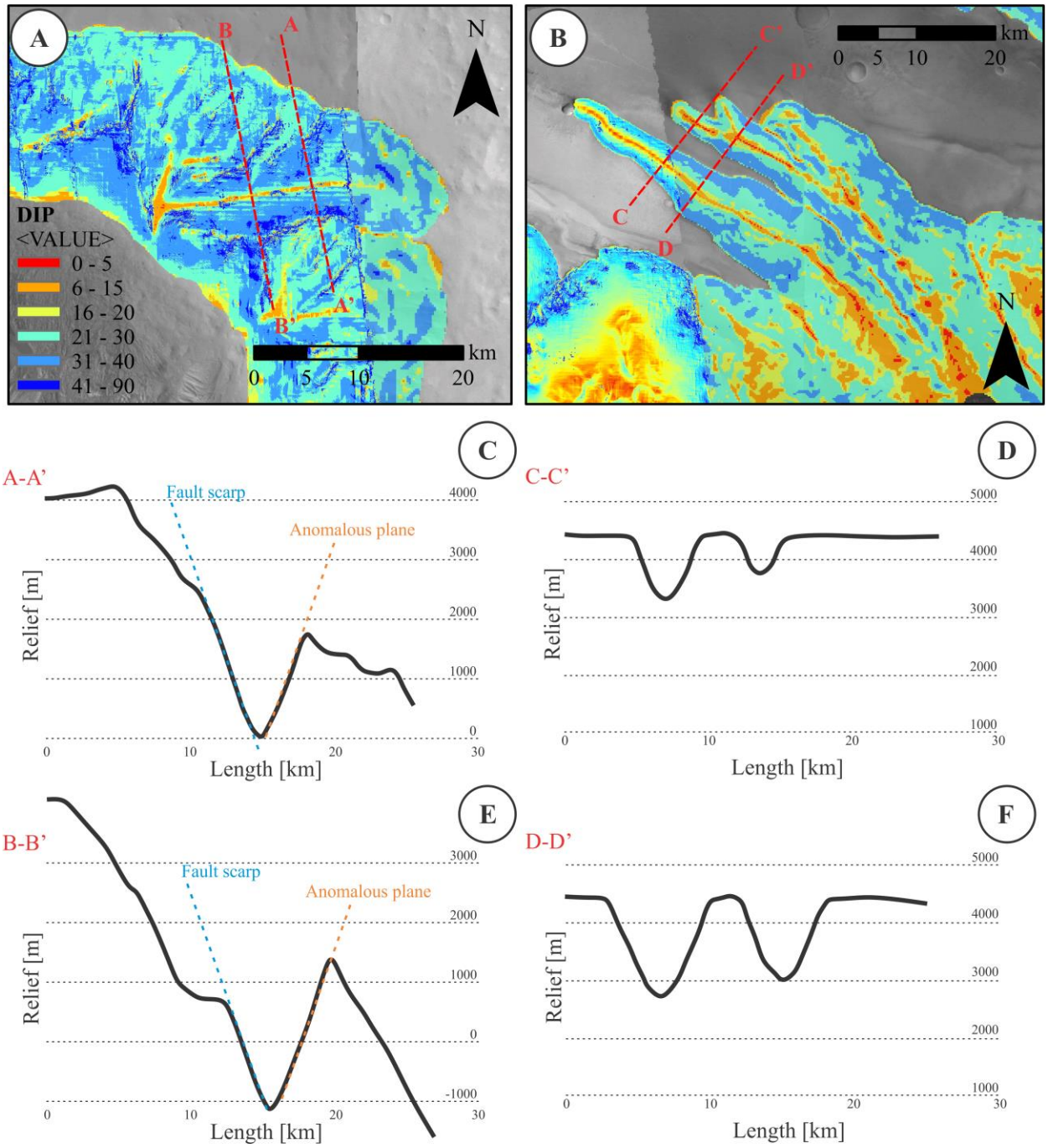

Figure 4-3: Comparison of the dip of the walls of the (A) V-shaped channel at East Candor Chasma, and (B) tributary canyons at Ius Chasma. (C-F) profiles of the channels, 2x V.E., of (C,E) East Candor Chasma and (D,F) Ius Chasma. Here it is compared the geometry of the walls of both channels.

By contrast, the slopes of tributary canyons in Ius Chasma are slightly shallower than the V-shaped channel (Figure 4-3 A&B). Tributary canyons have their steepest values at the upper part of their walls (Figure 4-3B), thus forming a U shape [Laity and Malin, 1985; Howard, 1987]. Two profiles across the tributary canyons show how their shapes remain the same along its extension until they form the large long spurs (Figure 4-3 D&F). Similarly the V-shaped channel maintains a consistent shape along its entire extent (Figure 4-3 A,C,&E). It is considered that both formations have defined shapes, making difficult a possible transition between them.

Topographic measurements along the base of the V-shaped determined that the channel has an attitude of ~263/09, while measurements along the base of tributary canyons have shallower intersections with plunges of ~5° (Figure 4-3 A&B). Both types of channels are considered to have formed along underlying structures that influenced their morphology. For example, the tributary canyons extend linearly following the orientation of the grabens visible on the plateau while the V-shaped channel has one wall formed by the extensive fault along the north wall of East Candor.

Both channels are thought to have formed under fluvial conditions, the tributary canyons have a U-shape that is associated with melting of ice that breaks through the bedrock as groundwater [Laity and Malin, 1985; Howard, 1987]. The association of tributary canyons at Ius chasma with grabens visible on the plateau indicates that the grabens facilitated the formation of the tributaries. Nonetheless, the morphology and associated structures of both channels mark clear differences in their type of formation. The V-shaped channel is proposed to have formed by the fault scarp and the AP having competent and planar walls. The exposure of these planar surfaces involves the erosion of the bedrock that reveal the underlying planar structures (Figure 4-2C and Figure 4-4).

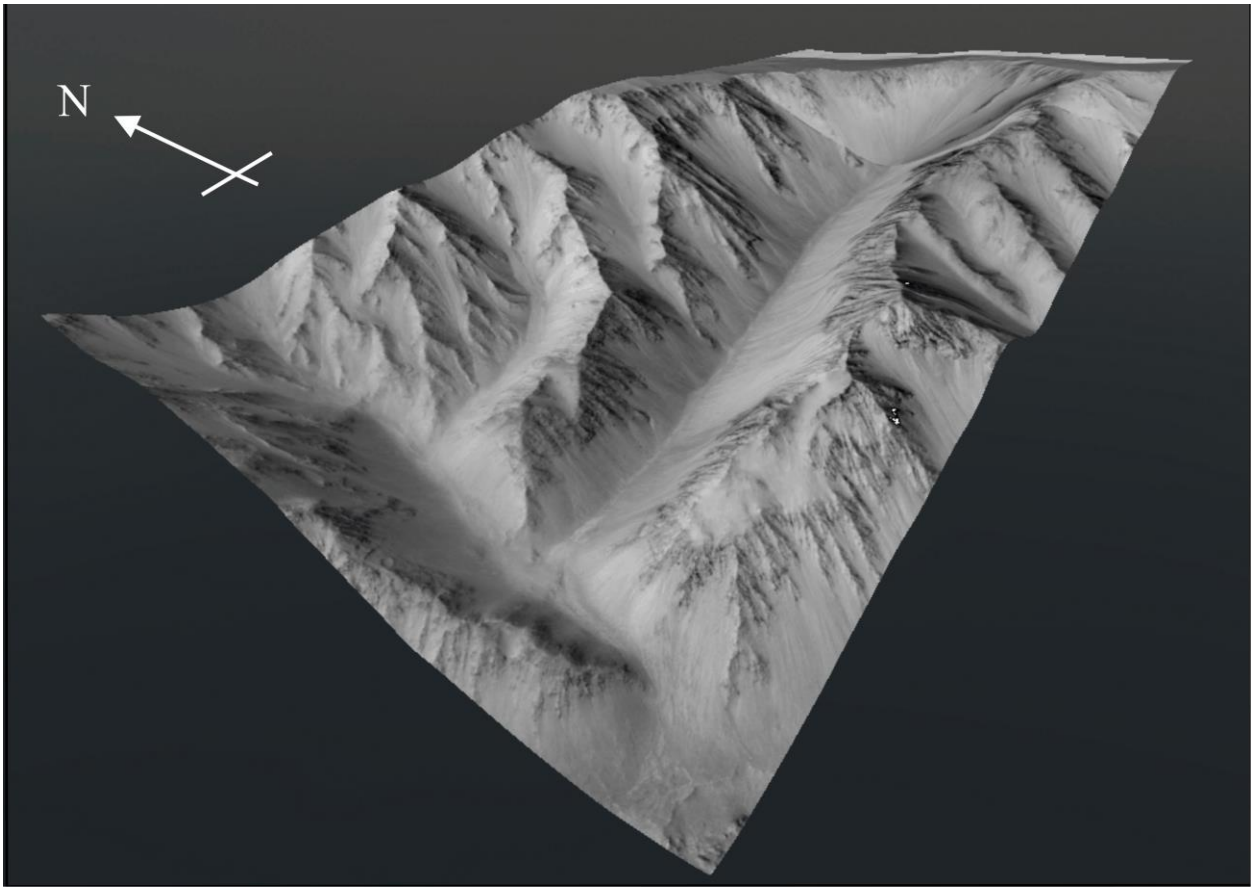

Figure 4-4: 3D projection of Figure 4-2C visualizing the V-shape channel formed by the fault scarp and the anomalous plane. 2x Vertical Exaggeration (V.E.).

It is proposed that both channels involve structural influence although they expressed differently due to differences in their underlying structures. The structural influence near the tributaries is observed close to the end of their extent where the large long ridges start (Figure 4-1B). This is noticed by the change in texture and aspect of the surface, going from a smooth surface covered by talus to a rougher surface that includes small crests (Figure 4-1B). The structural influence on the V-shaped channel is notably expressed on its walls. Yet the lack of visible traces of structures on the surrounding plateau limits the interpretation of the origin of the AP.

4.2. Hourglass graben

Structural influence expresses on the spur and gully wall morphology as the result of the interaction between the walls and structures such as faults from grabens or wrinkle ridges. The influence becomes visible on the walls as eroded wall morphology form geometric traces of the underlying structures on the walls [Chapter 3]. An example of this appears along the extension of the late Hesperian grabens located on Ophir Planum [Schultz, 1989; Hauber et al., 2010] that cross the walls of East Candor Chasma (Figure 4-5). They affected the morphology of the wall forming large long ridges extending along the fault planes (Figure 4-5). These spurs are relatively long and continuous ridges compared with those examined on the neighbouring walls. Since the termination of the grabens appears to coincide with the uppermost end of spurs, the connection between these features and the grabens was analyzed.

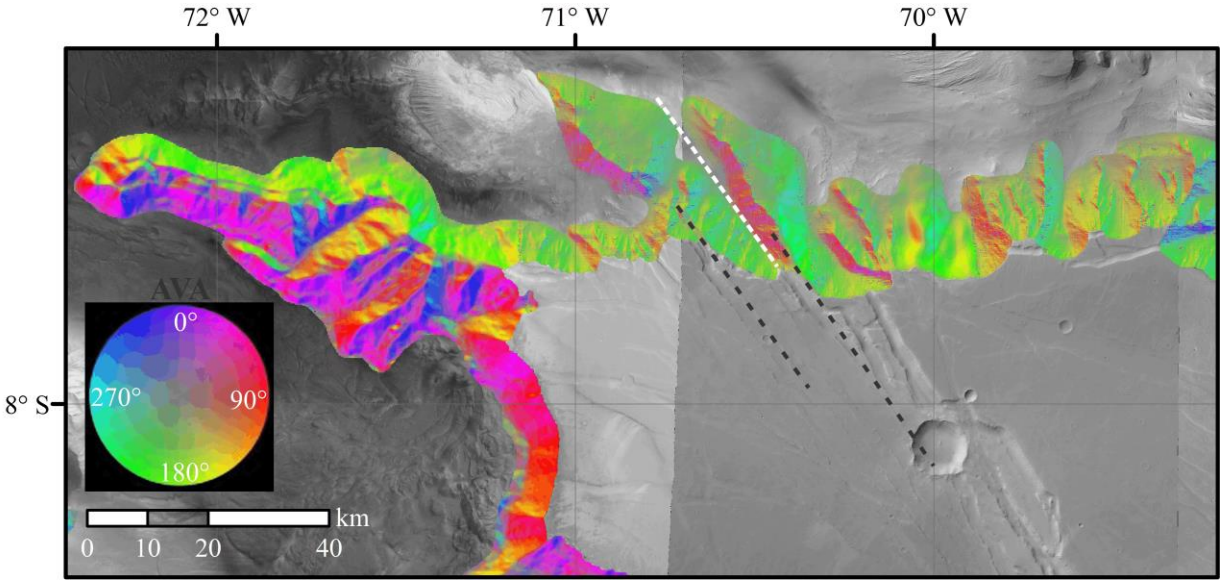

Figure 4-5: Grabens crossing the walls of East Candor Chasma; dashed lines show the orientation of both SGs and the grabens, ~300°.

Inspection of the intersection of the graben and the wall of East Candor Chasma indicates that the graben extend into the chasma, expressing on the walls. The fault planes cut through the walls to form the flanks of the spurs. Similarly, the ramp of the graben led to the formation of the gully between the long ridges, given their similar orientation (Figure 4-6A). In this case, one fault plane merges with a section of the southwest wall of the chasma and the other forms the flank of a long spur (Figure 4-6A). The flank of the spur aligns with the fault plane of the graben while the southwest wall eroded and widened, acquiring a shallower attitude compared to its associated fault plane (Figure 4-6A).

Grabens within this area could have had steeper attitudes when they formed [Schultz, 1989; Hauber et al., 2010]. However, the slope of the walls of the graben appears to decrease downslope due the erosion of the walls that infill the interior of the structure adhering to the walls (Figure 4-6B). This suggests that the erosional processes may affect the appearance of the floor enhancing the slope of the floor to a current dip of ~16° SW (Figure 4-6B), producing the asymmetry of graben. The morphology of the graben suggests it is an hourglass-shaped graben [Schultz et al., 2000; Schultz et al., 2007] (Figure 4-6C). This type of grabens is considered to form by thick-skinned tectonics [Schultz et al., 2007] as the faults cut through diverse lithology.

The connection between the faults of the graben and the eroded planes along the wall and the spur was corroborated by comparing the attitudes of the walls of the graben, the flank of the long spur, and the section of the walls (Figure 4-7). The attitudes of the walls of the graben are 325/25 and 147/25 for both the southwest and the northeast wall respectively (Figure 4-7A) being slightly shallower than the attitude of the flank of the long spur and the southwest wall that are 165/28 and 312/31 respectively (Figure 4-7B).

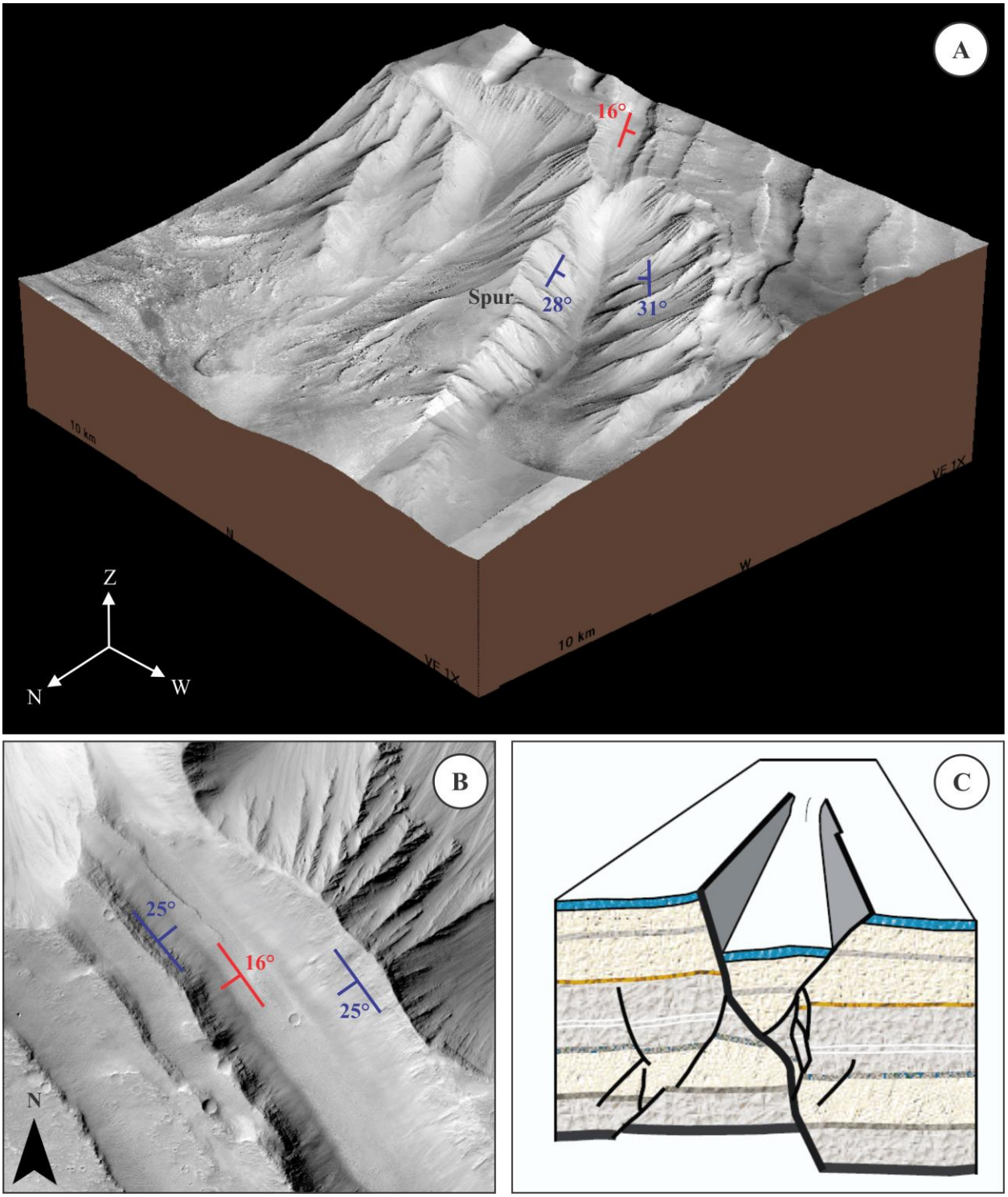

Figure 4-6: Graben crossing the south wall of East Candor Chasma (A) 3D projection (B) close-up of the tilted filled floor (C) hourglass graben model, modified from Schultz et al. [2000].

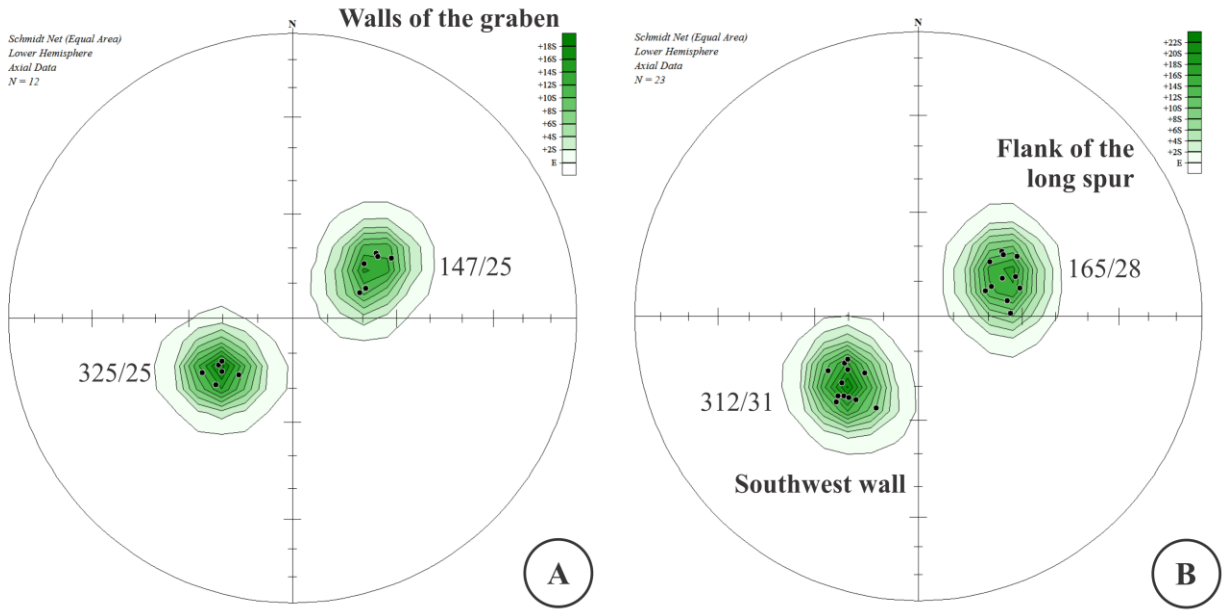

Figure 4-7: Stereonet with measured attitudes of the pole-to-plane for the (A) walls of the graben (B) flank of the long spur and section of the wall of the chasma.

The results are within a similar range of attitudes, agreeing with the suggested widening of the space between the fault planes. This is observed when comparing the attitude of the walls of the graben with the respective aligned walls of the chasma (i.e. flank of the long spur and section of the walls or southwest wall). The comparison shows that the flank of the spur changes in strike of ~5° greater than the one observed for the southwest wall (Figure 4-7). This is related to the shape of the spur since as it narrows away from the chasma wall (Figure 4-6A).

A schematic model of the graben extending over the wall of East Candor Chasma shows the connection between the observations (Figure 4-8). The model considers the possible hourglass shape for the graben extending over the walls and showing how the ridges formed over the walls as an expression of the fault planes of the graben developing by adjusting the topography during the erosion of the walls (Figure 4-8B). Secondary spurs formed downslope on the flank of the long spurs and the southwest wall (Figure 4-8B). Along these secondary spurs, facets and knobs infer wall retreat associated with fault scarps nucleated by the faults parallel to main graben (Figure 4-6 A&B). The orientation of these facets and knobs coincide with the trend of the grabens (Figure 4-8B).

The fault planes of the graben are traced to indicate that their development goes to greater depths (Figure 4-8B). A possible intersection is included since hourglass grabens can extend through various geological units (Figure 4-8B).

The case shows how possible pre-existing faults are involved in the formation of large long spurs. It is proposed that later faulting modified the wall morphology of a chasma with a different attitude due to changing structural influence.

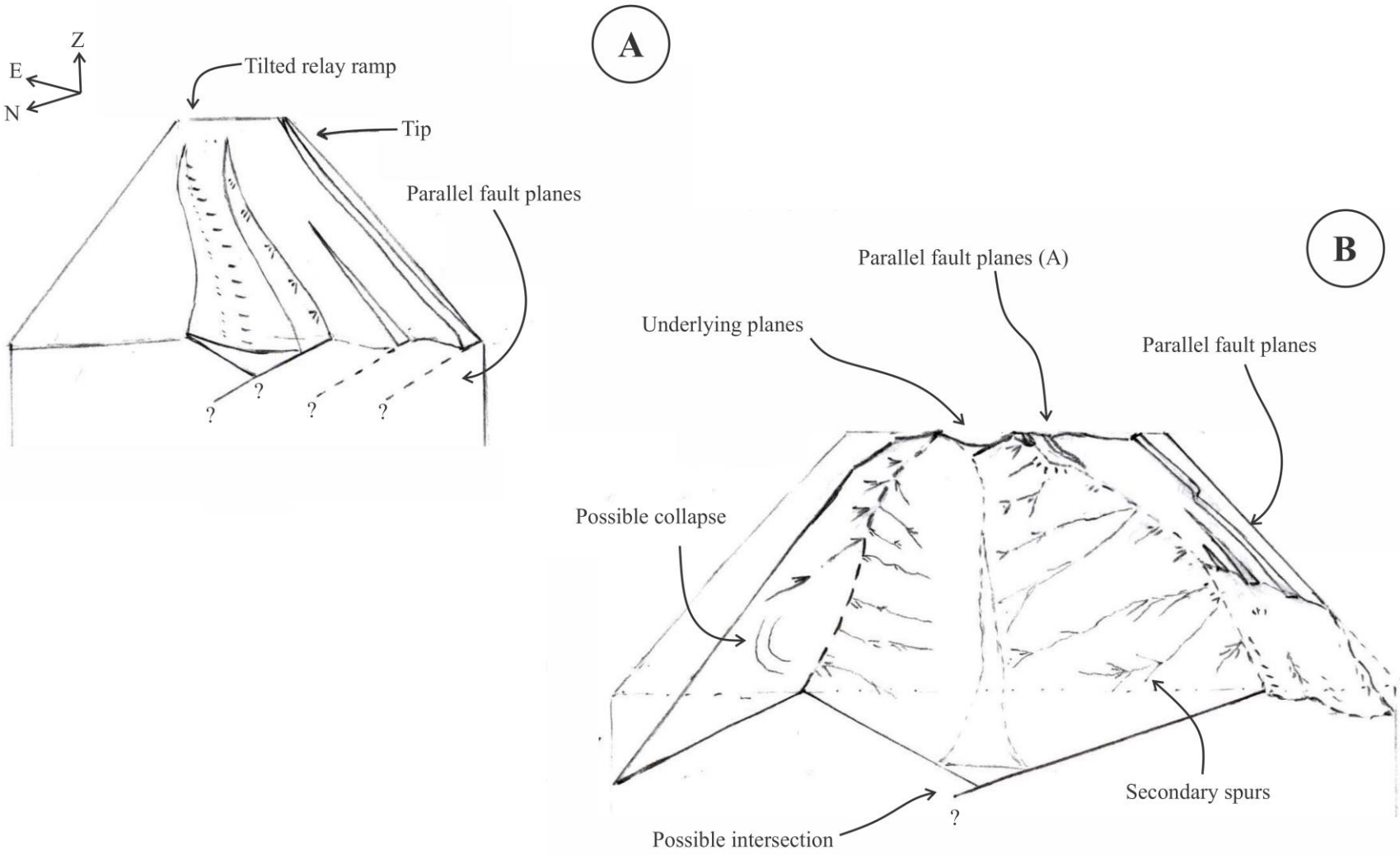

Figure 4-8: Schematic model of the graben extending over the wall of East Candor Chasma: (A) illustration of the asymmetry including the underlying northeast dipping faults and parallel fault planes (B) SG wall morphology showing the extension of the graben and the parallel planes at the plateau.

4.3. Segmented formation of Coprates Chasma

It has been suggested that Coprates Chasma is the result of volcano-tectonism that involved extensional processes and subsidence [Schultz, 1991; Andrews-Hanna, 2012]. This long chasma has a rectangular shape, narrowing towards the east. It is bounded by faults [Schultz, 1991; Witbeck et al., 1997] associated with the extension of the chasmata and the subsidence of the region [Andrews-Hanna, 2012]. However, there have been no detailed proposals for the formation of this ~1000 km long chasma.

Results from the MSSD and rake analysis in Chapter 3 showed a marked difference between western and eastern Coprates Chasma (Figure 4-9). This difference is in the morphology of the spurs which become less pronounced towards the east (Figure 4-9A). These results led in Chapter 3 to the suggestion that the asymmetry of the chasma involves not only narrowing towards east but also a decrease in the height of the walls from ~10 km to 6 km [Chapter 3].

I present a hypothesis for a multiple-stage formation for Coprates Chasma involving the already suggested extensional and subsidence processes. The stages of formation are based on a division of the chasma into sections of Coprates Chasma based on the results from the MSSD and rake analysis, as well as other morphological and geological observations. It is proposed that Coprates Chasma originated as four isolated smaller chasmata, here referred to as West Coprates, Central Coprates, East Coprates, and South Coprates (Figure 4-9). This classification will be explained in following subsections.

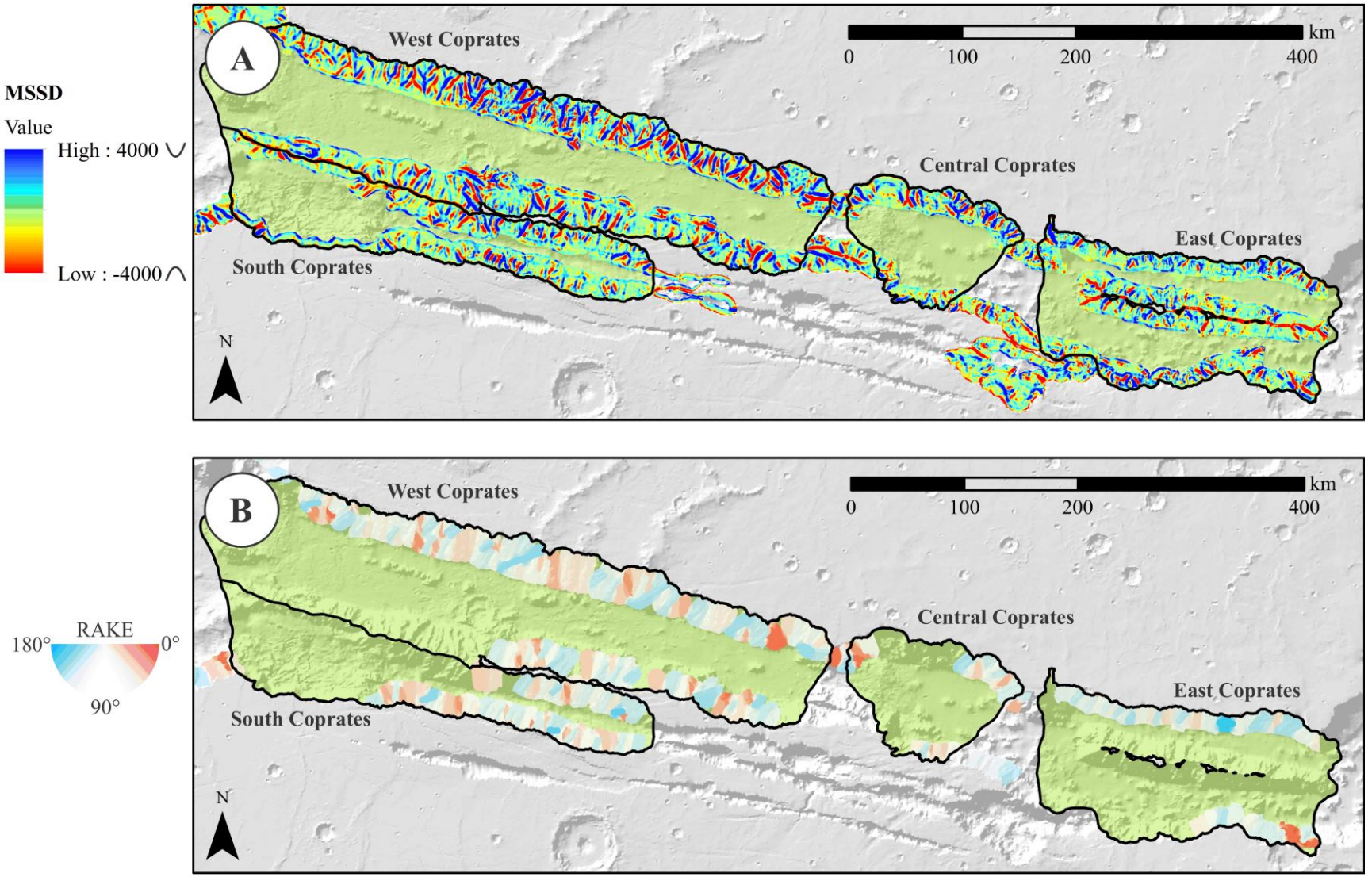

Figure 4-9: (A) MSSD and (B) rake analysis of the walls of Coprates Chasma. Highlighted areas contour the proposed sections of Coprates Chasma.

The MSSD analysis shows that the SGs at West Coprates have higher relief than those observed on East Coprates. This can be observed by the higher concentration of blue and red on the color-scheme of the walls (Figure 4-9A).

The MSSD results were further analyzed by quantifying the pronounced relief of the spurs of each section of the chasma into histograms (Figure 4-10). Negative MSSD values representing the curvature of the ridges, the values being taken for every pixel of the surface of the wall. The pixel counts were normalized in order to compare them. Positive MSSD values representing troughs were ignored since they can be infilled leading to a misinterpretation of the results.

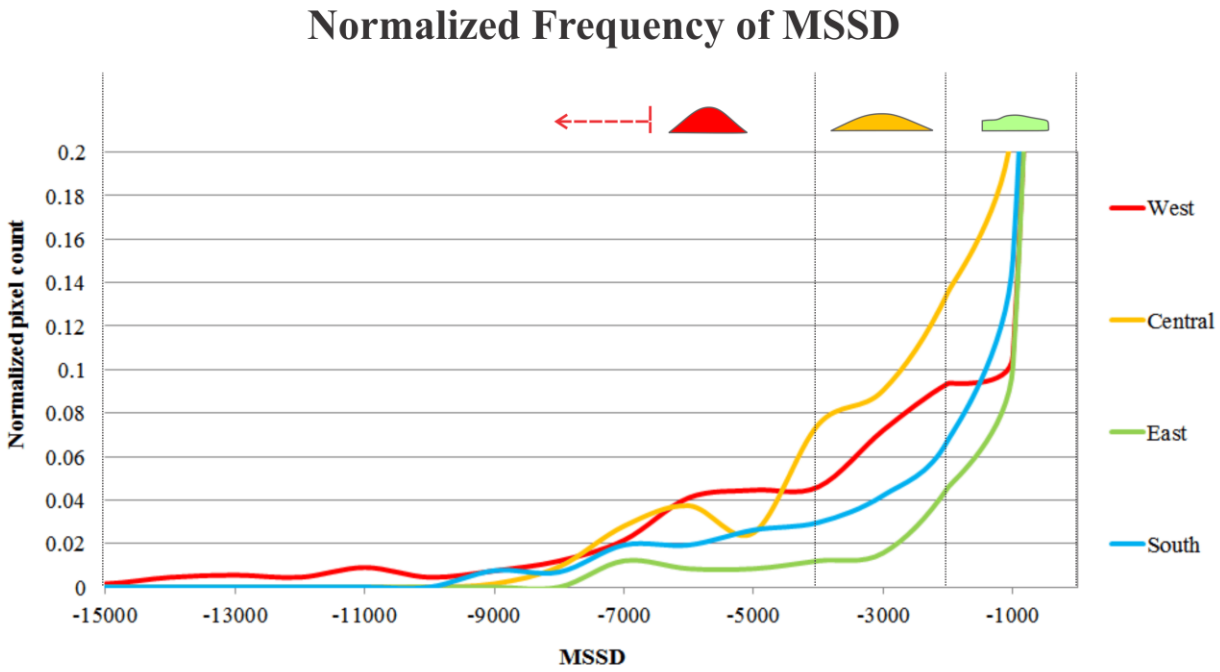

Figure 4-10: Comparison of the MSSD pixel counts showing the relief of the sections of Coprates Chasma. At the top of the graph the pronounced relief of the spurs based on the defined MSSD is shown with the respective color-scheme [Chapter 3].

Comparison shows that tighter ridges are observed on the walls of West Coprates and Central Coprates (Figure 4-10). The relatively small size of Central Coprates provides fewer data points which may explain some of the variations of the curve. The higher curvature values are associated with greater relief; this indicates that the walls of East Coprates have shallower SGs based in the observed distribution of MSSD values on Figure 4-10.

This observation is comparable to the other sections of Coprates Chasma where it is noticed that SGs in South Coprates have lower relief even with its closeness to West Coprates (Figure 4-9 and Figure 4-10). These results infer a possible division as illustrated in Figure 4-9. Nonetheless, it is necessary to specify other characteristics such as the orientation of the spurs.

The orientation of the spurs can indicate a dominant orientation in the erosion of the walls. The results from the rake analysis were quantified using rose diagrams weighted by the length of the spurs (Figure 4-11). The diagrams are shown as half circles oriented according to the attitude of the measured rakes having the semi-circles facing each other similar to their position in the walls. The scale of the diagrams goes from 0-180° following the right hand rule (Figure 4-11). Each facing pair of diagrams was scaled to the same weight range for a better interpretation.

Further evidence for the complex formation of Coprates comes from the shape of the chasma. The rake analysis shows that the spurs of West Coprates have a wide range of orientations, this can be seen from the various peaks on the distributions Figure 4-11A. However, not all of them have a representative length.

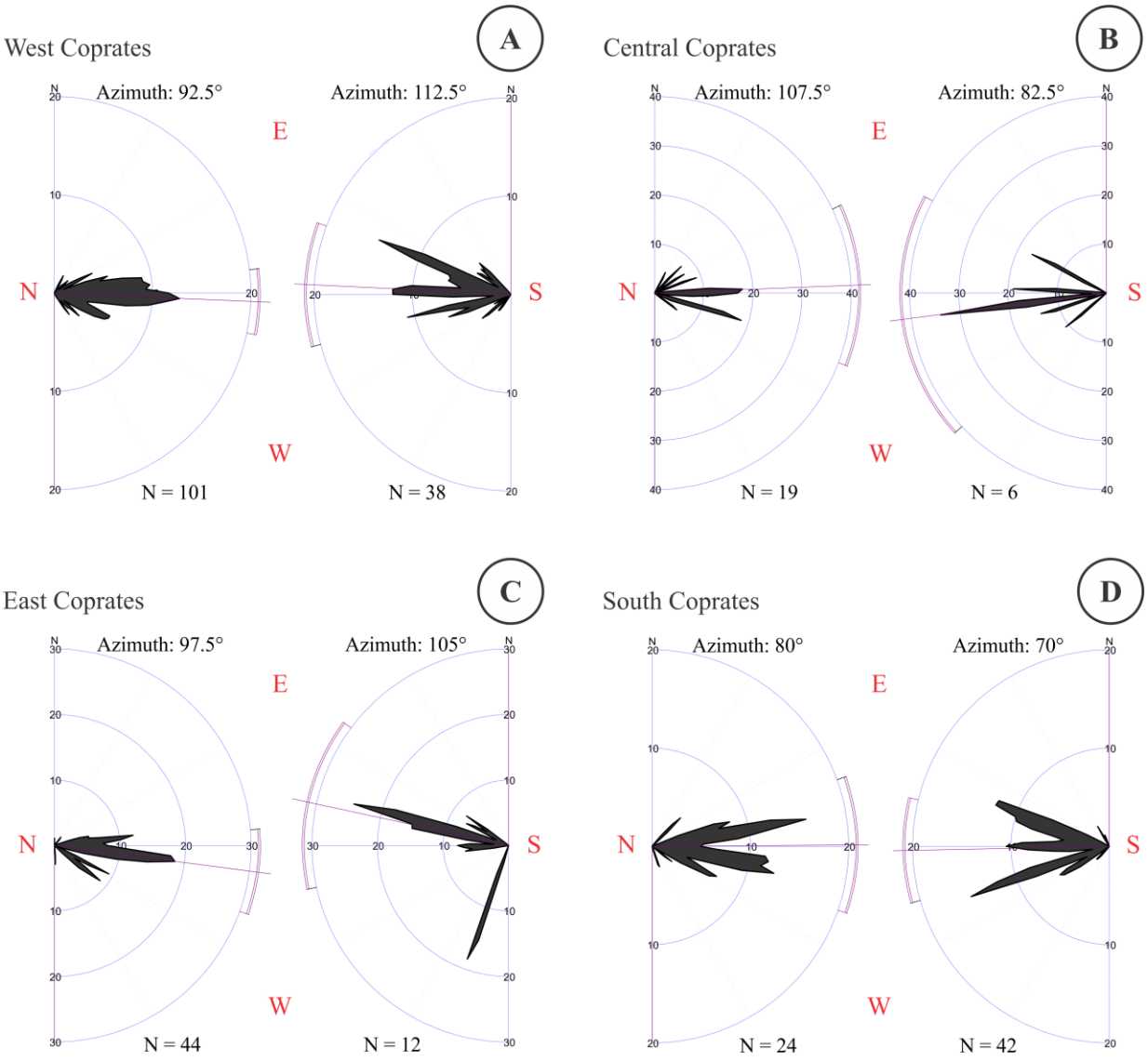

Figure 4-11: Rose diagrams of the measured rakes of the spurs of (A) West Coprates (B) Central Coprates (C) South Coprates (D) East Coprates.

Central Coprates appears to have a slightly rounded shape as observed from the attitude of its walls. The rose diagrams of Central Coprates show a higher variance than West Coprates considering that its peaks have greater lengths than those on Western Coprates. It is inferred that this distribution is associated with its slightly rounded shape (Figure 4-11 A&B). The spurs within its walls are orientated towards the center of the section. If the walls eroded in the direction of the spurs, it can be inferred that it was once a small chasma, possibly similar to a large pit chain depression (Figure 4-9). East Coprates shows peaks that could be associated with the wall retreat and the collapse of its walls (Figure 4-11C). Similarly South Coprates has peaks with equal deviation from the expected 90° trend (Figure 4-11D) which could be associated with its origin similar to the erosion of pit chains, based on a comparison of pits parallel to it towards the east (Figure 4-9B). It is proposed that the divided formation of Coprates Chasma occurred similar to the formation of pit chains such as those formed south of the chasma (Figure 4-9).

These results form the basis for the division of Coprates Chasma into smaller chasmata. The proposed sections of the chasma are divided in main and secondary stages where the main stages are West Coprates, Central Coprates, and East Coprates. South Coprates is divided into main and secondary due its connection to the pit chains aligned with it (Figure 4-12).

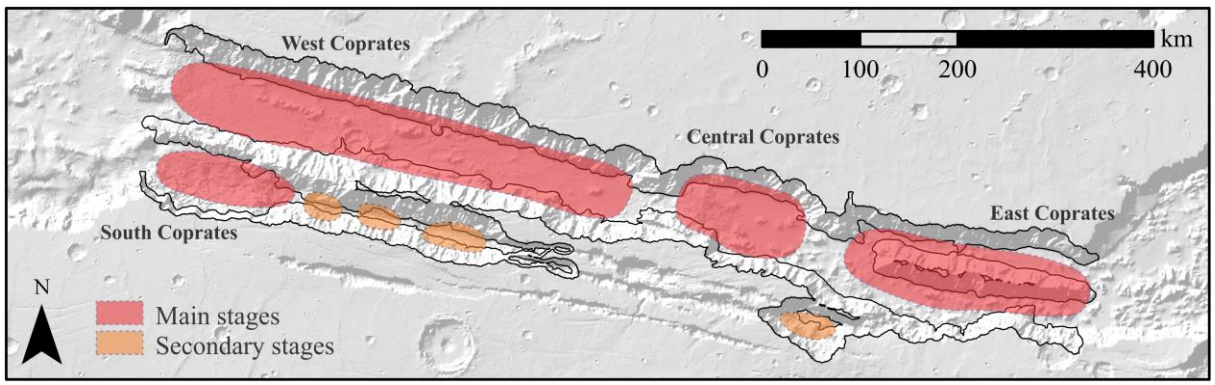

Figure 4-12: Division of the sections of Coprates Chasma into stages.

West Coprates and South Coprates are considered to be the oldest parts of Coprates Chasma due their relatively long walls compared to Central Coprates and East Coprates [Chapter 3] and the presence of interior layered deposits [Fueten et al., 2010, 2011]. The presence of such deposits within the chasma indicates that the floor was already formed during the lacustrine period of Valles Marineris, allowing the formation of the deposits [Lucchitta, 2010]. The interior layered deposits and the connection to the pit chains are reasons to separate South Coprates into two different stages of formation. West Coprates only has interior layered deposits in one region although its morphology indicates that its formation was not sectioned. The lack of divisions of the walls similar to those regions between West Coprates and Central Coprates or Central Coprates and East Coprates corroborates the inference of West Coprates as a singular section.

It is considered that the formation of Melas Chasma is linked and influenced the formation of West Coprates and South Coprates. This is based on the widening of Coprates towards west. This hypothesis will be explored in the section 4.4.

Other observation used for the division of Coprates is the presence of faults within the chasma. Faults associated with the formation of the chasma can be traced within the walls as part of their collapse from the extensional formation [Chapter 2]. However, not all the faults can be traced along the full extent of Coprates, such as the example of the faults associated with the formation of Nectaris Montes. Nectaris Montes is a large ridge formed within Coprates Chasma. The presence of Nectaris Montes indicates that this section of the chasma was formed individually, as the faults that formed it cannot be traced to the other sections of the chasma (Figure 4-13A). This makes a boundary between East Coprates and the other sections. These observations led the way to the proposal of the following stages involved in the formation of Coprates Chasma.

4.3.1. Stage 1: Formation of grabens and fracturing of the Tharsis province

During the formation of the Tharsis province faulting occurred in various orientations due the isostatic subsidence from the Tharsis load and the influence of the dichotomy in the formation of Valles Marineris [Knapmeyer et al., 2006; Andrews-Hanna, 2012]. This part of the formation of the Tharsis province would be the first process involved in the formation of Coprates Chasma. The event set the trend of the chasma by fracturing Tharsis and forming radial grabens. These grabens are subparallel to Coprates Chasma [Witbeck et al., 1997; Tanaka et al., 2014]. The fracturing initiated the formation of Coprates Chasma (Figure 4-13A).

Fault scarps parallel to the walls indicate a possible major graben that formed the base of Coprates Chasma (Figure 4-13A). The faults nucleated along the length of Coprates Chasma facing each other. Two major faults are identified along various locations on the walls (i.e. outer faults on Figure 4-13A).

Other faults are possibly secondary and are aligned with the fault planes that formed Nectaris Montes (i.e. inner faults on Figure 4-13A) at the eastern end of Coprates. Nectaris has remnants of plateau at a lower elevation of ~ 200 m from the surrounding plana that suggest that this block was part of the Tharsis Rise and slightly subsided (Figure 4-13B). Other faults associated with grabens are observed south of Coprates Chasma; however, they appear not to have a strong influence as the ones marked (Figure 4-13A).

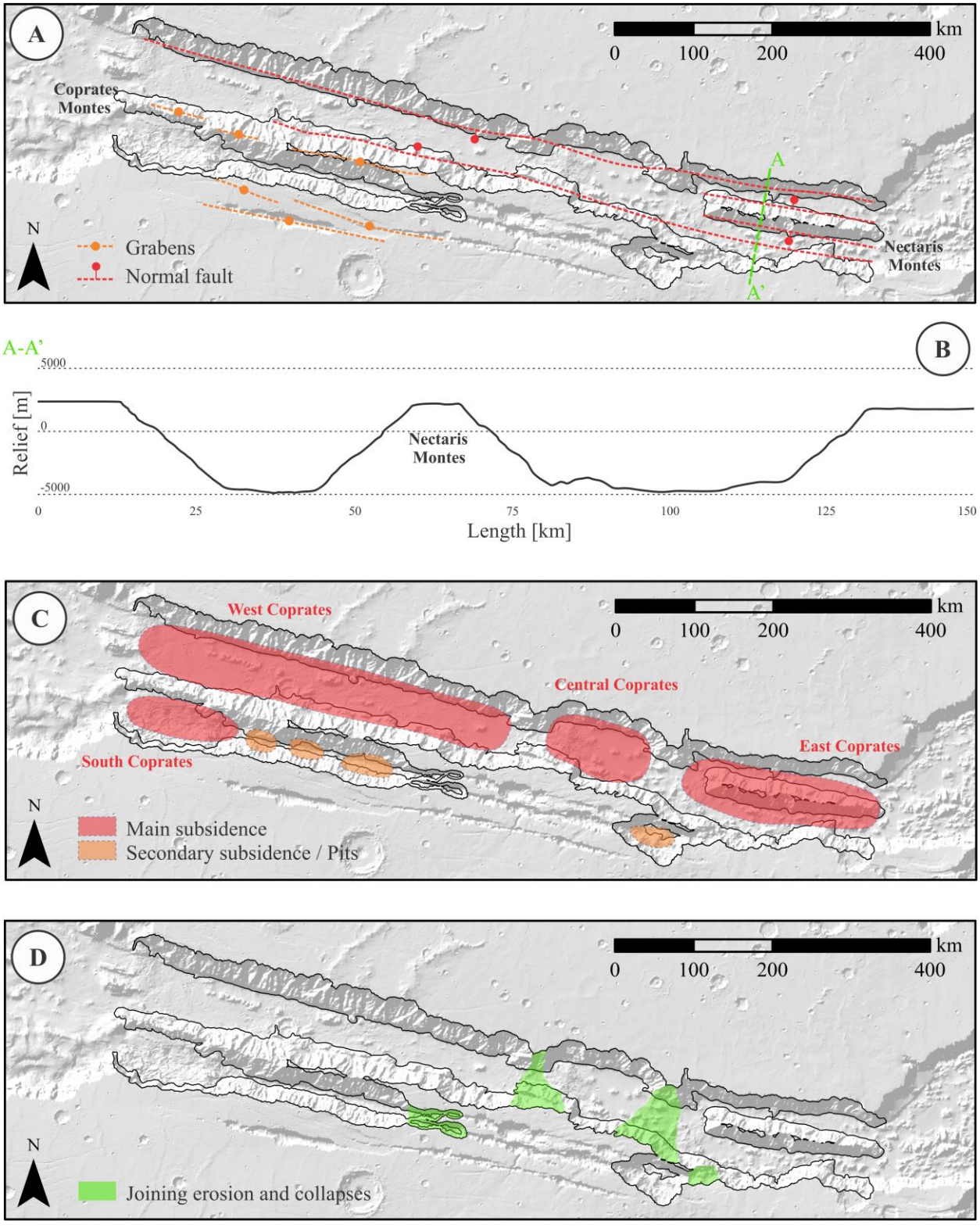

Figure 4-13: (A) Main faulting stage of Coprates Chasma (B) cross-section profile of Nectaris Montes (C) division of the subsidence of Coprates Chasma (D) joining of Coprates sections towards its current and final form.

4.3.2. Stage 2: Isolated subsidence and division of Coprates

The main faulting event formed the basis of what would be Proto-Coprates Chasma. This event facilitated the subsidence of the region that gave the rectangular shape of Coprates Chasma. The subsidence of Coprates Chasma is proposed as a process that occurred in different locations at possibly different rates (Figure 4-13C). Comparison of the extent of the walls and the differing depths of the sections of Coprates Chasma suggest that the subsidence of central Valles Marineris might have been greater than Melas Chasma.

West Coprates is the section of the chasma with the greatest depth, which suggests that greater subsidence was involved. West Coprates and South Coprates are two parallel sections linked by Coprates Montes (Figure 4-13A), yet West Coprates appears to have involved a greater subsidence judging from its larger size and deeper walls. South Coprates is suggested to have subsided and eroded towards the pit chains adjacent to Coprates Chasma due their alignment and current linkage. However, its location and connection to West Coprates affected its formation. It is proposed that West Coprates and South Coprates started their formation first, based on the presence of the interior layered deposits which are assumed to have formed early in the process.

Central Coprates is considered to have initiated its formation as an isolated smaller chasma that separated both West Coprates and East Coprates (Figure 4-13C). Within Central Coprates, there are no traces of faulting associated with the faults of Nectaris Montes. Its relatively smaller size compared to West Coprates and East Coprates suggests that central Coprates is the result of mostly subsidence and overall collapse of the region based on the low structural influence observed on the MSSD and rake results (Figure 4-9). However, Central Coprates might have originated as an ancestral basin similar to other chasmata [Schultz, 1998].

Subsidence of East Coprates probably occurred as single event due the presence of Nectaris Montes, a horst that remained and formed the Montes (Figure 4-13C). The slightly shorter walls of East Coprates and the low difference in elevation between the surrounding plateau and Nectaris Montes (~200 m) suggests that the vertical displacement of this section of Coprates could have been lower.

Other regions linked to the chasma are suggested as secondary subsidence or pits due their relatively smaller size compared to the sections of Coprates Chasma (Figure 4-13C). These secondary subsiding regions joined the main chasma during later processes forming one trough with South Coprates.

4.3.3. Stage 3: Retreat and erosion of the walls

The four proposed isolated sections of Coprates joined to form Coprates Chasma once the walls eroded joining them. This is considered the last stage of the formation of the chasma, which involved erosional processes and multiple stages of faulting that cut the walls. As result, the walls retreated expanding the sections of the chasma to join as one (Figure 4-13D).

The enlargement of South Coprates by joining with the secondary subsiding pits formed a trough adjacent to Coprates Montes (Figure 4-13D). The spurs formed within this trough follow the regular downslope orientation with various dominant orientations that suggest erosion of the walls and wall retreat, rather than structural influence from pre-existing faults (Figure 4-13A).

The SG wall morphology formed during those processes exposing the pre-existing faults within Tharsis and was influenced by the presence of those faults, as shown and exemplified in Chapters 2 and 3. Based on the observed MSSD results, it can be inferred that SGs with higher relief have been exposed for longer periods.

This hypothesis proposes a complex formation for Coprates Chasma based on structural features within the walls of the chasma. The large length of Coprates Chasma is one of the conditions that make the isolated formation of sections that joined overtime possible. The complex formation for Valles Marineris would better explain the diversity of structures observed within each chasmata.

4.4. Intersected faults along the Ius-Melas-Coprates trough

Previous sections explored isolated cases where pre-existing faults and chasma-producing faults influence the formation of the walls. The recognition of these faults helps explain their formation. This section explores a hypothesis of a linked formation for the Ius-Melas-Coprates trough. Coprates Chasma and Ius Chasma, two of the largest chasmata of Valles Marineris are connected by Melas Chasma, a wide intermediate chasma (Figure 4-14A). The hypothesis involves the late Hesperian grabens observed on western Ophir Planum as part of an analogy between these and the oldest grabens that trend subparallel to the trough along each chasmata formed prior to or during Proto Valles Marineris (Figure 4-14A).

Inspection of the western margins of Coprates Chasma shows a rotation of ~30° clockwise of the attitude of the northern wall as it merges into Melas Chasma (Figure 4-14C). This change of azimuth appears similar to the change in trend of the grabens on Ophir Planum [Schultz, 1991]. The grabens appear in two sets, both trending NW-SE, that linked as their faults intersect, forming an en echelon configuration [Schultz, 1991; Hauber et al., 2007] (Figure 4-14B).

It is proposed that the formation of the Ius-Melas-Coprates trough involves similar mechanics to the one observed at Ophir Planum. The mechanics relies on the interaction and connection among the grabens north of Ius Chasma and the grabens south of Coprates Chasma

that bound in a similar en echelon configuration over a longer distance. The proposed location of the two joined graben sets is the present location of Melas Chasma (Figure 4-14C).

The faults associated with these grabens led to the formation of the rectangular shape of Ius Chasma and Coprates Chasma, where the tension grew lengthening the faults [Schultz, 1991; Twiss and Moores, 2007]. This mechanism propagated the isolated faults along their respective orientation. The bounding faults of Ius and Coprates extended towards each other during the evolution of the chasmata formation. The orientation of the growing fault segments changed to an en echelon configuration similar to the one observed on Ophir Planum (Figure 4-14 B&C) [Schultz, 1991].

The configuration shaped Melas Chasma once the chasmata started subsiding. The chasma mimicked the curvature of the suggested en echelon configuration. It is difficult to identify the connection of the faults in Melas Chasma since it has been highly modified, having a covered floor and walls with no trace of the connection (Figure 4-14C). However, it can be inferred that the retreat of the southern wall of Melas follows the direction of the proposed en echelon curvature with the presence of curved faults on its southern plateau. The subsidence of Melas Chasma and later formation of Valles Marineris covered any possible fault trace that could have been visible on the floor (Figure 4-14). It is proposed that Melas Chasma is the result of the collapse of a fractured region formed by the en echelon system from the connection between the faults of the grabens of Ius Chasma and Coprates Chasma. The wide irregular shape of Melas can be associated with the active erosion of its walls. It is unlikely that this complex geometry of the current faults is the result of one single mechanism. This hypothesis indicates that a more complex history is involved in the formation of central Valles Marineris. Multiple structures within Tharsis interact forming what now is known as Valles Marineris.

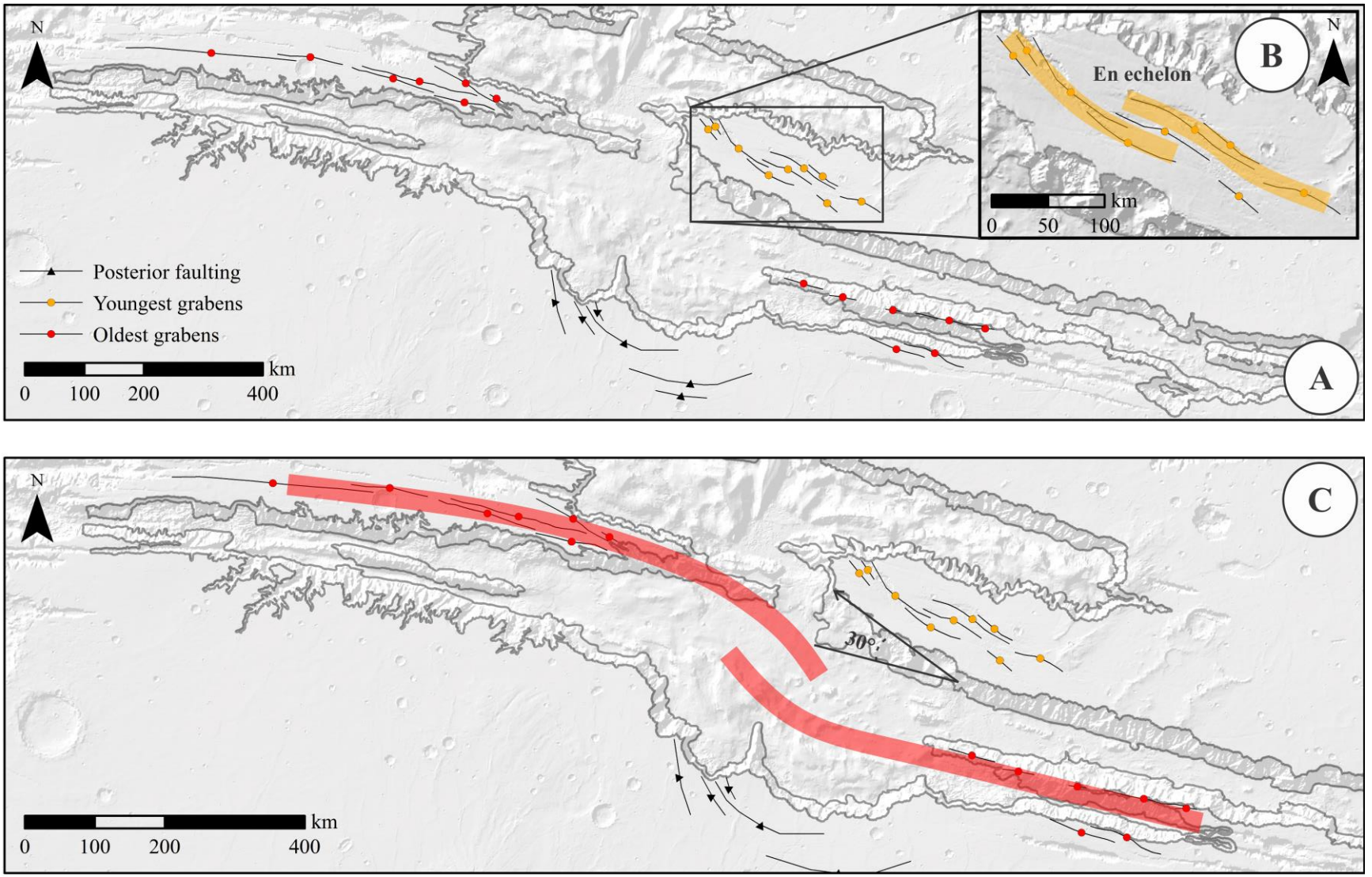

Figure 4-14: (A) Traces of the grabens along the chasmata, the late Hesperian grabens on Ophir Planum, and faulting of the plateau that surrounds Melas Chasma (B) en echelon configuration of the grabens at Ophir Planum (C) proposed propagation zones inferred from the observed faults.

Chapter 5 : Summary and Conclusions

In previous chapters, I examined variations of the spur and gully (SG) wall morphology. The full extent of the walls was analyzed using several methodologies such as dip analysis, Mean Signed Square Difference (MSSD) analysis, rake analysis, and the Augmented Visualization of Attitude (AVA) analysis. Their use allowed for the geometrical characterization of variations of the wall morphology. These geometries were classified into indicators of structural influence within the SG wall morphology. These indicators were used and presented in Chapter 2, 3 and 4 as specific cases.

Chapter 2 studied ridges, focusing on wrinkle ridges. Wrinkle ridges that surround central Valles Marineris were compared and the results suggest that their morphology varies based on the lithology and their location. This suggests that the lithological influence affected the relief of wrinkle ridges where greater heights are identified within relatively young deposits. However, based on their distribution and extension within those plana, it is considered that strain distribution has a greater role in their morphology.

The comparison led to the classification of the Large Wrinkle Ridges (LWRs). Their isolated location provided a perspective of their underlying structure due their location near the wallslope. These LWRs were associated with Anomalous Planes (APs) on the walls; their connection was tested using a numerical model. The results indicate a connection between surface structures and features on the chasma walls, implying that there is structural influence on the wall morphology of Valles Marineris beyond the presence of facets, which can be recognized using the indicators.

Chapter 3 shows that the indicators are the expression of faults on the walls that deformed and/or reshaped the spurs and the attitude of the walls. This chapter shows the proper use of each methodology in the study of structural influence. The dip analysis helps in the recognition of shallow areas and possible deposits within the walls appearing as clusters of similar dips. This analysis provides insight on the consistency of the wallslope, making it easier to observe variation in the slope along a surface.

MSSD results help in the identification of spurs on the walls that are associated with pre-existing faults, observed as large long ridges that extend beyond the length of the walls, as oblique spurs along the walls, and reoriented walls. The large long spurs in many cases are longer than the wallslope extent of their corresponding wall. This is due to their formation being influenced by fault planes that expose stronger lithology, with the footwall being more resistant to erosion during the formation of the walls.

Comparing MSSD and Length-Throw-Slope (LTS) results show that the walls of Coprates Chasma have well pronounced SGs within the western region of chasma while the eastern regions have shorter walls and less pronounced spurs. This suggests a connection between the extent of the wallslope and the length of the spurs. This observation appears to apply mostly to chasmata with rectangular shape, such as Coprates Chasma and Candor Chasma, as the comparison does not show the same correspondence for chasmata such as Melas Chasma and Ophir Chasma. The irregular shape of these latter two chasmata and the high population of landslides obscured any possible connection between the observed spurs and their respective walls.

The orientation of all the well-defined spurs on the walls was studied using the rake analysis. The results showed that the majority of the spurs follow the expected downslope orientation nonetheless; many of them have orientations that deviate from the norm. The orientation of these spurs is considered the result of the influence of both chasma-producing faults and pre-existing faults. Chasma-producing faults produced scarps with a highly deviated angle from the norm based on the rake analysis, while pre-existing faults would result in the formation of large spurs with a slightly smaller deviated orientation. For example, the APs discussed in Chapter 2 are highlighted within the results of the rake analysis and AVA analysis. The results from these analyses showed that there are more APs on the walls than those associated with the LWRs. However, not all the APs could be matched or linked to formations on the nearby plana.

Analysis of the results of these methodologies demonstrated that each has a specific purpose and under the proper conditions can reveal geometries that indicate structural influence.

Chapter 4 shows the application of the results of the structural analysis to the walls of central Valles Marineris. This chapter introduced four special cases where the indicators of structural influence are used. The first case shows a V-shaped channel on the walls of East Candor Chasma. This channel was compared with tributary canyons, yet its morphology proved to be of structural origin. A major fault along the north wall of East Candor is thought to be partly responsible for the formation of this channel. It is proposed that channels formed by structural influence have competent planar walls rather than the curved walls of channels formed by erosional processes.

Similarly, an hourglass graben crossing the southeast wall of East Candor Chasma almost perpendicularly influences the wall morphology by forming a large long spur along a fault plane. During erosion, the walls of the graben eroded to shallower values similar to the stable slope of Mars. The erosion of the walls affected not only the dip of the plane, the overall attitude of the plane changed, rotating away from the centerline of the graben. This was observed when comparing the attitude of the walls of the graben and the attitude of the flank of the spur and the southwest wall. A schematic model was proposed in order to explain the connection between the wall morphology and the morphology of the graben.

The third case takes into account the characteristics of the walls as an overall structure, using them to identify the segmented form of a chasma. Coprates Chasma was separated into four segments that were proposed to have been isolated smaller chasmata. MSSD and rake analysis results show that the orientation and relief of the spurs reveal the shaping of the chasma. It is suggested that the western region of Coprates Chasma is the oldest based on the presence of interior layered deposits and the observed high chasma relief. However, a definite order for individual formation cannot be established. Yet, this suggests a detail of the evolution of central Valles Marineris and how the chasmata can link to each other.

The last case is a proposed formation of the Ius-Melas-Coprates trough. It is based on the orientation of faults parallel to Ius Chasma and Coprates Chasma. It was suggested that the faults formed an en echelon configuration, linking in the current location of Melas Chasma. The existence of this configuration would explain the shape of Melas Chasma relative to the other chasmata. The proposal is based on a similar en echelon configuration of grabens on western Ophir Planum.

The cases presented here are the result of detailed analysis of the SG wall morphology and its relationship with the structures formed within the Tharsis province. The results from this work contribute to the understanding of the formation of the walls of Valles Marineris and the chasmata as a whole. The collected evidence of variations on the SG wall morphology demonstrates: 1) The underlying structure of wrinkle ridges can be more complex than previously used models; 2) The complexity of the structure influences the morphology of the wrinkle ridges; 3) Pre-exiting structures within the Tharsis province can influence the geometry of the walls; 4) The influence on the geometry of the walls due to pre-existing structures, and chasma producing faults, can be identified. Multiple indicators of structural influence that can be recognized and several locations along the walls of central Valles Marineris; and, 5) The formation of Valles Marineris is complex, but traces of its evolution are visible on the walls.

This work provides tools and criteria that would be useful for further research of the structures of Valles Marineris.

References

Anderson, R.C., Dohm, J.M., Golombek, M.P., Haldemann, A.F.C., Franklin, B.J., Tanaka, K.L., Lias, J., and Peer, B. (2001). Primary centers and secondary concentrations of tectonic activity through time in the western hemisphere of Mars. JGR, 1006(E9), 20563-20585.

Andrews-Hanna, J.C. (2012a). The formation of Valles Marineris: 1. Tectonic architecture and the relative roles of extension and subsidence. JGR, 117, doi:10.1029/2011JE003953.

Andrews-Hanna, J.C. (2012b). The formation of Valles Marineris: 2. Stress focusing along the buried dichotomy boundary. JGR, 117, doi:10.1029/2011JE003954.

Andrews-Hanna, J.C. (2012c). The formation of Valles Marineris: 3. Trough super-isostasy stress, sedimentation, and subsidence. JGR, 117, doi:10.1029/2012JE004059.

Atwood-Stone, C. and McEwen, A.S. (2013). Measuring dynamic angle of repose in low gravity environments using Martian sand dunes. LPSC 44th abstract#1727.

Banerdt, W.B., Golombek, M.P., and Tanaka, K.L. (1992). Stress and Tectonics on Mars. In Mars (H.H. Kieffer, B.M. Jakosky, C.W. Snyder and M.S. Matthews, Eds.), 249-297, Univ. of Arizona Press, Tucson.

Bieniawski, Z. T., (1993). Classification of rock masses for engineering: The RMR system and future trends, in Comprehensive Rock Engineering, vol. 3, edited by J. A. Hudson and E. Hoek, pp. 553 – 573, Pergamon, New York.

Blackwelder, E. (1928). The recognition of Fault Scarps. Journal of Geology, 36(4).

Blasius, K. R., Cutts, J. A., Guest, J. E. and Masurky, H. (1977). Geology of the Valles Marineris: First Analysis of Imaging From the Viking 1 Orbiter Primary Mission. J. Geophys. Res., 82, 4067-4091.

Broxton, M.J., and Edwards, L.J. (2008). The Ames Stereo Pipeline: Automated 3D Surface Reconstruction from Orbital Imagery. LPSC 34th abstract#2419.

Brustel, C., Flahaut, J., Hauber, E., Fueten, F., Quantin, C., Stesky, R., and Davies, G.R. (2017). Valles Marineris tectonic and volcanic history inferred from dikes in eastern Coprates Chasma. JGR, 122, doi:10.1002/2016JE005231.

Bryan, W.B. (1973). Wrinkle-ridges as deformed surface crust on ponded mare lava. Proc. Lunar Sci. Conf., 4th, 93-106.

Calkin, P. B. (1971). Glacial geology in the Victoria Valley system, southern Victoria Land, Antarctica, in Crary, A. P., ed., Antarctic Research Series, v. 16: Am. Geophys. Union, Washington, D.C. p. 363-412.

Carr, M.H. and Head, J.W. (2009). Geologic history of Mars, Earth and Planet. Sci. Let., 294, 185-203, doi:10.1016/j.epsl.2009.06.042.

Caruso, P. A. (2002). Seismic triggering of Martian landslides and slope stability for Valles Marineris, Mars, M.S. thesis, University of Nevada, Reno, 92 pp.

Cole, H.M., and Andrews-Hanna, J.C. (2017). The anatomy of a wrinkle ridge revealed in the wall of Melas Chasma, Mars. JGR: Planets, 172, doi:10.1002/2014JE005274.

Davis, J.C. (2002). Statistics and data analysis in geology. Third Edition. John Wiley & Sons, USA. ISBN 0-471-17275-8.

Davis, P.A., and Golombek, M. P. (1990). Discontinuities in the Shallow Martian Crust at Lunae, Syria, and Sinai plana. JGR, 95(B9), 14231-14248.

Debniak et al. (2017). Map Geomorphology of Ius Chasma, Valles Marineris, Mars.

DeHon, R.A. (1985). Thickness of ridged plains materials in Hesperian Planum, Mars. Reports Planet. Geol. Prog.

DeHon, R.A. (1988). Progress in determining the thickness and distribution of volcanic materials on Mars. In MEVTV Workshop: Nature and composition of Surface units on Mars, Houston. 54-56.

Dimitrova, L.L., Holt, W.E., Haines, A.J., and Schultz, R.A. (2006). Towards understanding the history and mechanisms of Martian faulting: The contribution of gravitational potential gravity. Geo. Red. Lett., 33.

Fergason, R.L., Laura, J.R., Hare, T.M. (2017). THEMIS-Derived Thermal Inertia on Mars: Improved and Flexible Algorithm, Lunar and Planetary Science XLVIII, abs. #1563.

Frey, H., and Grant, T. (1990). Resurfacing history of Tempe Terra and surroundings. J. Geophys. Res., 95, 14249-14263.

Fueten, F., Flahaut, J., Le Deit, L., Stesky, R., Hauber, E., and Gwinner, K. (2011). Interior layered deposits within a perched basin, southern Coprates Chasma, Mars: Evidence for their formation, alteration, and erosion. JGR, 116, E02003, doi:10.1029/2010JE003695.

Fueten, F., Novakovic, N., Stesky, R., Flahaut, J., Hauber, E., & Rossi, A. P. (2017). The evolution of Juventae Chasma, Valles Marineris, Mars: Progressive collapse and sedimentation. Journal of Geophysical Research: Planets, 122, 2223–2249. https://doi.org/10.1002/2017JE005334.

Fueten, F., Racher, H., Stesky, R., MacKinnon, P., Hauber, E., McGuire, P.C., Zegers, T., and Gwinner, K. (2010). Structural analysis of interior layered deposits in Northern Coprates Chasma, Mars. Earth and Plan. Sci. Lett., 294, 343-356.

Fueten, F., Stesky, R., MacKinnon, P., Hauber, E., Zegers, T., Gwinner, K., Scholten, F., and

Neukum, G. (2008). Stratigraphy and structure of interior layered deposits in west Candor Chasma, Mars, from High Resolution Stereo Camera (HRSC) stereo imagery and derived elevations. JGR 113, doi:10.1029/2007JE003053.

Golombek, M. P. (1979). Structural analysis of lunar grabens and the shallow crustal structure of the Moon. Journal of Geophysical Research, 84, 4567-666.

Golombek, M. P. and McGill, G. E. (1983). Grabens, basin tectonics, and the maximum total expansion of the Moon. Journal of Geophysical Research, 88, 3563-78.

Golombek, M.P., and Phillips, R.J. (2010). Mars Tectonics, in: Planetary Tectonics, T.R. Watters and R.A. Schultz (Eds.), pp. 183-232, Cam-bridge Univ. Press.

Golombek, M.P., Plescia, J.B., and Franklin, B.J. (1991). Faulting and folding in the formation of planetary wrinkle ridges. Proc. Lunar Planet. Sci, 21, 679-693.

Greeley, R., and Spudis, P.D. (1981). Volcanism on Mars. Rev. Geophys., 19,13-41.

Gwinner, K., et al. (2016). The High Resolution Stereo Camera (HRSC) of Mars Express and its approach to science analysis and mapping for Mars and its satellites. Plan. And Space Sci. 126, 93-138.

Hartmann, W. K., and Neukum, G. (2001). Cratering chronology and the evolution of Mars. Chronology and evolution of Mars, 165-194. Springer Netherlands.

Hauber, E., Charalambakis, E., Gwinner, K., Grott, M., Knapmeyer, M., Matz, K.D., and Wahlisch, M. (2007). Displacement-Length relationship of normal faults on Mars: New observations with MOLA and HRSC. Lunar and Planetary Science Conference XXXVIII, abstract #1670.

Hauber, E., Grott, M., and Kronberg, P. (2010). Martian rifts: Structural geology and geophysics. Earth and Pla. Sci. Lett. 294, 393-410.

Jackson, M. P. A., Adams, J. B., Dooley, T. P., Gillespie, A. R., and Montgomery, D. R. (2011). Modeling the collapse of Hebes Chasma, Valles Marineris, Mars. Geological Society of America Bulletin, 123(7-8), 1596-1627.

Kleinhans, M.G., Markies, H., de Vet, S.J., in't Veld, A.C., and Postema, F.N. (2011). Static and dynamic angles of repose in loose granular material under reduced gravity. JGR, 116, doi:10.1029/2011JE003865.

Knapmeyer, M., Oberst, J., Hauber, E., Wahlisch, M., Deuchler, C., and Wagner, R. (2006). Working models for spatial distribution and level of Mars' seismicity, J. Geophys. Res., 111, E11006, doi:10.1029/2006JE002708.

Laity, J.E., and Malin, M.C. (1985). Sapping processes and the evolution of theater-headed valley networks on the Colorado Plateau. GSA Bulletin, 96.

Laura, J., and Fergason, R.L., (2016). Modeling Martian thermal inertia in a distributed memory high performance computing environment, Big Data, IEEE International Conference, Washington, DC., DOI: 10.1109/BigData.2016.7840942.

Lin, J. and Stein, R.S. (2004). Stress triggering in thrust and subduction earthquakes, and stress interaction between the southern San Andreas and nearby thrust and strike-slip faults, Journal of Geophysical Research,, v. 109, B02303, doi:10.1029/2003JB002607.

Lucchitta, B.K. (1978). Morphology of chasma walls, Mars. Jour. Research U.S. Geol. Survey, 6(5), 651-662.

Lucchitta, B.K. (1979). Landslides in Valles Marineris, Mars. JGR, 84(B14), 8097-8113.

Lucchitta, B.K. (1990). Young Volcanic Deposits in the Valles Marineris Mars?.

Lucchitta, B.K. (2010). Lakes in Valles Marineris, in: Lakes on Mars, Cabrol, N.A., and Grin, E.A. (Eds.), pp. 183-232, Elsevier.

Lucchitta, B.K., Isbell, N.K., Howington-Kraus, A. (1994). Topography of Valles Marineris: implications for erosional and structural history. J. Geophys. Res. 99, 3783–3798.

Mangold, N., Allemand, P., and Thomas, P.G. (1998). Wrinkle ridges of Mars: Structural analysis and evidence for shallow deformation controlled by ice-rich decollements.

Maxwell, T.A., El-Baz, F., and Ward, S.W. (1975). Distribution, morphology, and origin of ridges and arches in Mare Serenitatis. Geol. Soc. Am. Bull., 86, 1273-1278.

McKenzie, D., and Nimmo, F. (1999). The generation of Martian floods by melting of ground ice above dykes. Nature, 397, 231-233, doi: 10.1038/16649.

Mege, D., and Bourgeois, O. (2011). Equatorial glaciations on Mars revealed by gravitational collapse of Valles Marineris wallslopes. Earth and Planetary Sci. Letters, 310, 182-191.

Mege, D., and Masson, P. (1996). A plume tectonics model for the Tharsis province, Mars. Planet. Space. Sci., 44, 1499-1546.

Minin, M., Vargas, L., Fueten, F., Stesky, R., and Hauber, E. (2015). A new automated technique within ArcGIS to compute the attitudes of planar topographic features. LPS XLVI, abstract #1577.

Montgomery, D.R., Som, S.M., Jackson, M.P.A., Schreiber, B.C., Gillespie, A.R., and Adams, J.B. (2009). Continental-scale salt tectonics on Mars and the origin of Valles Marineris and associated outflow channels. GSA Bulletin, 121, 117-133, doi:10.1130/B26307.1.

Moratto, Z. M., Broxton, M. J., Beyer, R. A., Lundy, M., & Husmann, K. (2010). Ames Stereo Pipeline, NASA's Open Source Automated Stereogrammetry Software. 41st Lunar and Planetary Science Conference, held March 1-5, 2010 in The Woodlands, Texas. LPI Contribution No. 1533, p.2364.

Mouginis-Mark, P.J., Wilson, L., and Zuber, M.T. (1992). The physical volcanology of Mars. In Mars (H. H. Kieffer, B.M. Jakosky, C.W. Snyder, and M.S. Matthews, Eds.), 424-452, Univ. of Arizona Press, Tucson.

Murchie, S.L., Roach, L.H., Seelos, F.P., Milliken, R.E., Mustard, J.F., Arvidson, R.E., Wiseman, S.M., Lichtenberg, K.A., Andrews-Hanna, J.C., Bibring, J.-P., Bishop, J.L., Parente, M., Morris, R.V. (2009). Evidence for the origin of layered deposits in Candor Chasma, Mars, from mineral composition and hydrologic modeling, Journal of Geophysical Research, 114, E00D05, doi:10.1029/2009JE003343.

Okubo, C.H., and Schultz, R.A. (2003). Thrust fault vergence directions on Mars: A foundation for investigating global-scale Tharsis-driven tectonics. Geophysical Research Letters, 30(22), doi:10.1029/GL018664.

Okubo, C.H., and Schultz, R.A. (2004). Mechanical stratigraphy in the western equatorial region of Mars based on thrust fault-related fold topography and implications for near-surface volatile reservoirs. GSA Bulletin, 116(5/6), 594-605, doi:10.1130/B25361.1.

Ori, G.G. and Karna, A. (2003). The uppermost crust of Mars and flood basalts. Lunar and Planetary Science Conference XXXIV, abstract #1539.

Pangaea Scientific (2006-2011). Orion: Orientation Hunter [computer software]. Supported by Canada Centre for Remote Sensing, Natural Resources Canada. Brockville, Ontario, Canada.

Patton, P.C. (1990). Erosional development of bedrock spur and gully topography in the Valles Marineris, Mars. NASA Tech. Memo.

Peulvast, J.P., and Masson, P.L. (1993). Erosion and tectonics in Central Valles Marineris (Mars): A new morpho-structural model. Earth, Moon, and Planets 61: 191-217.

Peulvast, J.P., Mege, D., Chiciak, J., Costard, F., and Masson, P. (2001). Morphology, evolution and tectonics of Valles Marineris wallslopes (MARS). Geomorphology, 37, 329-352.

Pieri, D.C. (1980). Martian Valleys: Morphology, Distribution, Age, and Origin, Science, 210, 4472, 895-897.

Robinson, M.S., and Tanaka, K.L. (1990). Magnitude of catastrophic flood event at Kasei Valles, Mars. Geology, 18, 902-905.

Schultz, R.A. (1989). Strike-slip faulting of ridged plains near Valles Marineris, Mars. Nature, 341.

Schultz, R.A. (1991). Structural Development of Coprates Chasma and Western Ophir Planum, Valles Marineris Rift, Mars. JGR, 96(E5), 22777-22792.

Schultz, R.A. (1998). Multiple-process origin of Valles Marineris basins and troughs, Mars. Planet. Space. Sci., 46(6/7), 827-834.

Schultz, R.A. (2000). Localization of bedding plane slip and backthrust faults above blind thrust faults: Keys to wrinkle ridge structure. J. Geophys. Re.., 105(E5), 12035-12052.

Schultz, R.A. (2002). Stability of rock slopes in Valles Marineris, Mars. JGR, 29(19), doi:10.1029/2002GL015728.

Schultz, R.A. and Tanaka, K.L. (1994). Lithospheric-scale buckling and thrust structures on Mars: The Coprates rise and south Tharsis ridge belt, JGR, 99(E4), 8371-8385.

Schultz, R.A., and Watters, T.R. (2001). Forward mechanical modeling of the Amenthes Rupes thrust fault on Mars. Geo. Res. Lett. 28(24), 4659-4662.

Schultz, R.A., Moore, J.M., Grosfils, E.B., Tanaka, K.L., and Mege, D. (2007). The Canyonlands model for planetary grabens: revised physical basis and implications. The Geology of Mars: Evidence from Earth-Based Analogs, ed. Mary Chapman. Published by Cambridge University Press, 371-399.

Schultz, R.A., Moore, J.M., Grosfils, E.B., Tanaka, K.L., Mege, D., Hauber, E., and Kronberg, P. (2000). Revised model for simple planetary grabens and tectonic implications. LPSC XXXI abstract #1175.

Sharp, R.B. (1973). Mars: Troughed terrain. Journal of Geophysical Research, 78, 4063–4072, doi:10.1029/JB078i020p04063.

Sharpton, V.L., and Head III, J.W. (1988). Lunar mare ridges: Analysis of ridge-crater intersections and implications for the tectonic origin of mare ridges. Proc. Lunar Planet. Sci. Conf., 18th, 307-317.

Smith, D.E., Neumann, G.A., Ford, P.G., Arvidson, R.E., Guiness, E.A., and Slavney, S. (1999a). Mars Global Surveyor Laser Altimeter Precision Experiment Data Record: MGS-M-MOLA-3-PEDR-L1A-V1.0: NASA Planetary Data System.

Smith, D.E., Neumann, G.A., Ford, P.G., Arvidson, R.E., Guiness, E.A., and Slavney, S. (1999b). Mars Global Surveyor Laser Altimeter Precision Experiment Data Record: MGS-M-MOLA-5-MEGDR-L3-V1.0: NASA Planetary Data System.

Spencer, J. R., and Fanale, F. P. (1990). New models for the origin of Valles Marineris closed depressions. Journal of Geophysical Research, 95(B9), 14,301–14,313.

Strom, R.G. (1972). Lunar mare ridges, rings and volcanic ring complexes. Mod. Geol., 2,133-157.

Tanaka, K. L., and Golombek, M.P. (1989), Martian tension fracture and the formation of grabens and collapse features at Valles Marineris, Lunar and Planetary Science, 19, 383–396.

Tanaka, K.L., Skinner Jr., J.A., Dohm, J.M., Irwin III, R.P., Kolb, E.J., Fortezzo, C.M., Platz, T., Michael, G.G., and Hare, T.M. (2014). Geologic map of Mars: U.S. Geological Survey Scientific Investigations Map 3292, scale 1:20,000,000, pamphlet 43 p., https://dx.doi.org/10.3133/sim3292.

Toda, S., Stein, R.S., Richards-Dinger, K., and Bozkurt, S. (2005). Forecasting the evolution of seismicity in southern California: Animations built on earthquake stress transfer, Journal of Geophysical Research, v. 110, B05S16, doi:10.1029/2004JB003415.

Twiss, R. J. and Moores, E. M. (2007). Structural Geology, 2nd ed.: xvi + 736 pp. New York: W. H. Freeman.

Viviano-Beck, C.E., Murchie, S.L., Beck, A.W., and Dohm, J.M. (2017). Compositional and structural constrains on the geologic history of eastern Tharsis Rise, Mars. Icarus, 284, 43-58.

Wallace, R.E. (1978). Geometry and rates of change of fault generated range fronts, North-Central Nevada. Jou. Res. U.S.G.S. 6(5), 637-650.

Watters, T. R. and Maxwell, T. A. (1986). Orientation, relative age, and extent of the Tharsis plateau ridge system. J. Geophys. Res. 91,8113-8125.

Watters, T.R. (1988). Wrinkle ridge assemblages on the terrestrial planets. J. Geophys. Res., 89, 10236-10254.

Watters, T.R. (1991). Origin of periodically spaced wrinkle ridges on the Tharsis plateau of Mars. JGR, 96(E1), 1599-15616.

Watters, T.R. (2001). Studies of Martian wrinkle ridges using MOLA topographic data: the nature of elevation offsets. Proc. Lunar Planet. Sci. Conf. 32nd. Lunar and Planetary Institute, abstract#1414.

Watters, T.R. (2004). Elastic dislocation modeling of wrinkle ridges on Mars. Icarus, 171, 284-294.

Watters, T.R., and Robinson, M.S. (1997). Radar and photoclinometric studies of wrinkle ridges on Mars. Journal of Geophysical Research, 102, 10889-10903

Watters, T.R., and Robinson, M.S. (2000). Topographic studies of wrinkle ridges: The significance of elevation offsets (abstract). Lunar Planet. Sci. XXXI, abstract#1879.

Wilkins, S.J., and Schultz, R.A. (2003). Cross faults extensional settings: Stress triggering, displacement location, and implications for the origin of blunt troughs at Valles Marineris, Mars. JGR, 108(E6), doi:10.1029/2002JE001968.

Williams, J. P., and Nimmo, F. (2004). Thermal evolution of the Martian core: Implications for an early dynamo. Geology, 32(2), 97-100.

Williams, J.P., Paige, D.A., and Manning, C.E. (2003). Layering in the wall rock of Valles Marineris: Intrusive and extrusive magmatism. Geo. Res. Lett., 30(12), 1623, doi:10.1029/2003GL017662.

Witbeck, N.E., Tanaka, K.L., and Scott, D.H. (1991). Geologic map of the Valles Marineris Region, Mars (East half and West half): U.S. Geological Survey Scientific Investigations Map I-2010, scale 1:20,000,000.

Zuber, M. T., and Aist, L.L. (1990). The shallow structure of the Martian lithosphere in the vicinity of the ridged plains. JGR, 95(B9), 14215-14230.

Zuber, M.T. (1995). Wrinkle Ridges, Reverse Faulting, and the Depth Penetration of Lithospheric Strain in Lunae, Mars. Icarus, 114, 80-92.

Appendices

A. List of DEMs

- **MOLA**

MOLA global DEM from interpolation of the MOLA tracks.
Resolution ~450 m/px.

MOLA-HRSC blended DEM.
Resolution ~200 m/px.

- **HRSC**

#	Orbit	Resolution [m/px]
1	H0334_0001	100
2	H0360_0000	100
3	H0438_0000	100
4	H0449_0009	200
5	H0471_0001	150
6	H0515_0000	175
7	H0982_0000	50
8	H1004_0001	75
9	H1995_0000	50
10	H2028_0000	50
11	H2039_0000	50
12	H3195_0000	75
13	H4160_0000	75
14	H4171_0000	75
15	H2138_0000	50
16	H5178_0000	75
17	H1885_0000	100

- **CTX**

*All files have a resolution of ~18 m/px.

Coprates Chasma

1	Coprates	CTX	1	B19	17200	1667	XN	13S063W-B21	17912	1681	XN	11S063W
2	Coprates	CTX	2	B17	16303	1649	XN	15S053W-P16	7218	1649	XN	15S053W
3	Coprates	CTX	3	P08	4159	1652	XI	14S056W-P15	6783	1654	XN	14S056W
4	Coprates	CTX	4	G16	24584	1662	XN	13S057W-P12	5570	1650	XN	15S057W
5	Coprates	CTX	5	B06	11912	1653	XI	14S055W-P21	9222	1660	XI	14S055W
6	Coprates	CTX	6	B16	16026	1643	XN	15S054W-P15	6717	1643	XI	15S054W
7	Coprates	CTX	7	G03	19270	1658	XN	14S059W-G04	19903	1658	XN	14S059W
8	Coprates	CTX	8	P04	2722	1673	XI	12S064W-P06	3355	1673	XI	12S064W
9	Coprates	CTX	9	B21	17688	1685	XN	11S067W-B22	18321	1685	XN	11S068W
10	Coprates	CTX	10	G07	20879	1669	XN	13S066W-G09	21657	1665	XN	13S066W
11	Coprates	CTX	11	D04	28751	1641	XN	15S054W-P13	6216	1663	XN	13S055W
12	Coprates	CTX	12	D02	27973	1655	XN	14S055W-G18	25441	1656	XN	14S055W
13	Coprates	CTX	13	B10	13547	1653	XN	14S054W-B10	13613	1652	XN	14S054W
14	Coprates	CTX	14	D01	27630	1651	XN	14S053W-P15	7073	1650	XI	15S053W
15	Coprates	CTX	15	G20	25929	1675	XN	12S056W-P16	7139	1653	XN	14S056W
16	Coprates	CTX	16	B06	11912	1653	XI	14S055W-G18	25085	1652	XN	14S055W
17	Coprates	CTX	17	P04	2735	1667	XI	13S059W-P06	3513	1656	XI	14S059W
18	Coprates	CTX	18	D01	27538	1674	XN	12S062W-P08	4212	1666	XI	13S062W
19	Coprates	CTX	19	G23	27393	1677	XN	12S064W-P08	4067	1681	XN	11S064W
20	Coprates	CTX	20	P06	3210	1679	XN	12S067W-P07	3922	1678	XI	12S067W
21	Coprates	CTX	21	B05	11543	1670	XN	13S062W-G21	26483	1670	XN	13S062W
22	Coprates	CTX	22	B02	10475	1667	XI	13S063W-G21	26615	1677	XN	12S064W
23	Coprates	CTX	23	B20	17332	1682	XN	11S068W-D04	28791	1681	XN	11S068W
24	Coprates	CTX	24	G18	25230	1651	XN	14S054W-G20	26008	1651	XN	14S054W
25	Coprates	CTX	25	B17	16303	1649	XN	15S053W-P16	7218	1649	XN	15S053W
26	Coprates	CTX	26	P06	3513	1656	XI	14S059W-P10	5069	1673	XI	12S060W
27	Coprates	CTX	27	P02	1812	1667	XN	13S060W-P07	3658	1658	XI	14S060W
28	Coprates	CTX	28	D14	32549	1677	XN	12S066W-D14	32694	1677	XN	12S066W
29	Coprates	CTX	29	D17	33762	1675	XN	12S065W-P16	7258	1686	XN	11S066W
30	Coprates	CTX	30	D12	31784	1669	XN	13S065W-P14	6546	1670	XN	13S065W
31	Coprates	CTX	31	B12	14167	1660	XN	14S061W-D13	32140	1668	XN	13S061W
32	Coprates	CTX	32	D20	34988	1669	XN	13S060W-D21	35410	1669	XN	13S060W

33	Coprates	CTX	33	D07	29806	1662	XN	13S058W-D13	32364	1663	XN	13S058W
34	Coprates	CTX	35	D16	33432	1654	XN	14S057W-D19	34566	1653	XN	14S057W
35	Coprates	CTX	36	F01	36267	1651	XN	14S055W-F02	36623	1651	XN	14S055W
36	Coprates	CTX	37	D22	35779	1651	XN	14S052W-D22	35924	1651	XN	14S052W
37	Coprates	CTX	38	D22	35911	1651	XN	14S057W-F02	36689	1660	XN	14S057W
38	Coprates	CTX	39	D22	35621	1659	XN	14S060W-D22	35977	1659	XN	14S060W
39	Coprates	CTX	40	D22	35898	1670	XN	13S063W-F01	36320	1669	XN	13S063W
40	Coprates	CTX	41	D14	32694	1677	XN	12S066W-F01	36241	1677	XN	12S066W
41	Coprates	CTX	42	D22	35621	1659	XN	14S060W-D22	35977	1659	XN	14S060W
42	Coprates	CTX	43	D22	35779	1651	XN	14S052W-P07	3671	1642	XI	15S052W
43	Coprates	CTX	44	P16	7218	1649	XN	15S053W-P22	9789	1656	XN	14S053W
44	Coprates	CTX	47	P17	7574	1647	XN	15S054W-P17	7719	1652	XN	14S054W
45	Coprates	CTX	48	D08	30386	1651	XN	14S054W-P16	7429	1671	XN	12S054W
46	Coprates	CTX	49	D10	31019	1652	XN	14S055W-D16	33366	1651	XN	14S055W
47	Coprates	CTX	50	B07	12268	1652	XI	14S055W-P05	3104	1654	XI	14S055W
48	Coprates	CTX	51	D20	34856	1652	XN	14S056W-D21	35278	1652	XN	14S056W
49	Coprates	CTX	52	D18	34289	1649	XN	15S053W-P15	7073	1650	XI	15S053W
50	Coprates	CTX	53	P17	7508	1648	XN	15S052W-P20	8945	1647	XN	15S052W
51	Coprates	CTX	54	D12	31942	1655	XN	14S056W-D14	32575	1654	XN	14S056W
52	Coprates	CTX	55	F03	36808	1670	XN	13S065W-F03	36953	1675	XN	12S065W
53	Coprates	CTX	56	F04	37256	1653	XN	14S057W-G22	26918	1673	XN	12S057W
54	Coprates	CTX	57	G16	24650	1656	XN	14S058W-P07	3869	1655	XN	14S058W
55	Coprates	CTX	58	D21	35331	1668	XN	13S064W-D21	35542	1668	XN	13S063W
56	Coprates	CTX	59	G04	19824	1673	XN	12S065W-P07	3711	1680	XN	12S065W
57	Coprates	CTX	60	D22	35779	1651	XN	14S052W-D22	35924	1651	XN	14S052W
58	Coprates	CTX	61	F03	36874	1688	XN	11S068W-P07	3632	1681	XI	11S068W
59	Coprates	CTX	62	D21	35476	1672	XN	12S064W-G18	25349	1661	XN	13S064W
60	Coprates	CTX	63	D08	30439	1666	XN	13S062W-F01	36109	1669	XI	13S062W
61	Coprates	CTX	64	G18	25362	1661	XN	13S058W-P13	6137	1655	XN	14S058W
62	Coprates	CTX	65	D22	35964	1670	XN	13S065W-P14	6546	1670	XN	13S065W
63	Coprates	CTX	66	D12	31784	1669	XN	13S065W-F02	36597	1674	XN	12S065W
64	Coprates	CTX	67	F06	38179	1651	XN	14S052W-P17	7508	1648	XN	15S052W
65	Coprates	CTX	68	D14	32549	1677	XN	12S066W-F01	36241	1677	XN	12S066W
66	Coprates	CTX	69	P07	3566	1711	XN	08S066W-P12	5623	1714	XI	08S066W
67	Coprates	CTX	70	G11	22369	1687	XN	11S066W-G12	23002	1686	XN	11S066W
68	Coprates	CTX	71	F03	36953	1675	XN	12S065W-F17	42584	1671	XN	12S065W
69	Coprates	CTX	72	D22	35964	1670	XN	13S065W-F03	36808	1670	XN	13S065W
70	Coprates	CTX	73	F02	36597	1674	XN	12S065W-P14	6546	1670	XN	13S065W
71	Coprates	CTX	74	P07	3711	1680	XN	12S065W-P11	5267	1699	XI	10S065W
72	Coprates	CTX	75	D21	35252	1672	XN	12S064W-P02	1733	1673	XN	12S064W
73	Coprates	CTX	76	D21	35476	1672	XN	12S064W-G18	25349	1661	XN	13S064W

74	Coprates	CTX	77	D21	35265	1668	XN	13S063W-F05	37665	1671	XN	12S064W
75	Coprates	CTX	78	G23	27393	1677	XN	12S064W-P08	4067	1681	XN	11S064W
76	Coprates	CTX	79	B02	10475	1667	XI	13S063W-G07	20958	1680	XN	12S063W
77	Coprates	CTX	80	B02	10475	1667	XI	13S063W-D21	35265	1668	XN	13S063W
78	Coprates	CTX	81	G23	27182	1669	XN	13S063W-G23	27327	1669	XN	13S063W
79	Coprates	CTX	82	D20	35120	1669	XN	13S063W-F05	37876	1666	XN	13S063W
80	Coprates	CTX	83	D17	33986	1668	XI	13S062W-D18	34131	1669	XI	13S062W
81	Coprates	CTX	84	D08	30439	1666	XN	13S062W-P08	4212	1666	XI	13S062W
82	Coprates	CTX	85	F09	39142	1651	XN	14S053W-F19	43111	1644	XI	15S053W
83	Coprates	CTX	86	G20	26008	1651	XN	14S054W-P17	7574	1647	XN	15S054W
84	Coprates	CTX	87	B10	13613	1652	XN	14S054W-B11	14048	1653	XN	14S054W
85	Coprates	CTX	88	G19	25850	1688	XN	11S060W-P02	1812	1667	XN	13S060W
86	Coprates	CTX	89	B05	11675	1673	XN	12S066W-F16	41872	1672	XN	12S066W
87	Coprates	CTX	90	B20	17332	1682	XN	11S068W-P07	3632	1681	XI	11S068W
88	Coprates	CTX	91	D01	27525	1688	XN	11S068W-F01	36096	1682	XN	11S068W
89	Coprates	CTX	92	B22	18321	1685	XN	11S068W-P04	2643	1688	XN	11S068W
90	Coprates	CTX	93	B21	17688	1685	XN	11S067W-F02	36663	1680	XN	12S067W
91	Coprates	CTX	94	F02	36663	1680	XN	12S067W-P04	2643	1688	XN	11S068W
92	Coprates	CTX	95	P06	3210	1679	XN	12S067W-P20	8906	1685	XN	11S067W
93	Coprates	CTX	96	P20	8906	1685	XN	11S067W-P22	9763	1690	XN	11S067W
94	Coprates	CTX	97	B12	14365	1692	XI	10S067W-B19	17121	1691	XI	10S067W
95	Coprates	CTX	98	F20	43784	1677	XI	12S067W-P16	7113	1678	XN	12S067W
96	Coprates	CTX	99	B11	13732	1690	XN	11S067W-F20	43784	1677	XI	12S067W
97	Coprates	CTX	100	B05	11543	1670	XN	13S062W-P13	6269	1670	XN	13S062W
98	Coprates	CTX	101	F19	43164	1663	XI	13S061W-P21	9420	1661	XN	13S061W
99	Coprates	CTX	102	F19	43375	1662	XI	13S061W-P21	9420	1661	XN	13S061W
100	Coprates	CTX	103	G19	25560	1677	XN	12S062W-G19	25705	1677	XN	12S062W
101	Coprates	CTX	104	B01	9987	1661	XN	13S061W-F12	40461	1673	XN	12S061W
102	Coprates	CTX	105	F16	42030	1661	XI	13S060W-F17	42531	1661	XN	13S060W
103	Coprates	CTX	106	F02	36465	1660	XI	14S060W-P08	4080	1651	XI	14S060W
104	Coprates	CTX	107	D21	35344	1659	XN	14S060W-D22	35977	1659	XN	14S060W
105	Coprates	CTX	108	F18	42742	1671	XN	12S059W-P04	2735	1667	XI	13S059W
106	Coprates	CTX	109	D20	35199	1664	XN	13S059W-D21	35555	1664	XN	13S059W
107	Coprates	CTX	110	B19	16976	1685	XN	11S069W-B19	17187	1685	XN	11S069W
108	Coprates	CTX	111	D01	27591	1677	XI	12S069W-G23	27314	1678	XI	12S069W

West Candor Chasma

1	West Candor	CTX	1	G10	22132	1742	XI	05S075W-G10	22211	1752	XI	04S075W
2	West Candor	CTX	2	G11	22567	1736	XI	06S074W-G12	22989	1736	XI	06S074W
3	West Candor	CTX	3	B09	13007	1726	XI	07S072W-G10	21934	1733	XI	06S072W
4	West Candor	CTX	4	P02	1707	1744	XN	05S076W-P05	2841	1744	XI	05S076W
5	West Candor	CTX	5	P08	4186	1745	XI	05S074W-P12	5597	1745	XI	05S074W
6	West Candor	CTX	7	G11	22343	1743	XN	05S076W-G11	22699	1742	XN	05S076W
7	West Candor	CTX	9	P03	2195	1743	XI	05S077W-P03	2340	1738	XI	06S077W
8	West Candor	CTX	10	G15	23978	1736	XI	06S074W-G16	24334	1736	XI	06S074W
9	West Candor	CTX	12	G03	19587	1746	XI	05S074W-P01	1443	1740	XN	06S074W
10	West Candor	CTX	13	D12	31758	1730	XN	07S076W-D12	31824	1730	XN	07S076W
11	West Candor	CTX	14	B02	10515	1742	XN	05S075W-P06	3197	1736	XI	06S075W
12	West Candor	CTX	16	B01	10027	1735	XN	06S073W-P20	9038	1736	XN	06S073W
13	West Candor	CTX	18	B18	16686	1738	XI	06S072W-B19	17108	1737	XI	06S072W
14	West Candor	CTX	19	G02	19020	1743	XI	05S073W-G03	19376	1739	XI	06S073W
15	West Candor	CTX	20	G11	22567	1736	XI	06S074W-P18	7957	1744	XI	05S074W
16	West Candor	CTX	21	F20	43705	1722	XI	07S072W-P06	3553	1745	XI	05S072W
17	West Candor	CTX	23	G04	19653	1742	XI	05S075W-P07	3830	1731	XI	06S075W
18	West Candor	CTX	24	B19	17174	1746	XI	05S075W-G10	22211	1752	XI	04S075W
19	West Candor	CTX	25	D22	35793	1751	XN	04S076W-P10	5096	1738	XI	06S076W
20	West Candor	CTX	26	D01	27644	1744	XN	05S077W-G23	27288	1744	XN	05S077W
21	West Candor	CTX	27	D21	35582	1745	XN	05S076W-F01	36070	1745	XN	05S076W

East Candor Chasma

1	East Candor	CTX	1	G04	19666	1745	XN	05S071W-P02	1997	1744	XN	05S072W
2	East Candor	CTX	2	D06	29714	1747	XI	05S070W-P03	2142	1748	XI	05S071W
3	East Candor	CTX	3	D09	30650	1715	XI	08S064W-P05	3078	1734	XI	06S065W
4	East Candor	CTX	4	B20	17411	1722	XN	07S065W-P21	9341	1722	XN	07S065W
5	East Candor	CTX	5	D04	28725	1730	XI	07S066W-D07	30004	1729	XI	07S066W
6	East Candor	CTX	6	G06	20668	1727	XN	07S066W-G07	20813	1728	XN	07S066W
7	East Candor	CTX	7	D02	27947	1732	XN	06S068W-D02	28013	1732	XN	06S068W
8	East Candor	CTX	8	P01	1390	1734	XI	06S069W-P04	2498	1734	XI	06S069W
9	East Candor	CTX	9	D06	29648	1723	XI	07S067W-D07	29925	1722	XI	07S067W
10	East Candor	CTX	10	G11	22646	1736	XN	06S068W-P13	6256	1720	XN	08S068W
11	East Candor	CTX	11	P13	5979	1721	XI	07S065W-P15	6757	1724	XI	07S065W
12	East Candor	CTX	12	P10	5122	1724	XI	07S067W-P12	5900	1738	XI	06S068W
13	East Candor	CTX	13	P01	1522	1734	XN	06S069W-P02	1931	1721	XN	07S069W
14	East Candor	CTX	14	D01	27736	1727	XN	07S066W-G23	27248	1726	XN	07S066W
15	East Candor	CTX	15	B12	14154	1727	XN	07S067W-P19	8260	1726	XN	07S067W
16	East Candor	CTX	16	D14	32773	1721	XN	07S065W-D15	33195	1721	XN	07S065W
17	East Candor	CTX	17	D15	32918	1720	XN	08S064W-D15	32984	1720	XN	08S064W
18	East Candor	CTX	18	G10	22290	1736	XI	06S070W-P04	2709	1744	XN	05S070W
19	East Candor	CTX	19	P05	3131	1747	XI	05S071W-P11	5254	1746	XI	05S071W
20	East Candor	CTX	20	G04	19666	1745	XN	05S071W-P02	1997	1744	XN	05S072W
21	East Candor	CTX	21	G05	20299	1735	XN	06S071W-P03	2353	1734	XN	06S071W
22	East Candor	CTX	22	D16	33274	1720	XN	08S064W-D16	33419	1720	XN	08S064W
23	East Candor	CTX	23	B12	14154	1727	XN	07S067W-D12	31982	1731	XN	06S067W
24	East Candor	CTX	24	G20	25903	1730	XN	07S068W-P11	5333	1734	XI	06S068W
25	East Candor	CTX	25	P01	1522	1734	XN	06S069W-P12	5755	1739	XN	06S069W
26	East Candor	CTX	26	G10	22290	1736	XI	06S070W-P02	1931	1721	XN	07S069W
27	East Candor	CTX	27	G18	25191	1739	XN	06S070W-P04	2709	1744	XN	05S070W
28	East Candor	CTX	28	G04	19666	1745	XN	05S071W-P18	7891	1742	XN	05S071W
29	East Candor	CTX	29	B02	10330	1717	XI	08S066W-D04	28725	1730	XI	07S066W
30	East Candor	CTX	30	D20	34896	1724	XI	07S067W-P19	8260	1726	XN	07S067W
31	East Candor	CTX	31	D15	32971	1734	XN	06S069W-P12	5755	1739	XN	06S069W
32	East Candor	CTX	32	F06	38140	1742	XI	05S069W-P12	5755	1739	XN	06S069W
33	East Candor	CTX	33	F05	37586	1723	XN	07S066W-F05	37731	1723	XN	07S066W
34	East Candor	CTX	34	B07	12532	1707	XN	09S063W-P07	3856	1737	XN	06S064W
35	East Candor	CTX	35	G20	25903	1730	XN	07S068W-P11	5333	1734	XI	06S068W
36	East Candor	CTX	36	B09	12954	1725	XN	07S066W-B09	13310	1725	XN	07S066W
37	East Candor	CTX	37	B06	11965	1725	XN	07S066W-B07	12242	1724	XN	07S066W
38	East Candor	CTX	38	F01	36373	1735	XN	06S069W-F02	36518	1734	XN	06S069W

39	East Candor	CTX	39	D15	32971	1734	XN	06S069W-F01	36373	1735	XN	06S069W
40	East Candor	CTX	40	G10	22290	1736	XI	06S070W-P11	5188	1743	XI	05S070W
41	East Candor	CTX	41	F06	38140	1742	XI	05S069W-F10	39736	1740	XI	06S069W
42	East Candor	CTX	42	B09	13086	1749	XI	05S069W-D02	28013	1732	XN	06S068W
43	East Candor	CTX	43	D19	34685	1727	XN	07S067W-D19	34751	1727	XN	07S067W
44	East Candor	CTX	45	P07	3566	1711	XN	08S066W-P12	5623	1714	XI	08S066W
45	East Candor	CTX	46	P03	2366	1723	XN	07S066W-P18	7904	1722	XN	07S065W
46	East Candor	CTX	47	B05	11609	1719	XN	08S065W-B08	12664	1720	XN	08S065W
47	East Candor	CTX	48	D17	33907	1719	XN	08S064W-D18	34263	1719	XN	08S064W
48	East Candor	CTX	49	D20	35041	1720	XN	08S064W-G02	19046	1720	XI	08S064W
49	East Candor	CTX	50	J04	46329	1740	XN	06S064W-J04	46474	1740	XN	06S064W

Ius Chasma

1	Ius	CTX	2	P18	8010	1720	XN	08S080W-P22	9658	1719	XN	08S080W
2	Ius	CTX	3	P04	2551	1712	XI	08S076W-P05	2828	1711	XI	08S076W
3	Ius	CTX	4	D02	27855	1710	XN	09S077W-G20	25956	1712	XN	08S077W
4	Ius	CTX	5	B17	16383	1713	XN	08S077W-B18	16528	1713	XN	08S077W
5	Ius	CTX	6	G20	26022	1715	XN	08S077W-G20	26088	1715	XN	08S077W
6	Ius	CTX	7	B08	12849	1716	XN	08S078W-P06	3184	1704	XN	09S078W
7	Ius	CTX	8	B09	13060	1715	XI	08S078W-D02	28132	1724	XN	07S078W
8	Ius	CTX	9	P01	1364	1714	XI	08S079W-P18	8155	1728	XI	07S079W
9	Ius	CTX	10	G02	18928	1717	XN	08S082W-P21	9368	1718	XN	08S082W
10	Ius	CTX	11	B20	17293	1724	XN	07S083W-P15	6784	1719	XN	08S083W
11	Ius	CTX	12	G19	25653	1723	XN	07S084W-P05	2815	1720	XN	08S084W
12	Ius	CTX	13	P07	3606	1727	XN	07S079W-P17	7799	1716	XI	08S079W
13	Ius	CTX	14	G14	23675	1722	XN	07S081W-P03	2327	1721	XI	07S081W
14	Ius	CTX	15	B01	10146	1738	XI	06S082W-B02	10568	1726	XN	07S082W
15	Ius	CTX	16	G05	20115	1731	XI	06S087W-P02	1958	1731	XN	06S087W
16	Ius	CTX	17	D01	27618	1731	XN	06S086W-P07	3870	1735	XN	06S086W
17	Ius	CTX	18	B22	18348	1730	XN	07S086W-D07	29807	1730	XN	07S086W
18	Ius	CTX	19	D01	27552	1715	XN	08S085W-P04	2670	1732	XN	06S085W
19	Ius	CTX	21	D22	35635	1724	XN	07S083W-G23	27341	1725	XN	07S083W
20	Ius	CTX	22	F01	36268	1737	XN	06S084W-P08	4160	1736	XN	06S084W
21	Ius	CTX	23	G19	25653	1723	XN	07S084W-P16	7140	1742	XN	05S084W
22	Ius	CTX	24	D21	35279	1724	XN	07S084W-P09	4582	1735	XN	06S084W
23	Ius	CTX	25	P06	3237	1734	XI	06S085W-P11	5215	1722	XI	07S085W
24	Ius	CTX	26	D16	33433	1730	XN	07S085W-D20	35134	1730	XN	07S085W
25	Ius	CTX	27	B06	11979	1731	XI	06S086W-P06	3303	1743	XN	05S087W
26	Ius	CTX	28	P06	3514	1742	XI	05S088W-P12	5848	1741	XI	05S088W
27	Ius	CTX	29	P08	4292	1744	XN	05S087W-P12	5782	1742	XI	05S087W
28	Ius	CTX	30	P07	3817	1729	XN	07S079W-P15	6797	1725	XN	07S079W
29	Ius	CTX	31	G13	23398	1723	XN	07S080W-P11	5373	1730	XI	07S080W
30	Ius	CTX	32	D19	34580	1720	XN	08S079W-P17	7654	1730	XN	07S080W
31	Ius	CTX	33	P12	5795	1730	XI	07S082W-P15	6863	1732	XN	06S081W
32	Ius	CTX	34	F13	40765	1723	XN	07S083W-P12	5650	1733	XI	06S083W
33	Ius	CTX	35	F16	42044	1734	XI	06S082W-F16	42189	1734	XI	06S082W
34	Ius	CTX	36	P16	7364	1733	XN	06S081W-P22	9513	1733	XN	06S081W
35	Ius	CTX	37	D18	34092	1713	XN	08S076W-D19	34514	1712	XN	08S076W
36	Ius	CTX	38	F14	41187	1729	XN	07S084W-G02	18849	1728	XN	07S084W
37	Ius	CTX	39	F02	36479	1733	XN	06S083W-F13	40765	1723	XN	07S083W
38	Ius	CTX	40	F11	40132	1725	XI	07S082W-P12	5650	1733	XI	06S083W

39	Ius	CTX	41	G02	18928	1717	XN	08S082W-G03	19350	1717	XN	08S082W
40	Ius	CTX	42	F19	43112	1732	XI	06S081W-P15	6863	1732	XN	06S081W
41	Ius	CTX	43	P04	2683	1728	XN	07S080W-P22	9658	1719	XN	08S080W
42	Ius	CTX	44	F17	42268	1731	XI	06S079W-P18	8155	1728	XI	07S079W
43	Ius	CTX	45	F16	41978	1719	XI	08S079W-P15	6797	1725	XN	07S079W
44	Ius	CTX	46	D01	27710	1716	XN	08S078W-F20	43547	1729	XI	07S079W

Melas Chasma

1	Melas	CTX	1	B19	16976	1685	XN	11S069W-B19	17187	1685	XN	11S069W
2	Melas	CTX	2	B02	10396	1699	XN	10S069W-B05	11451	1698	XN	10S069W
3	Melas	CTX	3	B12	14128	1726	XN	07S075W-P05	2907	1706	XN	09S075W
4	Melas	CTX	4	B03	10673	1664	XI	13S071W-P21	9394	1665	XN	13S071W
5	Melas	CTX	5	D04	28778	1692	XN	10S073W-D06	29635	1693	XI	10S073W
6	Melas	CTX	6	D01	27657	1685	XI	11S072W-D02	27934	1685	XI	11S072W
7	Melas	CTX	7	D02	28000	1694	XI	10S074W-D02	28066	1694	XI	10S074W
8	Melas	CTX	8	D08	30545	1699	XI	10S075W-P01	1575	1702	XN	09S075W
9	Melas	CTX	9	D01	27446	1678	XI	12S071W-D01	27723	1677	XI	12S071W
10	Melas	CTX	10	D04	28712	1663	XI	13S070W-G23	27380	1674	XI	12S070W
11	Melas	CTX	11	D05	29345	1681	XI	11S072W-D09	30558	1681	XI	11S072W
12	Melas	CTX	12	D08	30492	1674	XI	12S071W-P06	3342	1686	XN	11S071W
13	Melas	CTX	13	D01	27512	1694	XI	10S073W-G23	27367	1694	XI	10S073W
14	Melas	CTX	14	D17	33815	1692	XI	10S074W-D17	33960	1692	XI	10S074W
15	Melas	CTX	15	D13	32180	1693	XI	10S073W-D13	32470	1693	XI	10S073W
16	Melas	CTX	16	D08	30413	1684	XI	11S071W-D14	32760	1683	XI	11S071W
17	Melas	CTX	17	D18	34250	1676	XI	12S070W-D21	35450	1674	XI	12S070W
18	Melas	CTX	19	D01	27591	1677	XI	12S069W-G23	27314	1678	XI	12S069W
19	Melas	CTX	20	D09	30756	1697	XN	10S075W-D10	31191	1697	XN	10S075W
20	Melas	CTX	21	F16	41991	1714	XI	08S075W-F16	42136	1714	XI	08S075W

Ophir Chasma

1	Ophir	CTX	1	G10	22145	1760	XI	04S073W-G10	22277	1760	XI	04S073W
2	Ophir	CTX	2	B20	17609	1757	XN	04S072W-B22	18031	1757	XN	04S072W
3	Ophir	CTX	3	G08	21499	1761	XN	03S072W-P03	2208	1748	XN	05S072W
4	Ophir	CTX	4	B01	10172	1756	XN	04S071W-P20	8972	1756	XN	04S071W
5	Ophir	CTX	5	P04	2709	1744	XN	05S070W-P11	5188	1743	XI	05S070W
6	Ophir	CTX	7	B21	17886	1763	XN	03S074W-G22	26879	1764	XN	03S074W
7	Ophir	CTX	8	B01	9895	1764	XN	03S071W-P22	9750	1765	XN	03S071W
8	Ophir	CTX	9	D14	32826	1763	XN	03S073W-P03	2208	1748	XN	05S072W
9	Ophir	CTX	11	G04	19943	1757	XI	04S072W-G09	21855	1758	XI	04S072W
10	Ophir	CTX	12	D16	33393	1754	XN	04S073W-D17	33749	1754	XN	04S073W
11	Ophir	CTX	14	D14	32826	1763	XN	03S073W-F05	37573	1764	XI	03S073W
12	Ophir	CTX	15	D22	35661	1746	XI	05S071W-F04	37428	1779	XN	02S072W
13	Ophir	CTX	17	D06	29714	1747	XI	05S070W-P03	2142	1748	XI	05S071W
14	Ophir	CTX	18	J02	45459	1770	XN	03S071W-J02	45525	1770	XN	03S071W
15	Ophir	CTX	19	F03	36795	1748	XN	05S073W-F04	37217	1758	XN	04S073W
16	Ophir	CTX	20	F01	36083	1775	XN	02S074W-F02	36505	1762	XN	03S074W
17	Ophir	CTX	21	D21	35516	1763	XN	03S074W-F03	36861	1762	XN	03S074W
18	Ophir	CTX	22	D20	34949	1763	XN	03S074W-F03	36861	1762	XN	03S074W
19	Ophir	CTX	23	F06	38140	1742	XI	05S069W-F10	39736	1740	XI	06S069W
20	Ophir	CTX	24	G05	20220	1762	XN	03S074W-P20	8893	1762	XN	03S074W
21	Ophir	CTX	25	B07	12374	1758	XN	04S070W-P11	5188	1743	XI	05S070W
22	Ophir	CTX	26	G10	22290	1736	XI	06S070W-P11	5188	1743	XI	05S070W

B. Rake methodology: Step by step on ArcGIS

The rake is the inner angle between the spur crest on the attitude of its respective section of the wall projected horizontal plane. The projection on a horizontal plane does not affect the measurement of the angle since the geometrical properties remain the same as it is similar to a horizontal rotation of the plane. Therefore, the use of 2D measurements to obtain this 3D angle is appropriate.

The measurements are made on ArcGIS using available tools such as *Add Geometry Attributes, Near, Join Field, Calculate Field, and Delete Field*. These tools were used in a respective order to provide the geometric attributes to the linear features that represent the spur and the attitude of the walls (Figure 3-18A). The steps to calculate the rake are the following:

1. First, two polyline shapefiles are made to start the measurements. One for the spurs and one for the attitude of the walls, both are defined within the *Equirectangular* spatial reference projection. These shapefiles are used to measure the attitudes of the features following the right hand rule along the walls of the chasma that were selected to be measured.
2. Once the features are drawn, proceed to add geometry attributes like the length of the linear feature and the coordinates if the ends of each line and the center of it. This is done for both the spurs and the attitude of the walls.
3. The next step is determining the closest section of wall for each spur. This is done using the *Near* tool where the input is the spurs shapefile and the near requirement is the walls shapefile. With this connection, it is possible to join the geometry attributes from the walls shapefile to the spurs shapefile.

4. A new field is added to the spurs shapefile, this new field is the *rake*. The field is added to make the variable available to proceed to the calculation of it.
5. The rake value is calculated using the *Calculate Field* tool using the following configuration:

   Input Table:

   [Spurs shapefile]

   Field Name:

   [Rake]

   Expression:

   Line [1]: CodeCalc(!END_X! - !START_X! , !END_Y! - !START_Y! , !END_X_1! - !START_X_1! , !END_Y_1! - !START_Y_1!)

   Expression Type:

   PYTHON

   Code Block:

   Line [1]: def CodeCalc(SX,SY,WX,WY):

   Line [2]: return

   Line [3]: 57.29578*math.acos((SX*WX+SY*WY)/(math.sqrt(SX*SX+SY*SY)* math.sqrt(WX*WX+WY*WY)))

After step 5 the values will be available to be used. The symbology of the features was changed in order to have better visualization of the results. The used symbology uses *Quantities* taking the rake values un-normalized representing them in 5 ranges; 0-60° (red), 60-80° (pink), 80-100°(white), 100-120° (cyan), and 120-180° (blue). This is the representation observed on Figure 3-18B, the mentioned colors fill the circle on each spur.

A better interpretation of the results uses a line density distribution to show the most significant rake values of the spurs within each selected section of the wall (Figure 3-18B). This raster projected over the walls helps the visualization, and interpretation of the results and it is calculated using the *Line Statistics* tool. The tool requires the following information:

Input polyline features:

[Spurs shapefile]

Field:

[Rake]

Outer Raster:

[New raster with the results]

Output cell size:

500 ← This value was selected to help the visualization of the results and it is in meters

Search radius:

3000 ← This value was selected based on the distance between the spurs after trials.

Statistics type:

MAXIMUM

The resulting raster is modified to have the same color-scheme used for the linear features using the same ranges. The whole routine was summarized into just one model built to reduce the time of calculation and user interaction.

C. Azimuth of the crest of the walls

The rake analysis relies on the proper description of the sections of the walls. The sections of the walls used for the rake analysis are areas with widths of up to 40 km along the strike of the wall and lengths of up to 30 km downslope along the wall. These sections were defined using the straight crest of the wall. The presence of headwalls was discarded due its secondary erosional formation.

The strike of the crest of the walls will be referred as the azimuth. This value can provide information relative to the shape of the chasma and possible later changes. The azimuth of the crest of the walls was quantified and compared using a rose diagram that shows the dominant orientations of the walls (Figure C - 1). The measurements were made using the right hand rule therefore the diagrams show the actual orientation of the chasmata. The number of spikes in the diagrams describes the shape of the chasma: rectangular chasm with little alterations have two larger spikes opposite to each other (Figure C - 1 A-C), while chasma with irregular or rounded shape have several spikes with various attitudes distributed along the 360° scale (Figure C - 1 D&E).

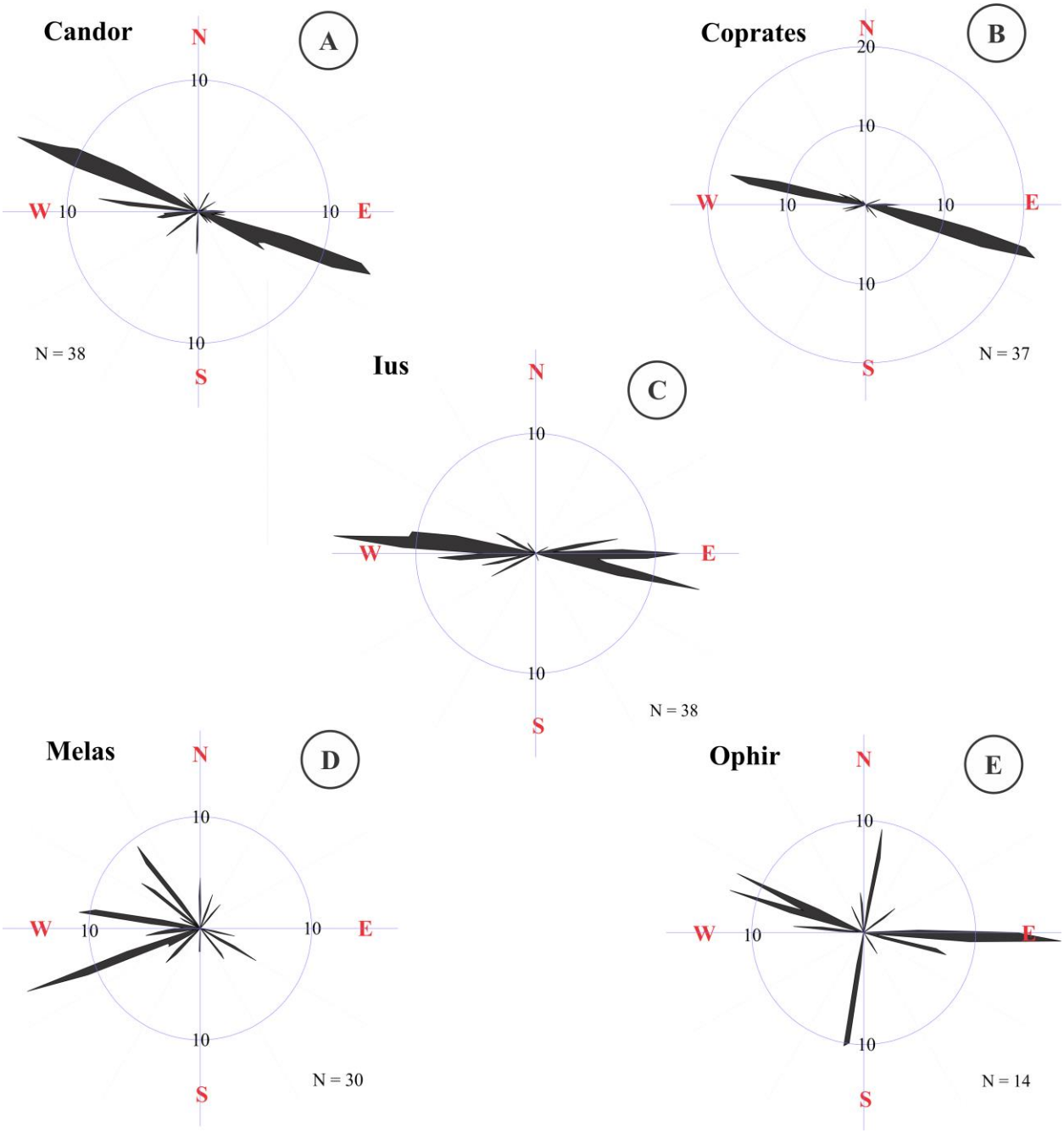

Figure C - 1: Rose diagrams of the azimuth of the crest of the walls of (A) Candor Chasma (B) Coprates Chasma (C) Ius Chasma (D) Melas Chasma and (E) Ophir Chasma. The diagrams show the dominance in wall orientation based on the shape of the chasma.